Controlling Field-Directed Assembly of Nanowires: Towards Nanomanufacturing for Biosensors and Transparent Electrodes

by

Mahshid Sam
B.Sc., University of Shiraz, 2005
M.Sc., University of Shiraz, 2008

A Dissertation Submitted in Partial Fulfillment of the
Requirements for the Degree of

DOCTOR OF PHILOSOPHY

in the Department of Mechanical Engineering

Controlling Field-Directed Assembly of Nanowires: Towards Nanomanufacturing for Biosensors and Transparent Electrodes

by

Mahshid Sam
B.Sc., University of Shiraz, 2005
M.Sc., University of Shiraz, 2008

Supervisory Committee

Dr. R.B. Bhiladvala, Supervisor
(Department of Mechanical Engineering)

Dr. M.B.G. Jun, Departmental Member
(Department of Mechanical Engineering)

Dr. B. Buckham, Departmental Member
(Department of Mechanical Engineering)

Dr. T. Lu, Outside Member
(Department of Electrical and Computer Engineering)

Supervisory Committee

Dr. R.B. Bhiladvala, Supervisor
(Department of Mechanical Engineering)

Dr. M.B.G. Jun, Departmental Member
(Department of Mechanical Engineering)

Dr. B. Buckham, Departmental Member
(Department of Mechanical Engineering)

Dr. T. Lu, Outside Member
(Department of Electrical and Computer Engineering)

ABSTRACT

The remarkable mechanical, optical, thermal and electronic properties of one-dimensional structures such as nanotubes or nanowires (NWs) have enabled the construction of devices of extraordinary capabilities. Nanotube resonators, for example, were recently used to demonstrate response to single-proton mass. However, such landmark demonstrations are limited to a small number of devices in research laboratories, since the cost of making them by traditional top-down methods is prohibitive, being proportional to the number of devices. This thesis makes contributions towards a new family of methods, field-directed assembly, to enable reliable and cost-effective fabrication of large numbers of nanodevices. This provides a path towards nanomanufacturing, to help bring the extraordinary capabilities of nanodevices into widespread commercial and scientific use.

Field-directed assembly is a cost-effective technique in which NWs are first synthesized, suspended in a fluid medium and then directed by fields, to predetermined positions between electrodes patterned on a substrate. When the gap size between electrode pairs is comparable to the length of NWs, a single NW can be positioned between each pair of electrodes. This technique enables individually addressable NW devices. This is essential in device applications of mass sensing, but cannot be provided through existing cost-effective techniques such as self-assembly of NWs.

Field-directed assembly has been used for positioning single NWs and fabricating cantilevered nanosensors. However, finding the best parameter values enabling high yield of devices on a substrate has so far been possible only through time consuming and costly trial-and-error experimental efforts. In this work, a framework is introduced that enables choosing parameter values through systematic steps to increase the device yield. Different physical parameters and forces that disrupt NW assembly are discussed and guidelines to reduce the disruptors are provided. Understanding of the competition between forces serving as directors and disruptors enabled the definition and use of a single dimensionless parameter, the yield index, which provides a rational guide to the selection of parameter values, reducing costly trial-and-error efforts in experimental work. Biosensors enabling molecular diagnosis for early detection of disease and response to treatment are one of the promising applications.

In addition to single NW positioning, we demonstrate that field-directed assembly can be used to create multiple long NW chains between electrodes when the electrode gap size is much larger than the length of a single NW. In this method, we have shown how NW connectivity and configuration of the NW chains can be controlled through dipole-dipole interaction between NWs. This level of control cannot be achieved by using other low-cost techniques such as drop casting or spray coating of NWs. With such ordered chains made on a low-cost transparent substrate, the resulting transparent conductive substrate can be used in optoelectronic devices, such as solar cells and displays, where a low cost fabrication technique is required to create ordered NW arrays with end-to-end registry.

In this work, for the first time, field directed NW chaining is examined as a versatile and inexpensive fabrication method for transparent conductive substrates. Since neither corrosive chemicals nor elevated temperatures is involved in electric field assisted NW chaining, this method shows potential for creating NW networks on rigid as well as polymeric substrates. Chained NWs on a flexible substrate can combine electrical or thermal conductivity, optical transparency and flexibility which open new avenues for fabricating light-weight and flexible transparent electrodes for foldable displays, organic solar cells and several other devices.

Contents

Supervisory Committee **ii**

ABSTRACT **iii**

Table of Contents **v**

List of Tables **ix**

List of Figures **x**

Acknowledgements **xvii**

Dedication **xviii**

1 Introduction **1**
- 1.1 Why Nanoresonators? 2
  - 1.1.1 What Are the Difficulties of Nanoresonator Fabrication? . . . 3
  - 1.1.2 What is Missing in Previous Demonstrations of Directed Assembly? 5
  - 1.1.3 Research Contribution Toward Increasing the Yield of Nanoresonators 5
- 1.2 NW Network: Techniques for Fabricating Transparent Electrodes . . 6
- 1.3 Difficulties in Fabrication of Transparent Electrodes 7
  - 1.3.1 Research Contribution Toward Fabrication of Transparent Electrodes 8
- 1.4 Structure of the Dissertation 9

2 Assembly of Nanoresonators **11**
- 2.1 Why Bottom-Up Field-Directed Assembly? 11
- 2.2 Experimental Steps for Nanoresonator Assembly 14

2.2.1 Patterning the Substrate and NW Positioning 17
2.2.2 Clamping 20
2.3 NW Defects, Pre-clamped and Post-clamped Yield 21
2.3.1 Defects in NW Positioning 21
2.3.2 Protocols for Device Yield Measurement 22
2.4 Conclusions 25
2.5 Future Work 25

3 A Framework for Field-Directed Assembly of Single Nanowire 27
3.1 Introduction 28
3.2 Framework Development 30
3.2.1 Weakly-Coupled Disruptors 31
3.2.2 Strongly-Coupled Disruptors 35
3.2.3 Experimental observation: effect of strongly-coupled disruptors on assembly yield 38
3.2.4 Director-Disruptor Competition 40
3.2.5 Clamping 42
3.2.6 Towards a Generalized Director-Disruptor Framework 44
3.3 Conclusions and Outlook 47
3.4 Experimental Methods 48
3.4.1 Nanowire Synthesis 48
3.4.2 Nanowire Concentration Measurement 49
3.4.3 Nanowire Assembly 49
3.4.4 Nanowire Yield Measurement 50

4 Nanoresonator Measurement: Suitable Fabrication Design 51
4.1 Resonance Frequency Measurement Setup 52
4.2 Different Actuation Methods and Related Fabrication Design 54
4.2.1 Piezo Disk Actuation 54
4.2.2 Electrostatic Actuation 55
4.2.3 Fabrication Design Used for Piezo Disk and Electrostatic Actuation 56
4.3 Effect of NW Geometry on Performance of Nanoresonators 57
4.3.1 Nanowire Length 57
4.3.2 Nanowire Diameter 59

4.4 Conclusions 62
4.5 Future Work 63

5 Field-Directed Chaining of Nanowires 64
5.1 Introduction 65
5.2 Materials and Methods 65
5.3 Results and Discussion 66
5.3.1 Effect of Disruptors on Chain Formation 67
5.4 Conclusions 70
5.5 Acknowledgments 71

6 Fabrication of Transparent Electrodes on Rigid Substrates Using Field-Generated Forces 72
6.1 Transparent Electrodes 72
6.2 Experiments 75
6.3 Effect of Chain Configuration and Electrode Geometry on Light Transmittance 76
6.3.1 NW Chaining at 5 V (rms) 76
6.4 Conclusions 81
6.5 Future Work 81

7 NW Chaining on Flexible Substrate 82
7.1 Two Protocols 82
7.2 Experiments 84
7.2.1 Spin Coating 84
7.2.2 NW Assembly 85
7.2.3 Peeling 86
7.3 Assembly Parameters 87
7.4 Fabrication of NW Grid 88
7.5 Conclusions 91
7.6 Future Work 92

8 Conclusions 93

A Lift-Off Process 96

B Nanoresonator Integration Process 97

C Rhodium Nanowire Length 99

D Single Nanowire Positioning 100

D.1 Order of magnitude analysis of Brownian and dielectrophoretic displacement 103

E Chaining NWs 104

F Effect of Capillary on NW-Chains Configuration 105

G Grid-Shaped Assembly Electrode 106

Bibliography 109

List of Tables

Table 1.1 Summary of techniques applicable for NW network assembly . . 7

Table 3.1 Pre-clamped experimental yield (Exp. yield) at 10^4 Hz and 7 V (rms). Theoretical V_{eff}/V_{rms} was calculated using Figure 3.3(d). 39

Table 3.2 Table of comparison: identifying director and disruptor forces influencing the yield of single NW assembly in selected studies focused on increasing the yield of individually addressable single NWs. Effects marked by ‡ are classified as director or disruptor by us, based on qualitative information provided in the source. pDEP and nDEP refer to positive and negative dielectrophoresis. 46

Table 6.1 Effect of assembly-electrode thickness, for geometry used in our experiments, on light transmission (%T) of the resulting transparent electrode (TE). 80

List of Figures

Figure 1.1 (a) Single-nanowire assembly for nanoresonator integration, (b) chained-nanowires for fabrication of transparent electrodes. . . 2

Figure 2.1 Schematic of dielectrophoresis: (a) zero net force in uniform field prevents nanowire movement towards electrodes, (b) in a non-uniform electric field, nanowire moves toward the region of higher electric field. 13

Figure 2.2 Schematic of the nanowire (NW) synthesis and assembly: (a) NW synthesis in a porous template. After dissolving the template, NWs are released in a medium such as ethanol. (b) Bottom-up field-directed assembly of single NWs in photolithographically-patterned wells in a sacrificial photoresist layer. (c) Individual clamp windows were defined through a photoresist layer in which metal clamps were electrodeposited on clamp electrode. The photoresists were dissolved to suspend the clamped NWs above the driving electrode. 15

Figure 2.3 Two different fabrication designs used in this research work for nanoresonator integration: (a) design #1 and (b) design #2. In both designs, positioning electrodes are identified with red and green stars. Electrodes with white stars were used for driving the nanoresonators. Red dashed lines show the area patterned with electrode pairs and wells. 16

Figure 2.4 Importance of photoresist removal step. (a) Photoresist residual, due to incomplete cleaning step, covers NWs and disrupts the functionality of the NWs. (b) No photoresist residual after soaking substrate in high-temperature Microposit Remover 1165 for 8 hours. 19

Figure 2.5 Due to insufficient exposure and developing time, the photoresist was partly removed from clamp electrode. Clamp material was only deposited where photoresist was completely removed. . . . 20
Figure 2.6 Experimental result of pre-clamped NWs. Both images show that NWs were preferentially aligned in the wells, as marked with white arrows. Assembly defects including empty wells, short NWs, misaligned NWs, chained and bundled NWs are marked in these two images. 21
Figure 2.7 NW bundle and chain are the most common defects during NW assembly. High concentration of NWs is the main cause of these defects. 22
Figure 2.8 NW counting rules to evaluate pre-clamped yield: A NW with its chained end positioned on clamp electrode (red arrow) is considered in pre-clamped yield measurement. Where multiple functional NW are positioned between pairs of electrodes (white arrows), only one NW is counted per each pair. Green arrow shows a NW assembled next to an empty well. This NW can be clamped and create a functional nanoresonator. 23
Figure 2.9 NW resonators and the types of defects. 24

Figure 3.1 Schematics of positioning and clamping of single NWs on gold electrodes: (a) patterning electrode pairs with wells in between, to locate and trap NWs (b) positioning single NWs inside wells using DEP (c) electrodeposition of clamp material after photoresist removal from electrode surface (d) side view of clamped NWs after removing the remaining photoresist. 30
Figure 3.2 A cylindrical dam reduces the effects of drying-front capillary force as a disruptor and prevents NW spillover to adjacent dies. 32

Figure 3.3 Frequency changes affect the competing director and disruptor forces by altering (a) the magnitude of the DEP director as a result of the change in the magnitude of $Re[F_{CM}]$; (b) the electroosmotic force (F), a disruptor that drags NWs away from the assembly-electrode gap and (c) the electroosmotic velocity of disruptor fluid vortices. (d) The ratio of the effective voltage to the applied voltage for different gap sizes changes with frequency due to electrode polarization (a disruptor), modeled as an RC circuit(inset). 36

Figure 3.4 Experimental results showing the effect of applied voltage on preclamped yield at 10^5 Hz for three different gap sizes ($2x$). Larger gap sizes have higher threshold voltage (2, 1 and less than 0.7 V (rms) respectively for $2x$=10, 8 and 6 μm. Highest assembly yield occurs at 7 V (rms). 39

Figure 3.5 Single NWs aligned in almost every well (green arrows) at 10^5 Hz and 7 V (rms). Red arrows show misaligned NWs. 40

Figure 3.6 Director-dominant (green), disruptor-dominant (pink) and competing region (yellow) for water (a) and ethanol (b) with electrical conductivity of 5×10^{-3} and 2.19×10^{-5} Sm^{-1} respectively. The yield index for water (c) and ethanol (d) indicates the device yield as a result of competition between disruptors and directors in the competing region. For this comparison, electrode gap size was 10 μm and 1μm photoresist layer was considered on the electrodes. 41

Figure 3.7 Single-end-clamped nanoresonator using electrodeposited silver as clamp material, with inset showing the uniformity of the silver clamp around the NW. 43

Figure 3.8 High yield clamped single NW and defects. Green arrows: perfectly positioned and clamped NWs; blue arrow: a broken NW after clamping and removing photoresist; white arrow: NW bundle instead of single NW; orange arrow: no NW; red arrow: misaligned NW. 44

Figure 4.1 Schematic of mass detection. The shift in resonance frequency is caused by small mass attached to the nanoresonator. 51

Figure 4.2 (a) Laser setup used for resonance frequency detection. (b) Schematic of the measurement setup to measure the resonance of NW resonators. 52
Figure 4.3 A chip mounted on a piezo disk. The electrical feedthrough on the flange can be used to apply AC voltage for both piezo disk and electrostatic actuation. 53
Figure 4.4 Schematic of piezo disk actuation. 54
Figure 4.5 Schematic of electrostatic actuation. The AC voltage applied between the clamp and driving electrode is used to drive the NW. 55
Figure 4.6 FIB-milled slot used for isolating two bridged pads by removing part of a gold connection bar. 57
Figure 4.7 Two configurations of nanowire resonators with suspended length of l. 58
Figure 4.8 Effect of misaligned clamp mask. (a) Clamp mask was shifted to the left and caused (b) deposition of clamp material on the NW beyond the edge of the clamp electrodes while (c) remaining photoresist on the opposite edge, prevented deposition of the clamp material on the NW end placed over these edges. 59
Figure 4.9 Defective NWs grown inside AAO porous template. (a) Cross section of NWs grown inside AAO pores [63]. (b) Integrated nanoresonator. 60
Figure 4.10(a) Geometry of NWs extracted from polycarbonate porous membrane. (b) Resulting NWs show uniform geometry. (c) However, criss-crossed pore pattern causes NW clumps. 61
Figure 4.11Defects caused by NWs synthesized from polycarbonate template. (a) Clumped NWs can connect clamp and driving electrodes which prevents NW actuation electrostatically. (b) Synthesized single NWs can be short. 61
Figure 4.12Nanoresonator integrated from polycarbonate-synthesized NWs, assembled and clamped using design #2. 62

Figure 5.1 Sketch of (a) single NW positioning ($L_{gap}/L_{NW} < 2$) and (b) NW chaining (L_{gap} /$L_{NW} \geq 20$). 67

Figure 5.2 (a) L_{gap}=180 μm (b) L_{gap}=240 μm. In (b), capillary force disconnects the bridged chains (marked with red circle). The direction of the drying front of the medium is indicated with blue arrows 68
Figure 5.3 Disruptor results: effect of increasing voltage from (a) V_{rms}= 5 V to (b) 7 V. (c) and (d) hovering NWs prevent a short circuit. 69
Figure 5.4 Resistance measurement for chains of L_{gap}=180 and 240 μm. . 70

Figure 6.1 Effect of applied electric field on NW connectivity. 10 μl of NW suspension was introduced over both substrates (a) no electric field was applied, (b) an AC field with 5 V (rms) at 10 kHz was applied to the electrodes. 75
Figure 6.2 Chain configuration alters as assembly-electrode gap size changes from (a) 120 μm to (b) 180 μm and (c) 240 μm. The frequency and magnitude of applied voltage for all three experiments were 10 kHz and 5 V (rms) respectively. 77
Figure 6.3 Light transmission results from substrate patterned (a) with blank electrodes with gap sizes of 240 μm, 180 and 120 μm and (b) with NW chains between different electrode gap sizes. NW chain assembly occurred at 10 kHz and 5 V (rms). 78
Figure 6.4 The effect of assembly-electrode thickness on light transmittance of the substrate. Transmittance measurement for glass substrate coated with 15 nm Ag layer (blue line), is taken from Ref. [104]. Electrodes with 10 nm Cr/100 nm Au layer (red line) were used in this work. Vertical dashed lines represent the percent of covered area for assembly electrodes with 120, 180 and 240 μm gap size. 79
Figure 6.5 Schematics of thin film grid pattern. 80

Figure 7.1 Two different protocols for NW assembly on a flexible substrate using field-generated forces. (a) NW assembly on a patterned plastic substrate (b) NW assembly on a polymer layer coated on a patterned rigid substrate. Polymer is partially removed from the electrodes (see red arrows) enabling electrical contact. . . . 84
Figure 7.2 (a) Nonuniform thickness of polymer. (b) and (c) show that more NW chains are generated over thinner parts of polyimide layer. 85

Figure 7.3 (a) Peeling NW-patterned polymer from a rigid substrate. (b) SiO_2 layer was deposited on the substrate to assist peeling the NW-patterned polymer. Oxide layer was partially etched from positioning electrodes to enable electrical connection between probe tips and electrodes. 86

Figure 7.4 Effect of frequency on chain formation: (a) 100 kHz, (b) 10 kHz. In both cases, electrode-assembly gap size is 240 μm. 87

Figure 7.5 Chain growth at 7 V (rms) and 100 kHz between electrodes with 240 μm spacing. NW chains remain short due to small field-generated forces. 87

Figure 7.6 NW chain bridging electrodes with 120 μm gap size. Assembly voltage and frequency used were 7 V (rms) and 100 kHz respectively. 88

Figure 7.7 Peeled NW-patterned polyimide. High van der Waals force between NWs and polymer prevents chain destruction during peeling of the polymer. 88

Figure 7.8 Grid-shaped assembly electrode detailed at right of figure. . . . 89

Figure 7.9 Alternating applied voltage to (a) horizontal, (b) vertical assembly electrodes. 90

Figure 7.10 NW grid formation. (a) 120 μm and (b) 300 μm electrode spacing. Smaller field-generated forces in (b) caused less ordered patterns of connected NWs showed in (c). 90

Figure C.1 SEM images of the rhodium nanowires extracted from anodized alumina membranes (AAO from Whatman). Dominant length ranged between 8 to 12 μm. 99

Figure D.1 Effect of NW concentration on NW assembly yield: (a) high concentration of NWs reduces the device yield due to presence of so many NW clumps on the substrate. (b) decreasing the concentration to 19×10^5 NW/mL increases the number of wells filled with single NWs (green arrows). 100

Figure D.2 Optical micrograph of nanowire assembly defects. Nanowires are preferentially positioned inside wells. Defects such as bundled, chained and empty sites are considerably reduced by appropriate choice of nanowire concentration range. Misaligned nanowires, shown attached to the photoresist surface, are removed with the photoresist. 101

Figure D.3 High pre-clamped yield of nanowires. Where multiple nanowires are positioned in between some electrode pairs, only one nanowire per electrode pair is counted, to determine the assembly (pre-clamped) yield. 101

Figure D.4 SEM image of post-clamped defects. Empty sites, bundled or multiple nanowires less than 10 μm apart and short nanowires were not counted as functional nanoresonators. If the free end of a clamped nanowire reaches the edge of the counter electrode below, it is counted as functional device. 102

Figure D.5 Optical image of clamped nanowires showing high yield after photoresist removal. Dark rectangles are the silver clamps. . . . 102

Figure E.1 Schematic of interdigitated electrodes. 104

Figure E.2 Using a dam to increase available time (before alcohol evaporates), for creating multiple chains bridging the electrodes. . . . 104

Figure F.1 Effect of capillary force at the NW suspension drying front on configuration of NW chains. Assembly-electrode gap size is 240μm. Capillary force can break the bridged chains. Small chain segments agglomerate on the substrate. 105

Figure G.1 Three different photolithography masks designed by using L-Edit software. 108

ACKNOWLEDGEMENTS

I would like to thank:
My supervisor, Dr. Rustom Bhiladvala, who trusted me and shared his deep knowledge about nanofabrication with me. He was always being patient and supportive when work was slowed down. I also wish to extend my thanks to the members of my committee Dr. Martin Jun and Dr. Bradley Buckham.
Nathanael Sieb and Grace Li at Simon Fraser University 4D LABS for their guidance on using nanofabrication facilities and help with the experiments.
My friend and former colleague Dr. Nima Moghimian who always helped me with his knowledge and friendship.
Dr. Rodney Herring, Adam Schuetze and Dr. Elaine Humphrey for their support with SEM, FIB and other tools at Advanced Microscopy Facility.
Dr. Alex Brolo and Mahdieh Atighi for the use of Brolo's Lab.
My group members: Fan Weng, Jehad Alsaif and Amin Ebrahiminejad for their help with the experiments. My friend and former colleague Ali Etrati for all the fun moments.
My sister Farnoosh and my nephews Behdad and Neema with whom I shared all my hopes and disappointments. They were always there for me when I was sad or hopeless.
My best Friend Mana Norouzpour who gave me a heart full of joy and always supported me with her friendship.
My dear friend Stanislaw Kania for his love and devotions throughout the ups and downs of this period of my life.
And last but not least, my beloved parents Habib and Simin and my sisters and brother Felora, Sanaz and Farhad for their lifetime support.

DEDICATION

To my beloved parents: Simin and Habib

Chapter 1

Introduction

Rapid advances in synthesis and assembly of nanomaterials into functional systems, enable use of the extraordinary capabilities of nanostructures in various areas. Some examples are in biomedicine (*e.g.* artificial skin [1], in vivo mapping of brain activity [2] and early-stage disease detection [3]), electronics (*e.g.* field-effect transistors [4, 5]), transparent electrodes applicable to devices such as display screens, LEDs and solar cells [6–9], and gas sensing [10–13]. Using nanomaterials for these systems is important because some properties such as high sensitivity or mechanical flexibility are pronounced at nanometer dimensions. Various fabrication techniques have been utilized for assembly of single [3–5, 14] and connected or chained nanostructures [6–9, 15–17]. However, there are difficulties associated with existing techniques that lead to high cost or low throughput of resulting devices.

In this research work, a cost-effective field-directed assembly technique is developed to enable ordered positioning of nanowires (NWs) covering a large surface area. We propose a framework based on classifying physical forces and demonstrate its systematic use to enable a high yield of nanodevices. This research, demonstrating assembly control for low-cost fabrication of large numbers of nanodevices, provides a path towards nanomanufacturing.

To demonstrate the capability of this technique for single-NW assembly and NW-chains, two possible applications that can benefit from simple and cost-effective fabrication were considered: biosensing and transparent electrode (TE). In biosensing, a large number of single-NW resonators (nanoresonators) are required to be assembled and addressed individually in order to be used for early detection of disease (Figure 1.1(a)). In TE, chains of NWs with controllable chain density and NW connectivity are needed to create reasonable electrical conductivity and optical transparency

(Figure 1.1(b)). TEs are important component of devices including LEDs and solar cells. For each application, development of fabrication mechanisms and steps, possible defects that can occur during fabrication and guidelines to prevent these defects, are provided in this work.

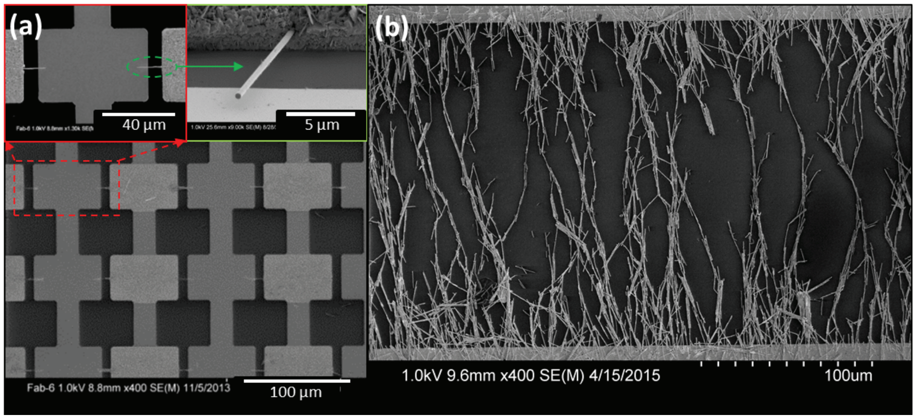

Figure 1.1: (a) Single-nanowire assembly for nanoresonator integration, (b) chained-nanowires for fabrication of transparent electrodes.

1.1 Why Nanoresonators?

Nanoresonators are submicron-sized structures such as wires and beams, clamped at one or both ends (single- or double-end clamped), that can be driven into vibration around a resonant frequency, by using one of a number of different actuation techniques [18]. Nanoresonators are of technological interest in mass and force measurement because of their high sensitivity. In a recently published work [19], a single proton mass resolution (10^{-24}g) was demonstrated using a double-end-clamped nanoresonator. Such extraordinary resolution in mass detection of these submicron-sized devices enables us to anticipate nanoresonator applications in biological research and engineering.

Examples of using single- or double-end clamped nanoresonators in engineering are the characterization of mechanical [20–23] and electrical [20, 24, 25] behavior of NWs and nanotubes, to enable technological goals such as actuation and detection of their sub-nanometer displacements at high frequencies. The high sensitivity of nanoresonators will have an important role in healthcare as demonstrated for early-stage cancer detection [3]. However, commercialization of these nanodevices is challenging due to high fabrication cost or low device yield. The first part of this Ph.D. research is focused on using a cost-effective fabrication technique for single-end clamped nanoresonator assembly. Difficulties attributed to fabrication of high-yield functional nanoresonators, required for nanomanufacturing of biosensors, are noted and an approach to solve the issues is provided.

1.1.1 What Are the Difficulties of Nanoresonator Fabrication?

Although the extraordinary sensitivity of nanoresonators is poised to yield a breakthrough in early detection of disease, device manufacturing poses challenges in commercializing the devices. The intrinsic stress from fabrication which causes nonlinear geometric effects during transduction (driving and detection of vibration) [26], high fabrication cost and low device throughput, are some examples of these challenges which limit nanodevices to research laboratory demonstrations. To understand these challenges, it is helpful to look at families of techniques –bottom-up, top-down and hybrid bottom-up directed-assembly [27–30]. The methods and challenges attributed to each one are briefly explained below.

The term top-down methods [27,28,31] often refers to manufacturing micron- and nano-sized structures by patterning larger scale bulk materials. Photolithography can be utilized to create patterns in a photoresist layer by using ultraviolet light (typically 250 nm wavelength). This is a suitable technique for creating micron-sized structures. In order to pattern nano-sized structures, smaller wavelengths are required. Nanostructures can be patterned using electron-beam lithography (EBL) and focused-ion beam (FIB) [27,28]. The pattern is then transferred to the substrate either by etching into the substrate (subtractive pattern transfer) or selectively filling the patterned area with a desired material (additive pattern transfer).

Nanoresonators, with the feature size of tens to hundreds of nanometers, have been made by EBL and FIB lithography [19, 28]. However, covering large area for making commercial sensor arrays by using EBL or FIB is time-consuming. Also, the high cost of operating equipment does not allow inexpensive production of large-area sensor arrays. The shortcomings of well-established top-down techniques for making nanoresonators have led to an alternative family of fabrication techniques.

Bottom-up methods are identified by their use of the assembly of smaller units into larger structures, for example, single nanoresonator elements assembled and integrated into arrays for sensing. Self-assembly [24,33,34] (formation of ordered structures from disordered ones without applying external forces) provides a low-cost and efficient way for creating nanostructures with critical dimensions below photolithographic resolution limits. The formation of self-assembled structures is a defining example for a bottom-up approach towards the fabrication of nanostructures. A significant advantage over top-down methods is that various nanoscale materials with different shape, size and crystallinity, synthesized off-chip, can be assembled on the chip. The elements may also be functionalized off-chip to capture different sensing targets on the same chip (multiplexing) [35]. However, clamping and addressing individual nanostructure assembled on a substrate by using self-assembly is not easily done.

To drive the nanoresonators and detect their vibration individually, each NW needs to be positioned and clamped at pre-determined places on a substrate. What fabrication technique can we use to make a large array of individually addressable nanostructures with low cost?

A hybrid strategy of combining photolithographic patterning of the substrate, borrowed from top-down methods, and the flexibility of using stress-free individual nanostructures, provided by bottom-up method, can partially overcome the difficulties of each method. An example of this strategy, called bottom-up directed-assembly, was demonstrated by Li *et al.* [14]. In this technique micron-sized electrodes are patterned on a wafer using photolithography. NWs synthesized off-chip, suspended in a medium, are introduced over the substrate. Applying an AC electric field between electrode-pairs patterned on the substrate generates a dielectrophoretic (DEP) force [36–38] exerted on the NW due to the induced dipole moment and the non-uniform electric field at the electrode edges. Electrode patterning allows this force to be used to position and align NWs in designated places on the substrate. Thick metal clamps are then electrodeposited on the assembly electrodes to clamp the positioned NWs and each of the integrated nanoresonators can then be individually addressed. While this hybrid bottom-up directed-assembly technique enables the assembly of individually addressable nanoresonators at low cost, the device yield needs to be improved in order to extend this towards cost-effective nanomanufacturing.

Yield enhancement of the nanodevices fabricated by this hybrid technique has been studied in a few research labs [14,25,39–42]. The main challenge in using DEP force in bottom-up directed assembly is the disruptive effect of several forces and physical parameters that prevent DEP from directing NWs into pre-patterned places on the substrate and subsequently decrease the device yield. Dissociating disruptive effects and forces from the DEP director is not always easy since the electric field required for DEP assembly also triggers disruptor forces (*e.g.* negative DEP and electroosmotic force) simultaneously. A common approach in all studies is to run a different set of experiments and try to find the best positioning parameters by trial-and-error. As will be explained in Chapter 2 and 3, there are several parameters that affect NW positioning yield such as electrode geometry, electrical properties of the medium and NW, concentration of NWs in the suspension, amplitude and frequency of applied field. The large number of variables causes an extensive experimental effort when using trial-and-error. This can be avoided by using a framework that helps us choose the right parameter values.

1.1.2 What is Missing in Previous Demonstrations of Directed Assembly?

Utilizing the extraordinary sensitivity of nanoresonators in commercialized devices for disease diagnosis and healthcare is not possible without increasing the device yield by using a cost-effective method. However, increasing the device yield faces many challenges. The number of variables affecting the device yield is large and due to imperfect understanding of all variable effects, a yield reported by one published work may not be reproducible by a new user using different assembly setups or different materials and experimental parameter values. Several physical effects can be coupled together but there are few studies on understanding the underlying physical phenomena and coupling effects. As a result, if a researcher needs to change a single fabrication step or using a different material, the large dimension of the parameter space causes considerable effort in a trial-and-error approach to obtain high device yield. The cost of substrate fabrication and the large amount of time required for trial-and-error is the main challenge in improving the device yield.

1.1.3 Research Contribution Toward Increasing the Yield of Nanoresonators

In this work, underlying physical phenomena that contribute to device yield in field-directed assembly of NWs were studied. As a result of this study, a framework, applicable for all field-directed assembly methods, was introduced for identifying disruptor and director forces. To achieve that, disruptive forces and parameters that prevent directing NWs into pre-determined places were studied and classified as weakly-coupled or strongly-coupled to the director force (DEP). This framework enables reduction of the disruptors by following simple guidelines and reducing the time and cost required if choosing the assembly parameter values solely by experiment. With assistance from this framework, the highest yield of integrated nanoresonators, compared with previous similar studies, was achieved in this Ph.D. research.

In previous studies of field-directed assembly of NWs limited work has been done on the possible coupling between several physical effects. This work investigated effect of coupling between different forces and parameters in field-directed assembly of NWs and its use to reduce the time and cost associated with trial-and-error method. The framework introduced here is a significant step towards commercial and scientific use of nanoresonators.

1.2 NW Network: Techniques for Fabricating Transparent Electrodes

The second part of this Ph.D. research is associated with describing field-assisted NW chaining in order to create a high density of parallel NW chains on a substrate. The assembly parameters required for chaining differ from those for single NW assembly. As described in this work, field-directed chained NWs can create networks of ordered, connected NWs that enable fabrication of rigid and flexible transparent electrodes (TEs).

Organized collections of NWs can be used as TEs for use in devices such as optoelectronics (e.g. LEDs or solar cells) [43–48]. The main challenge in assembly of a network of NWs is the delivery of NWs onto substrates of interest with control over connectivity. In principle, generating organized, connected NWs from disorganized suspension requires external forces to overcome Brownian motion and to introduce end-to-end connectivity in the final configuration. The most common techniques carried out for the formation of NW network are summarized in Table 1.1.

Table 1.1: Summary of techniques applicable for NW network assembly

Method	Advantages	Disadvantages	Ref
Flow of NW suspension in microchannels	• Different assembly direction is possible, depending on flow direction • Compatible with both rigid and flexible substrate	• Area of NW assembly is limited to the size of microchannels • Difficult to assemble high density of NW array	[33, 34]
Dry Transfer	• Provides assembly into desired configurations • Applicable for large area assembly • Compatible with both rigid and flexible substrates • Different assembly direction is possible	• Adhesion between nanomaterials and the surfaces of the stamps need to be engineered	[49, 50]
Drop casting and spin coating	• Easy to conduct • Applicable to large area assembly •Compatible with both rigid and flexible substrates • NW assembly process is fast	• Inhomogeneous NW assembly • Difficult to achieve high reproducibility • NW surface functionalization is required to prevent agglomeration	[16, 51–53]
Spray coating	• Easy to conduct • Applicable to large area assembly • Compatible with both rigid and flexible substrates	• Difficult to achieve high reproducibility	[54, 55]
Nanoimprinting	• High resolution • High control of assembly into desired configurations	• Complex, several steps are required • Not applicable for large area assembly • Requires original stamps containing prefabricated nanostructures	[56]

1.3 Difficulties in Fabrication of Transparent Electrodes

Several techniques, mentioned in Table 1.1, directly use NWs to create the network. In addition to these methods, electrospinning [57, 58] and electron beam lithography (EBL) [59] have also been utilized for fabrication of high performance TEs. However, in these techniques NWs are not directly used and a network of wire-shaped conductive material covers all substrate. Electrospining is applicable for large-area coverage, but requires several steps of depositing and dissolving materials which make this method complex and time-consuming. EBL has high resolution and control over assembly into desired configurations, however, it is an expensive technique and not applicable for large area fabrication. Complexity and the high cost of making large-size TEs by using these methods promote investigation of other techniques such as drop casting, spin coating and spray. Although these are simple and low-cost techniques, it is difficult to achieve reproducible electrical and light transmission properties by using these methods since NW connectivity and configuration of the NW network cannot be easily controlled.

One cost-effective technique for creating end-to-end connectivity of NWs is applying an electric field to a drying suspension of NWs. In this technique, NW connection is controlled by the gradient of the applied field and by induced dipoles. Short NW chains (1-3 μm long) generated by this method on rigid substrates have been used as sensors [11,12]. However, covering a large area with long chains is challenging due to the disruptive effect of capillary force that tends to destroy chains at the drying front of NW suspension during medium evaporation. Another issue is an electrical short circuit that prevent more NW chain growth after the first chain bridges and make contact with assembly electrodes. The question to be answered is if field-generated forces are capable of covering large surface area with long chains? How can we prevent electrical short circuits to generate parallel chains between assembly electrodes to fabricate high-performance TE? To answer thess questions, we need to know what the chain formation process is, which parameters and forces are involved in chain formation and how to harness these parameters to create a large-size TE.

1.3.1 Research Contribution Toward Fabrication of Transparent Electrodes

Field-directed chaining of NWs shares the simplicity of drop-casting and spray, in that multiple fabrication steps or complicated and expensive equipment are not needed. However, it uses dipole-dipole interaction to enable control of the connectivity of NWs missing in spin coating and spray techniques. The major difficulties in using field-directed NW chaining for TE fabrication are the effect of capillary force at the medium drying front that can break the NW chains and electrical short circuit when first chain bridging assembly electrodes that stops further chain growth.

In this work, forces and physical parameters involved in field-directed NW chaining were studied. Specifying and eliminating disruptor forces and parameters enabled choosing parameter values that provide large enough director force to create multiple long NW chains.

To the best of the author's knowledge, no investigation results have been reported on electric field assisted NW assembly on flexible substrates. Due to the high demand for a new generation of flexible devices such as foldable displays and flexible organic solar cells, fabrication techniques that can be used for both rigid and flexible substrate are preferred. The capability of this technique for NW assembly on both rigid and flexible substrates is demonstrated in this research in Chapters 5 to 7. This technique provides a basis for development of a scalable and cost-effective technology to fabricate versatile, high performing devices on both rigid and flexible substrates.

1.4 Structure of the Dissertation

This dissertation presents advances in electric field assisted NW assembly for two different applications: 1- biosensing (individually addressable single NW resonators) and 2- transparent electrodes (covering large surface area with chained NWs). Following an explanation of fabrication steps for nanoresonator assembly, a framework is introduced to guide fabrication of high yield devices and reduce experimental effort. Field-assisted NW chaining is then explained followed by demonstration of the fabrication of high-performance transparent electrode by using NW chains on glass substrates. NW chain fabrication on a flexible substrate is also demonstrated as a proof-of-concept. The last chapter lists the main conclusions from this dissertation.

There is no separate methods section or experimental chapter in this document. The methodological details have been presented in each chapter as needed. In cases where the experimental details are long, the reader is directed to Appendices. The relevant background and literature review are presented in each section where needed, to avoid a single exhaustive literature review chapter. Each chapter terminates with a Conclusions and Future Work section.

Chapter 2 briefly describes the principles of dielectrophoretic force and electric field-directed assembly. The fabrication steps, defects that may occur during assembly of NW resonators as well as guidelines to prevent the defects are summarized.

Chapter 3 presents a peer-reviewed, published journal paper [1] with results and discussion on director and disruptors of single NW assembly. A framework is presented that enables the classification of disruptor and director forces, increasing the device yield by decreasing or eliminating the effect of disruptors and reducing trial-and-error in experimental effort.

Chapter 4 introduces the actuation and detection techniques for nanoresonators. Based on limitations associated with different actuation techniques explained here (piezo disc and electrostatic), the particular fabrication requirements are explained. Suitable design for nanoresonator integration and detection via each of the actuating techniques is introduced.

Chapter 5 presents a peer-reviewed, published journal paper [2] [60] on the process of NW chaining. Forces involved in this process and the difference between field-assisted single NW assembly and NW chaining are explained.

Chapter 6 demonstrates a cm-size transparent electrode fabricated on a glass substrate by using field-assisted NW chaining. The resulting TE presents high light transmittance and electrical conductivity.

Chapter 7 presents capability of electric-field-assisted NW assembly for positioning NWs on flexible substrates. Two protocols are introduced and results of NW chaining on polyimide substrate are demonstrated.

Chapter 8, Conclusions, summarizes the main contributions of this Ph.D. research.

---

[1] Mahshid Sam, Nima Moghimian, Rustom B. Bhiladvala. "Field-directed assembly of nanowires: identifying directors, disruptors and indices to maximize the device yield." *Nanoscale* 8 (2016): 889–900

[2] Mahshid Sam, Nima Moghimian, Rustom B. Bhiladvala. "Field-directed chaining of nanowires: Towards transparent electrodes." *Materials Letters* 163 (2016): 205–208

Chapter 2

Assembly of Nanoresonators

This chapter describes the process of making nanoresonators by using the bottom-up field-directed assembly technique. Several steps are involved in the assembly of the nanoresonators which are explained in this chapter. The defects that can occur during the NW assembly and fabrication of nanoresonators are presented towards the end of this chapter.

2.1 Why Bottom-Up Field-Directed Assembly?

The high sensitivity of nanoresonators introduces a potential technology for molecular diagnosis at an early stage of disease, when small concentrations of disease biomarker molecules are present. This can be enabled by functionalizing nanoresonators for specific binding of target biomarker molecules and using the frequency shift following target binding [3, 35]. This extraordinary sensitivity can make a significant contribution to healthcare and biological research if device yield can be increased at reasonable cost. The great impact of utilizing nanoresonators on our life motivated me to study and investigate a technique that enables mass production of such devices. The aim of this Ph.D. research is to introduce an approach that allows laboratory demonstrations to be extended to commercially available devices.

By combining off-chip NW synthesis and field-directed assembly with conventional bottom-up microfabrication, several shortcomings of current fabrication methods can be resolved. In top-down techniques, NWs are patterned and etched from a thin semiconductor film or a thin metal film sputtered or evaporated on the substrate. The residual stress, resulting from thermal stress during film deposition, can de-form the nanoresonator [61, 62]. This defect is eliminated by using NWs synthesized off-chip. The use of undistorted NWs simplifies the frequency peak detection and related measurements. Whereas in top-down techniques, all nanoresonators on a substrate are constructed to have the same material, bottom-up field-directed assembly enables integration of NWs of different materials [40] that are processed or functionalized off-chip [35]. Differently functionalized NWs can detect different disease marker molecules on the same chip to provide multiple-target biosensor arrays (multiplexing).

Another fabrication issue that has been addressed by bottom-up field-directed assembly method is the fabrication cost for a large array of individually addressable nanodevices. A large number of single NWs can be fabricated by self-assembly technique [24, 33, 34] but the NWs cannot be addressed individually. Electron beam lithography can be utilized to make contacts for addressing the NWs, but this is an expensive and time-consuming method. However, bottom-up field-directed assembly allows fabrication of individually addressable NWs with high yield and low fabrication cost as described in this chapter.

This hybrid technique has been used previously by Li *et al.* [14]. However, in this research, significant gains have been realized during NW assembly by introducing a framework to help selection of parameter values. Using this framework, higher device yield is realized compared with the reported yield by Li *et al.* [14]. Without using such an established assembly principle as a baseline for comparison, the high device yield in this work could be due to a new assembly protocol, utility of the framework or both. This chapter details the fabrication steps after describing dielectrophoretic (DEP) force.

DEP force is exerted on a polarizable particle when it is subjected to a non-uniform electric field [36–38]. The principle of DEP is illustrated in Figure 2.1. In a uniform electric field, as shown in Figure 2.1(a), the net force due to Coulomb interaction between the polarized particle and the electrodes is zero. However, in a non-uniform field (Figure 2.1(b)), the electric field gradient is higher on the right side of the particle, therefore, there is a net force acting on the particle in the direction of higher field strength. In this simple explanation, the effect of the medium was neglected. However, in the general case, the polarization of the medium should also be considered.

Eq. (2.1) and (2.2) show that DEP force (F_{DEP}) depends on electrical properties of medium and particle. In these equations l and r are length and radius of NW, ϵ_m is permittivity of the medium and E_l is the electric field. Re[F_{CM}] is the real part

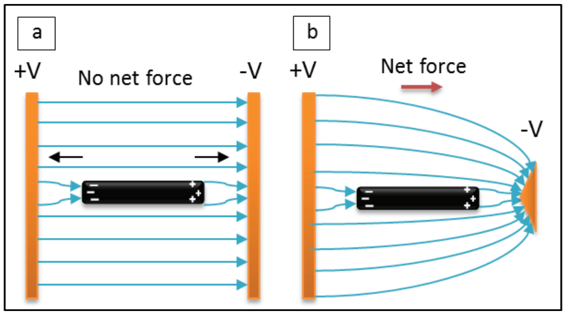

Figure 2.1: Schematic of dielectrophoresis: (a) zero net force in uniform field prevents nanowire movement towards electrodes, (b) in a non-uniform electric field, nanowire moves toward the region of higher electric field.

of the Clausius-Mossotti factor that depends on ϵ_p^* and ϵ_m^* (complex permittivity of NWs and medium respectively). The complex permittivity defined as $\epsilon^* = \epsilon - j(\frac{\sigma}{\omega})$ where ω is the angular frequency of the applied electric field and σ is the electrical conductivity.

$$F_{DEP} = \frac{\pi r^2 l}{6} \epsilon_m Re[F_{CM}]. \bigtriangledown (E_l^2) \tag{2.1}$$

with

$$F_{CM} = \frac{\epsilon_p^* - \epsilon_m^*}{\epsilon_m^*} \tag{2.2}$$

Re$[F_{CM}]$ can be positive or negative. The sign of the Re$[F_{CM}]$ introduces two classes of DEP force: positive and negative DEP. In positive DEP (pDEP), a particle with higher polarizability than the surrounding medium is pushed toward the region of higher electric field (electrode edges). If the suspended particle has a polarizability smaller than the surrounding medium, the particle is pushed toward the region of weaker electric field (away from electrode edges), and this phenomenon is called negative DEP (nDEP).

In this research, in order to position NWs, arrays of microscale assembly electrodes were first fabricated on the substrate by using photolithography. Ultraviolet (UV) light (near-UV or deep-UV) is used in photolithography to transfer a pattern through a mask to a photoresist. Creation of micronscale assembly electrodes over the whole wafer with a single exposure replaces the rastering of an electron-beam required to pattern nanostructures in place over a large area. Borrowing this step from additional top-down methods to avoid electron-beam lithography (EBL) allows large area nanofabrication at greatly reduced cost. The smallest feature size in this work is

2 μm which can be patterned using UV light with 250 nm wavelength. Details about patterning the substrate are discussed in section 2.2.1 after noting experimental steps.

Contact printing [28] is also another fabrication technique in which a stamp (most frequently made of PDMS) is used to transfer a solid or liquid ink onto a surface. This is a low cost technique for fabricating micron-sized electrodes. However, compared to photolithography, contact printing has lower resolution for aligning different layers.

2.2 Experimental Steps for Nanoresonator Assembly

In this work, rhodium (Rh) NWs synthesized by electrodeposition in a porous membrane have been used. The synthesis of NWs was done by my colleague Nima Moghimian and a detailed discussion is provided in his Ph.D. dissertation [63]. Two different templates were utilized in NW synthesis: anodized alumina membranes (AAO) with 200 nm nominal pore size and thickness of 60 μm (Whatman) and polycarbonate (PC) membranes with 400 nm nominal pore size and thickness of 20 μm (Sterlitech). Schematic of synthesized NWs in a porous membrane is shown in Figure 2.2(a). Rh NWs were grown by electrochemical deposition inside nanoporous membranes from a commercial sulfate-based solution (RH221D from Technic) at a constant potential of -400 mV with respect to a Ag/AgCl reference electrode with duration of 1 hour. A thin (0.5 μm) silver contact layer was evaporated on one side of either type of membrane to provide electrical connection (Figure 2.2(a)). The grown NWs were extracted from the template by dissolving the silver (in nitric acid) and the membrane material (AAO membrane in 3M NaOH and PC membrane in dichloromethane). Following this, NWs were rinsed in water and then rinsed and stored in ethanol. Synthesized NWs, suspended in ethanol, were then assembled on a pre-patterned substrate by using DEP force.

From NW positioning to assembly of the nanoresonators, three main steps are involved: 1- patterning the substrate using photolithography, 2- positioning the NWs using DEP force and 3- clamping the NWs by electrodeposition of clamp material. For these steps, three different masks were designed to pattern the substrate and clamp the NWs.

The first mask (“electrode” or “Mask 1”) was used to pattern substrates to create assembly electrodes, on which, NWs were positioned. These electrodes, after NW

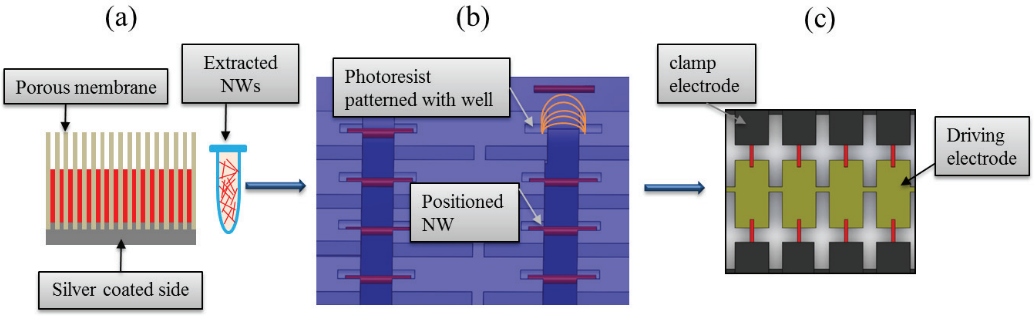

Figure 2.2: Schematic of the nanowire (NW) synthesis and assembly: (a) NW synthesis in a porous template. After dissolving the template, NWs are released in a medium such as ethanol. (b) Bottom-up field-directed assembly of single NWs in photolithographically-patterned wells in a sacrificial photoresist layer. (c) Individual clamp windows were defined through a photoresist layer in which metal clamps were electrodeposited on clamp electrode. The photoresists were dissolved to suspend the clamped NWs above the driving electrode.

positioning, were also used for electrodeposition of a metal clamp to fix one end of the NWs. A second mask ("wells" or "Mask 2") was used to pattern wells in a photoresist layer. This mask was aligned with the electrodes to create wells in between each pair of electrodes. Well ends were places with a higher gradient of the electric field, which promoted NW positioning inside wells as shown in Figure 2.2(b). The third mask ("clamp" or "Mask 3") was used to pattern clamp windows and expose electrodes which were used to attach one end of positioned NWs to the substrate as demonstrated in Figure 2.2(c). NWs were positioned between two electrodes. One electrode was used for clamping and also served as one of the driving electrodes. The other served as the second driving electrode, for driving the NWs. To prevent confusion, the electrodes on which clamp material were deposited are named "clamp electrodes" and the opposite electrodes that were used for NW driving, are named "driving electrodes".

The steps described above can be easily used to fabricate double-end clamped NWs with a slight modification in the design of the third mask ("clamp") enabling deposition of clamp material on both ends of positioned NWs. Double-end clamped NWs have been used for measuring mechanical properties of NWs [64] as well as for mass [19, 65], gas [66] and UV-light [67] sensing.

In this work, two different patterns were designed and fabricated as shown in Figure 2.3(a) (design #1 (D1)) and (b) (design #2 (D2)). Each fabrication design is suitable for a different actuation method as explained in Chapter 4. Red dashed lines in the inset images of Figure 2.3 identify the NW positioning areas where wells are patterned between electrodes. All clamp electrodes in each die are connected to a main clamping electrode, that is marked by red stars in the inset image of Figure 2.3, and was used for electrodeposition of clamp materials . This electrode with electrodes marked with green stars, were used for applying electric field on the substrate. In design #1 (D1) all driving electrodes are connected together while in design #2 (D2), every group of five adjacent driving electrodes are connected to a separate electrode. White stars in the inset images of Figure 2.3(a) and (b) show the electrodes to which all electrodes (in D1), or each of the five driving electrodes (in D2) are connected.

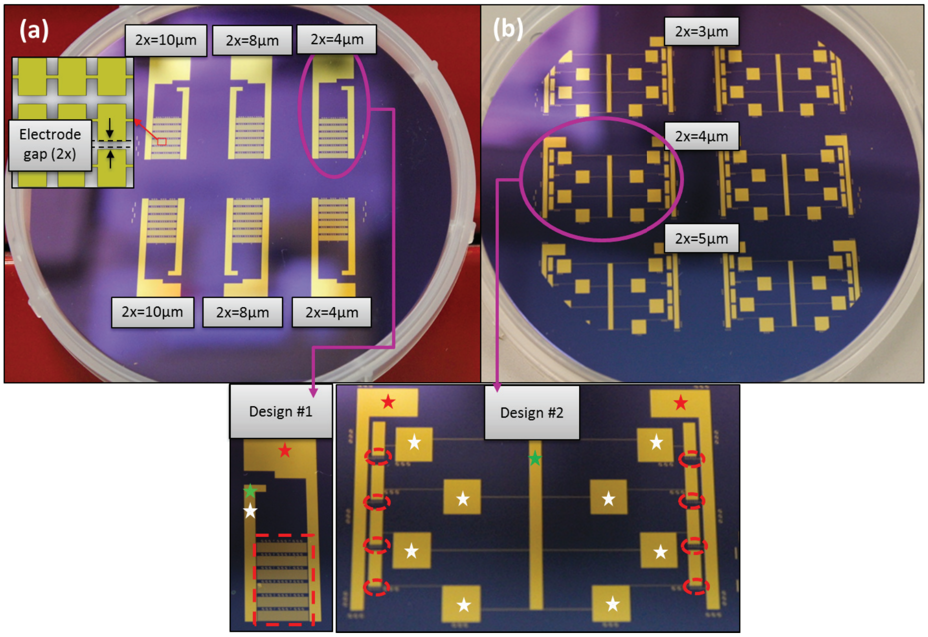

Figure 2.3: Two different fabrication designs used in this research work for nanoresonator integration: (a) design #1 and (b) design #2. In both designs, positioning electrodes are identified with red and green stars. Electrodes with white stars were used for driving the nanoresonators. Red dashed lines show the area patterned with electrode pairs and wells.

The gap between driving and clamp electrodes, $(2x)$, is identical in each die yet different from other dies (see Figure 2.3). This allows assembly of NWs with different length. The ratio of NW length to electrode gap can affect fabrication of functional nanoresonators. NWs need to be long enough to have an overlap with clamp and driving electrode to enable NW clamping and resonance measurement. However, the ratio between the NW length and the electrode gap size is not only important for NW clamping and resonant measurement, it is also an effective parameter for NW positioning inside wells. If this ratio is much higher than 2, a misaligning torque can rotate NWs from being parallel to wells to perpendicular position [68]. The details of the effect of NW length on NW assembly are described in Chapter 3.

2.2.1 Patterning the Substrate and NW Positioning

Here, details of the fabrication steps are provided. Fabrication starts with assembly electrodes, using a metal lift-off process (see Appendix A) on a 4-inch silicon wafer with 300 nm thermally grown silicon oxide. A ∼100 nm LOR 2A photoresist (MicroChem) layer was spun (4000 RPM) and baked (for 2 min at 180 °C) as an adhesion layer followed by spin coating a 1 μm-thick AZ703 photoresist (AZ Electronic Materials) with a spin speed of 4500 RPM for 45 seconds. AZ703 Photoresist was then baked on a hotplate at 90°C for 1 minute followed by 1 minute at 110°C. Electrodes were patterned on the photoresist by using the first mask (electrode), gold evaporation and a lift-off process (Appendix A). Following metal lift-off process, the wafer was coated with a sacrificial layer of Polymethylglutarimide photoresist (PMGI SF-11, 1 μm thick, MicroChem) at a spin speed of 4000 RPM for 40 seconds and then hard-baked on a hotplate at 200°C for 5 minutes to remove the solvent. High temperature and long baking time change the property of PMGI SF-11 and make it insensitive to near-UV light and also inert to ethanol. Therefore, NWs suspended in ethanol can be positioned inside wells, which are patterned inside PMGI, without dissolving the photoresist.

To pattern the wells (Figure 2.2(b)) within the PMGI photoresist a layer of 1 μm-thick Shipley 1811 photoresist (MicroChem) was coated on top of the PMGI at a spin speed of 4000 RPM for 40 seconds and baked on a 100°C hot plate for 1 minute. An OAI mask aligner model MBA 800 was used to pattern wells in the second photoresist layer (Shipley 1811) using the well mask. The Shipley layer was exposed for 4 seconds under a near-UV lamp with 19.4 mW/cm^2 power density and was then developed in MF 26-A (MicroChem) for 45 seconds. Exposure and developing time for patterning wells into Shipley 1811 must be long enough to remove all Shipley within the well patterns. Exposing the substrate with deep-UV (Hitachi zone cleaner) for 90 seconds was followed by developing in 101A (MicroChem) developer for 40 seconds. The wells were then transferred into PMGI photoresist using the well pattern on Shipley photoresist as a mask. Deep-UV exposure and developing time must be long enough to remove only half of the PMGI from the well patterns and create half depth wells. 90 seconds of deep-UV exposure and 240 seconds of developing were suitable to create half-depth wells withing PMGI photoresist. The remaining PMGI will prevent electrical short during positioning NWs. It also indicates the gap between suspended end of NWs and substrate in resulting nanoresonators. The Shipley resist was then removed in acetone and left wells with 500 nm depth in the PMGI SF-11 photoresist.

The assembly of NWs was performed at 100 kHz and V = 7 V (rms). A rational method to obtain the values of these parameters is a significant contribution of this dissertation, detailed in Chapter 3. The NW suspension was sonicated for 15 minutes before introduction over the substrate. Sonication disperses NWs in the medium and reduces the number of bundled NWs that are clumped together by van der Waals force. Introducing the NW suspension over the substrate, the electric field gradient in the NW suspension, produced by the applied electric field, orients NWs along the field, attracts them toward regions of high electric field gradient and positions them inside wells (Figure 2.2(b)). The gradient of the electric field is higher at well ends which provide preferential sites for assembly of single NWs compared with the unpatterned regions.

Following NW positioning, the wafer was coated with the second layer of Shipley 1811 photoresist. The “clamp” Mask 3 was used to pattern clamp windows with the same exposure and developing conditions as described earlier for patterning wells in Shipley 1811. These clamp windows act as a mask to transfer patterns to the PMGI photoresist layer after 240 seconds deep-UV exposure in zone oven followed by 45 seconds developing in 101A developer. Removing photoresist left the NW tips and the underlying clamp electrode exposed. At the end of this step, the substrate was diced and clamping operation was performed on each die separately as discussed below.

Silver metal clamps (∼2-3 μm thick) were grown from the clamp electrode by electrodeposition. Versa STAT3 potentiostat was used for electrodeposition of Ag clamp from commercially available silver succinimide ($Ag(C_4H_5NO_2)_2$) solution. The rigidity of the clamp plays a very important role in nanoresonator functionality. Clamp material choice and clamp morphology modification have been discussed extensively in Moghimian’s dissertation [63].

Following NW clamping, the substrate was soaked in Microposit Remover 1165 (MicroChem) at 55°C for 8 hours to dissolve both PMGI and Shipley photoresist. The substrate was transferred to a petri dish filled with DI water. To clean the substrate, it was slightly agitated in water and moved to another petri dish with clean

DI water. This step was repeated four times with DI water and then the substrate was transferred to the next petri dish containing ethanol. The same procedure was followed to clean the substrate in ethanol and at the end, the substrate was dried in a critical point dryer. At the start of critical point drying ethanol is replaced with liquid CO_2. It is possible to choose a particular temperature and corresponding pressure, where liquid CO_2 and its vapor can co-exist and hence have the same density. At this point, liquid CO_2 changes to vapor without change of density and therefore without surface tension effects. This prevented adhesion of the suspended NW ends to the driving electrodes. All steps with required exposure and developing time is summarized in Appendix B to make it easier for reader to follow the sequence of steps.

Removing and cleaning the substrate from the photoresist after clamping NWs is a very important step. Figure 2.4 shows Rh NWs clamped with Ag. If photoresist was not completely removed either due to short soaking time of the substrate in Microposit Remover 1165 or incomplete cleaning step after transferring substrate from Microposit Remover 1165 to DI water and ethanol, remaining photoresist may cover some parts of the substrate including NWs, as shown in Figure 2.4 (a) and disrupt nanoresonator functionality. To prevent this defect (see Figure 2.4 (b)), high temperature (∼55°C) of Microposit Remover 1165, as well as several steps of cleaning with DI water and ethanol, is strongly recommended.

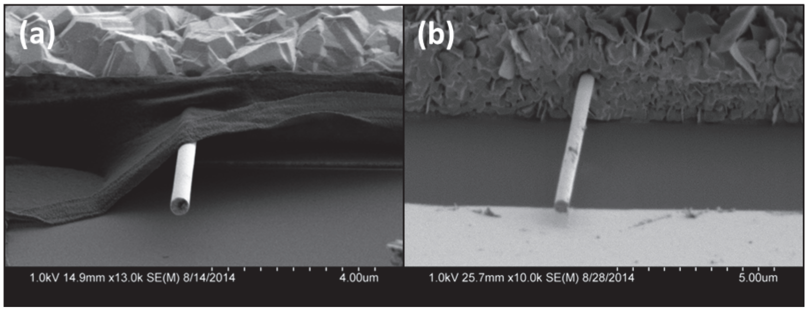

Figure 2.4: Importance of photoresist removal step. (a) Photoresist residual, due to incomplete cleaning step, covers NWs and disrupts the functionality of the NWs. (b) No photoresist residual after soaking substrate in high-temperature Microposit Remover 1165 for 8 hours.

2.2.2 Clamping

As described in Section 2.2.1 and Appendix B, silver was electrodeposited to clamp one end of the NWs after exposing and removing photoresist from clamp electrodes. To achieve this, photoresist needs to be entirely removed from these electrodes. Figure 2.5 shows an example in which photoresist was only partly removed. In this example, the PMGI layer was exposed for 120 seconds with DUV and developed in 101 for 30 seconds. By looking at clamp electrodes across the whole substrate under an optical microscope, it was observed that Ag was only deposited where the wells were patterned in previous steps. The thickness of PMGI photoresist in wells is half of the thickness of the non-patterned photoresist. The thinner layer of photoresist required less exposure and developing time, to be completely removed from the substrate. In the example shown in Figure 2.5, the exposure and developing time was enough to remove photoresist only from patterned wells. The remaining photoresist prevented Ag electrodeposition on the electrode surface. Our experiments showed that increasing the exposure and developing time to 240 and 45 seconds respectively, was sufficient for complete removal of the photoresist.

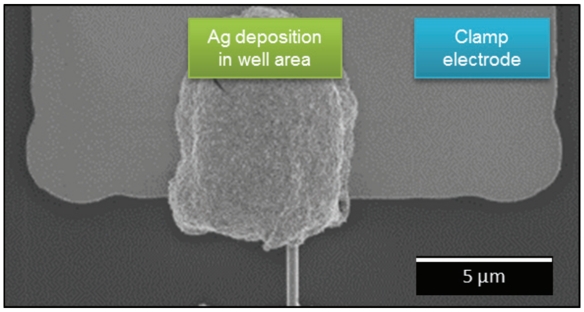

Figure 2.5: Due to insufficient exposure and developing time, the photoresist was partly removed from clamp electrode. Clamp material was only deposited where photoresist was completely removed.

Adhesion of clamp material to clamp electrodes and its morphology directly influence the functionality of the completed device [69] and need to be controlled through electrodeposition conditions, such as current density and ionic concentration. NW clamping and guidelines to overcome possible defects are explained in Moghimian's Ph.D. dissertation [63].

2.3 NW Defects, Pre-clamped and Post-clamped Yield

This section presents the experimental results of NW assembly and clamping. Several defects may occur during positioning (pre-clamped) or after clamping (post-clamped) which will be discussed. These defects disrupt the functionality of the resulting nanoresonator and lower the device yield. Protocols to measure pre- and post-clamped yield are explained in this section.

2.3.1 Defects in NW Positioning

Figure 2.6 shows experimental results for pre-clamped Rh NWs. As shown by white arrows, some wells contain single NWs. Some defects including empty well, misaligned NWs, chained, bundled and short NWs are demonstrated in these micrographs.

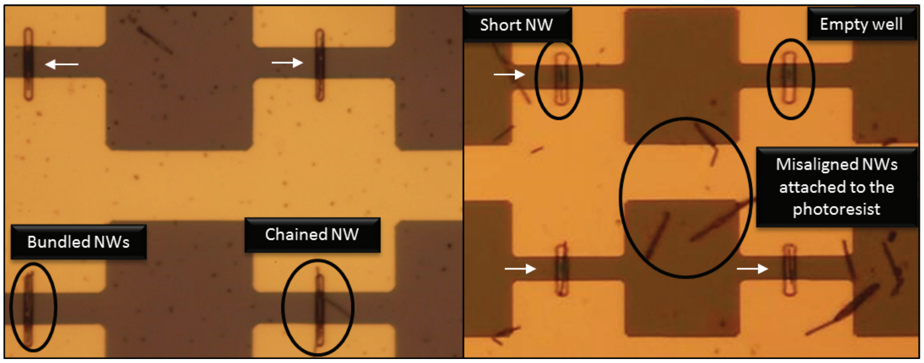

Figure 2.6: Experimental result of pre-clamped NWs. Both images show that NWs were preferentially aligned in the wells, as marked with white arrows. Assembly defects including empty wells, short NWs, misaligned NWs, chained and bundled NWs are marked in these two images.

Using the fabrication process described in Section 2.2 and Appendix B, misaligned NWs were removed with the photoresist. Bundled and chained NWs, shown in Figure 2.7, are common defects that origin from a high concentration of the NWs in the suspension. Using low NW concentration as well as sonication of the NW suspension before assembly, decrease these defects considerably. However, if NW concentration is too low, number of the empty-well defect will increase. Therefore, NW concentration plays an important role in device yield and has to be adjusted before starting the assembly process as described in Chapter 3.

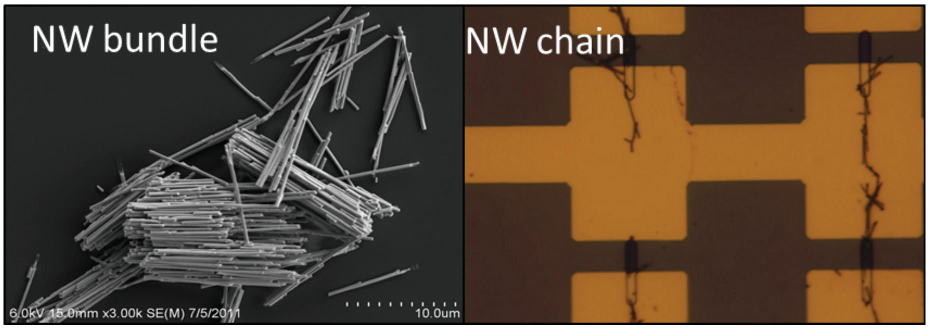

Figure 2.7: NW bundle and chain are the most common defects during NW assembly. High concentration of NWs is the main cause of these defects.

The length of Rh NWs used in this work was measured to be between 8 and 12 μm by using several SEM micrographs, as shown in Appendix C. However, small fragments of NWs were also formed due to NW breakage during several steps of dissolving the template and cleaning the NWs. These short NWs, if positioned inside wells, can decrease the yield of the functional device. Removing these NW fragments is not possible without assistance from sorting techniques. At the time of this work, a NW sorting technique was not available. Therefore, short NWs (although small fraction) could decrease the device yield.

2.3.2 Protocols for Device Yield Measurement

Design #1 was fabricated and used for yield measurement. A 10 μL drop of diluted Rh NWs with the concentration of $19{\times}10^6$ NW/mL was dispersed on a die. NW assembly occurred on each die separately. The concentration of NWs suspension was chosen to be dilute enough to prevent defects such as NW chaining, as shown in Figure 2.7 and described in Section 2.3.1. The yield was determined by observing optical micrographs from 3000 randomly selected electrode pairs out of a total 57000 pairs from six different dies on a substrate. Several rules, explained below, were followed to measure the yield of pre-clamped and post-clamped NWs.

Although chaining was introduced as a defect, if chaining occurred at the NW tip placed on clamp electrode, marked with red arrow in Figure 2.8, this NW was counted as a functional device since the chained end was clamped without disrupting device functionality.

During NW assembly, positioning of multiple NWs between electrodes was observed as shown with white arrows in Figure 2.8. One approach for eliminating multiple NW positioning would be to make the width of clamp window the same size as the width of wells (2 μm). In this case, only NWs positioned in the wells will be clamped and the rest will be removed with photoresist. However, aligning small-sized clamp windows with the wells makes alignment difficult and time-consuming. To prevent this difficulty, in this work, clamp windows are made as wide as clamp electrodes. Multiple NWs positioned between electrodes could be clamped and serve as functional NWs. However, the distance between these adjacent NWs is important. If these NWs are too close, their interaction with each other causes difficulties in signal detection during operation of the nanoresonators. Accordingly, multiple NWs with less than 10 μm gap were not counted as functional nanoresonators (showed as non-functional multiple NWs in Figure 2.9). If they are far enough apart, they all can create functional devices but to simplify measuring the device yield, these multiple functional NWs are counted as one functional device.

Rarely, it was observed that a NW was positioned adjacent to an *empty* well as shown with a green arrow in Figure 2.8. This NW was counted as a functional NW as it can be clamped and utilized for resonance measurement.

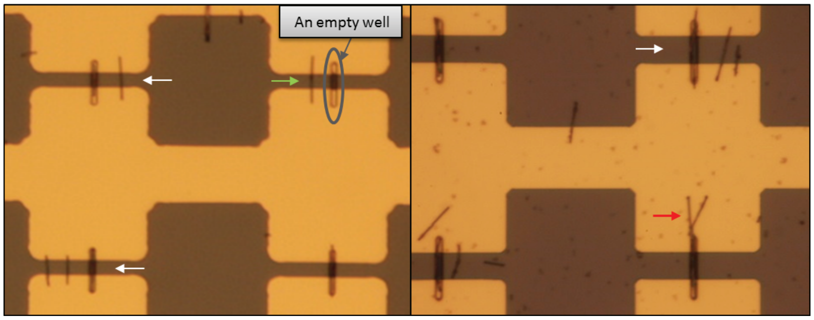

Figure 2.8: NW counting rules to evaluate pre-clamped yield: A NW with its chained end positioned on clamp electrode (red arrow) is considered in pre-clamped yield measurement. Where multiple functional NW are positioned between pairs of electrodes (white arrows), only one NW is counted per each pair. Green arrow shows a NW assembled next to an empty well. This NW can be clamped and create a functional nanoresonator.

Figure 2.9 shows SEM micrographs of clamped NWs with some noted defects. After clamping, all misaligned NWs or short NWs which did not overlap with clamp electrodes were removed with photoresist. Empty sites can occur due to two reasons: (1) if no NW was assembled during NW positioning or (2) if the assembled NW was too short to be clamped. In the former case, the number of empty wells was minimized by finding the best concentration of NWs in suspension as well as improving the assembly conditions, described in Chapter 3. However, in the latter case, only sorting NWs based on their length can eliminate this defect.

As marked in Figure 2.9, a short but clamped NW can be considered as a functional short NW, where the gap between free end of the NW and the driving electrode is less than 1 μm. If this gap is more than 1 μm, resonant measurement of this NW may be difficult, as described in Chapter 4. Accordingly, these very short clamped NWs were not considered as a functional devices.

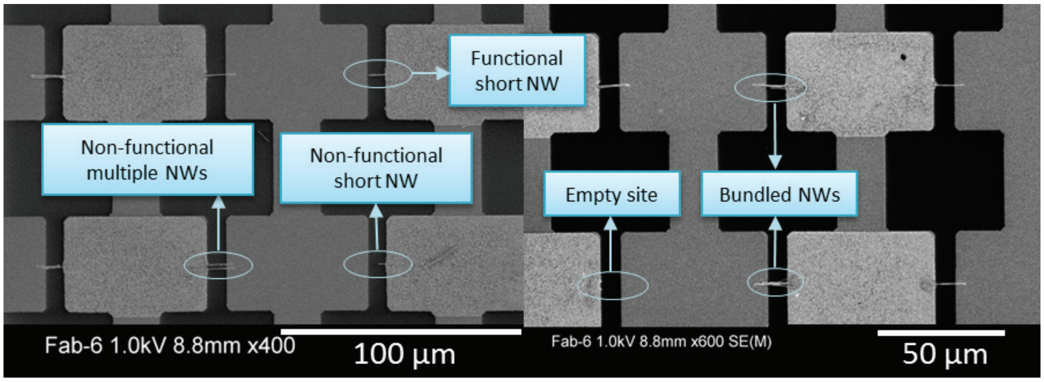

Figure 2.9: NW resonators and the types of defects.

Elimination of defects can enhance the device yield. Understanding the effect of forces and physical parameters that are involved in generating the defects will help us to increase the device yield. What are these forces and parameters and how can we harness their disruptive effects? Researchers have previously used trial-and-error to increase the device yield or sought assistance from other forces like fluid flow drag force [39] or capillary force [40]. The immense experimental effort and time in trial-and-error technique is costly. In case of assistance from other forces, additional fabrication steps are required which lead to higher fabrication cost or more complicated fabrication steps. A simple method is required that can systematically decrease the density of defects by eliminating the forces and parameters that disrupt NW assembly.

In this chapter, we have discussed how DEP force is used for positioning NWs on a pre-patterned substrate. Although several groups have used DEP force for NW assembly [14,25,39–42,70], there are several details in assembly and integration which have not been considered or deeply studied. Some of these overlooked details make a very substantial difference in the yield of positioned NWs and they will be addressed in Chapter 3.

2.4 Conclusions

This chapter discussed bottom-up field-directed assembly of NWs for nanoresonator fabrication. This hybrid technique has resolved some of the issues related to conventional fabrication techniques. The main challenge in fabricating nanoresonators is covering large surface area with individually addressable devices at low fabrication cost. Bottom-up field-directed assembly is a cost-effective technique that enables assembly of off-chip synthesized NWs, which can then be integrated at pre-determined places and addresses individually.

Some defects can occur during NW assembly and decrease the yield of resulting nanoresonators. The main defects such as NW chaining and bundled NWs, empty sites, misaligned and short NWs were shown. In addition, some approaches to eliminate these effects were noted, such as controlling NW concentration or decreasing the size of clamp windows, with the goal of increasing the device yield. At the end of this chapter, rules that have been followed in order to measure the device yield were defined.

Several interesting questions remain, for instance: how do parameters related to the applied field, such as voltage and frequency, affect the yield of NW assembly? What are the effects of other forces such as Brownian motion and capillary force during NW assembly? To answer these questions, we need to study all forces and parameters that can affect NW assembly. In order to increase the device yield, a framework is needed to systematically minimize the effect of disruptor forces and parameters. This framework and results of using it are explained in details in Chapter 3.

2.5 Future Work

Throughout this chapter, assembly of NW resonators was described and several approaches toward increasing the device yield were discussed. NW length variation in a NW suspension is introduced as a disruptor that decreases the number of functional nanoresonator when short NWs were positioned inside wells. A nondestructive technique which enables sorting NWs based on their size can prevent positioning non-functional short NWs and as a result, increase the device yield.

NWs that are less than 10 μm apart and clamped one electrode pair, are not functional. As mentioned, having a clamp window, as wide as the width of wells, can be helpful to clamp only the positioned NW inside the well while the NWs positioned outside the wells will be removed with photoresist. But it was also noted that this method makes aligning clamp mask with patterned wells difficult and time-consuming. One approach to clamp only the positioned NW inside well is through tuning the exposure and developing time during opening the clamp window. It was demonstrated in Figure 2.5 and explained that since photoresist inside wells has less thickness compared with the non-patterned region of photoresist, the photoresist inside wells will be developed and removed in shorter exposure and developing time. Therefore, clamp material will be only deposited on these areas and will only clamp NWs that were positioned inside wells. Since at the time of doing these experiments photolithography facilities were not available at UVic, trying this approach required many trips to Simon Fraser University, where we had access to cleanroom and photolithography tools. Costly trips and user charges, and many other practical limitations slowed down the development and prohibited the author for trying this approach. However, an equipped photolithography facility is expected to become available at UVic in a time scale of one year. This will greatly speed up fabrication of substrates.

Chapter 3

A Framework for Field-Directed Assembly of Single Nanowire

This chapter presents an article published [71] with the title of *Field-directed assembly of nanowire: identifying directors, disruptors and indices to maximize device yield*. The article (Nanoscale 8 (2016): 889-900) is reproduced with permission from Royal Society of Chemistry.

Abstract

Individually-addressable nanomechanical (NEMS) devices have been used to demonstrate sensitive mass detection to single-proton level, as well as neutral-particle mass spectrometry. The cost of individually securing or patterning such devices is proportional to their number or the chip area covered. This limits statistical support for research results, as well as paths to the commercial availability of extraordinarily sensitive instruments. Field-directed assembly of synthesized nanowires addresses this problem and shows potential for low-cost, large-area coverage with NEMS devices. For positive dielectrophoresis (pDEP) as the main assembly director, the space of field, geometric and material parameters is large, with combinations that can serve either as directors or disruptors for directed assembly. We seek parameter values to obtain the best yield, by introducing a rational framework to reduce trial-and-error. We show that sorting the disruptors by severity and eliminating those weakly coupled to the director, allows a reduction of parameter space. The remaining disruptors can then be represented compactly by dimensionless parameters. In the example

protocol chosen, a single dimensionless parameter, the yield index, allows minimization of disruptors by the choice of frequency. Following this, the voltage may be selected to maximize yield. Using this framework, we obtained 94% pre-clamped and 88% post-clamped yield at 57000 nanowire sites. Organizing the parameter space using a director-disruptor framework, with economy introduced by non-dimensional parameters, provides a path to controllably decrease the effort and cost of manufacturing nanoscale devices. This should help in the commercialization of individually addressable nanodevices.

3.1 Introduction

Remarkable capabilities of single-proton mass detection [19], neutral particle mass spectrometry [72] and earlier, the detection of nucleic acid sequences [73] have been demonstrated using individually addressable nanomechanical (NEMS) devices, but only for a small number of clamped nanowires (NWs) or nanobeams. Large-area coverage with individually-addressable NW devices will significantly reduce experimental research time for future landmark demonstrations. If done at low cost, it will also enable stronger statistical support for measurements needed to understand mechanical [20–23] and electrical [20, 24, 25] behavior of NWs, and most significantly, ease the development of instruments for commercial applications, such as screening for early detection of disease through molecular diagnosis [3]. A recent review [74] provides several examples of promising NW device applications.

Directed assembly provides a path towards nanomanufacturing systems to achieve large-area coverage at low-cost. For nanofabrication, the term directed assembly describes a family of methods [14, 39, 41, 75, 76] which use micro-patterned structures for spatial and temporal control of fields, to direct synthesized nanoscale elements to predetermined locations. The patterned structures enable NW position control and could involve one of several *fields* -such as hydrodynamic, electric, magnetic, temperature -or their combinations. Such field-directed assembly combines elements of top-down microfabrication and bottom-up nanostructure synthesis, enabling fabrication of nanoscale devices in large arrays. It retains the advantages of using low-cost nanostructure assembly (compared to electron-beam lithographic patterning) offered by self-assembly [76, 77], but also provides greatly improved position control, and a route to individual device addressability.

In contrast with established macroscale manufacturing processes, research laboratory nanofabrication protocols, including field-directed assembly, often require some small modifications to be reproducible by a new user or in a new facility. These changes are no assault on experimental repeatability, but are a mundane consequence of unknown methods or prohibitive cost of adequate metrology at and below device scales. In addition, there is an imperfect understanding of possible coupling between several physical effects. As a result, a user who decides to change a single step, material or experimental parameter value within a protocol may often have to change several others. In the absence of a framework to guide the choice of experimental parameter values, considerable effort is spent in a trial-and-error approach to obtain best yield from NW assembly. To strongly reduce such effort, we propose a framework, based on identifying forces, which serve either as *directors* or *disruptors*, with competing effects on yield in directed assembly. The framework provides a rational guide to parameter value selection.

Dielectrophoresis (DEP) force has been reported by a few research laboratories [14, 25, 39–42, 75, 78, 79] worldwide, as a director in field-directed NW assembly. Examples of directors and disruptors are forces that arise from negative or positive DEP [79], Brownian motion [68,80], electroosmotic forces [41,42] or electrode polarization effects [41,78]. Here we use a sequence of steps from a known DEP protocol, reported in the work of Li *et al.* [14], to help illustrate the utility of the framework. Starting with an established basis is also necessary to examine whether any improvements in yield accrue from use of the framework.

While parameter values are chosen using the framework developed later in this paper, here we briefly outline the basic steps utilized, as shown in Fig. 3.1(a) to (d). We used rhodium (Rh) NWs that have desirable mechanical properties for resonant mass sensing as they retain high quality factor (Q-factor) from high vacuum to near atmospheric pressure [14]. Photolithography was first used to create electrically conductive pad pairs with different gap widths of 6, 8 and 10 μm, which define the locations to which NWs will be directed. A photoresist layer was spun to cover the electrodes and prevent an electrical short circuit that would result from NWs bridging electrode pads. Wells (shown in Fig. 3.1(a)) were then patterned in photoresist between each electrode pair, followed by application of the electric field to direct NWs into wells (Fig. 3.1(b)). Photoresist was removed from one of the electrode pairs and clamp material was electrodeposited to fix one end of the NWs (Fig. 3.1(c)). Finally, NWs were suspended by removing the remaining photoresist from the substrate and using critical point drying. Experimental details may be found in Section 4 at the

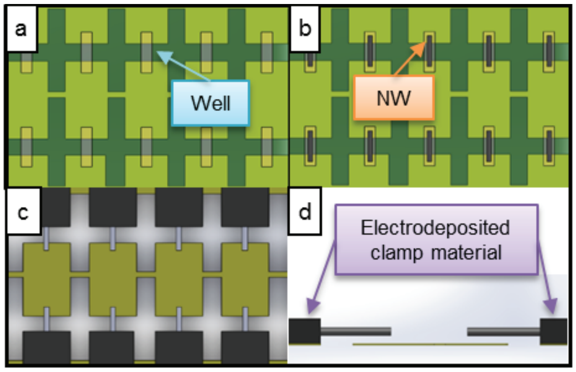

Figure 3.1: Schematics of positioning and clamping of single NWs on gold electrodes: (a) patterning electrode pairs with wells in between, to locate and trap NWs (b) positioning single NWs inside wells using DEP (c) electrodeposition of clamp material after photoresist removal from electrode surface (d) side view of clamped NWs after removing the remaining photoresist.

end of this paper.

The word ”yield” in the literature on directed assembly has been used to refer to different things. Most devices made from suspended NWs need one or both ends to be clamped after the directed assembly process is complete. Though clamping processes typically do reduce the yield, the word ”yield” has been used to report the yield from assembly alone [39,40], while other reports [14] use the word to mean yield of functional devices after both assembly and clamping. It is misleading to compare numbers for the yield between these two groups of references. To avoid confusion, we suggest the use of two categories of NW yield: pre-clamped yield, which is the percent of available sites with correctly positioned single NWs; and post-clamped yield, referring to the percent of sites with functional, clamped NWs.

3.2 Framework Development

This study is focused on developing a framework for field-directed assembly of NWs. A DEP protocol with positive dielectrophoresis (pDEP) as the main director is used here to show the framework methodology in classifying and evaluating the director and disruptors. We separate disruptors into two groups: {1} disruptors weakly coupled to the main director, pDEP, that either depend on electrode design or need less quantification to be eliminated and {2} disruptors that are strongly coupled through parameter choice to the main director. In this section, we first evaluate weakly-coupled disruptors (disruptive torque, capillary force from the drying front, improper NW concentration, Brownian motion and electrothermal force) followed by strongly-coupled ones (negative DEP (nDEP), electroosmotic force and electrode polarization). In this evaluation, the results of analysis and computation can provide useful guidance, even if somewhat rough. This step is followed by the definition of a dimensionless parameter, which compactly represents the competition between the director and the remaining disruptors. This helps to guide parameter value selection for best device yield, with reduced trial-and-error. In the example chosen in this study, the final control of device yield was realized only by tuning the director, with negligible hindrance from disruptors.

3.2.1 Weakly-Coupled Disruptors

3.2.1.1 Disruptive Torque

DEP torque, a primary need for NW alignment, can become a disruptor when NWs are much longer than the width of the gap between electrodes, in each electrode pair. For low values of the ratio (λ) of electrode gap width to NW length, the induced dipoles can lie beyond the two electrode edges, rather than in between them, with a torque that rotates NWs in an opposite sense to that required for alignment (disruptive or "negative" torque). Some guidance is provided by the computational results of Liu *et al.* [68], which show that it is possible to avoid disruptive torque if $\lambda >0.4$, that is, when NW length is smaller than 2.5 times the gap width.

NWs of length smaller than the gap width ($\lambda >1$) clearly cannot have both ends clamped, and may produce one-end clamped devices which are outside of the intended functional range, even if they are properly aligned. To avoid this, we restrict our choices to the range ($0.4< \lambda <1$).

3.2.1.2 Capillary Force

The spreading of a drop of NW suspension during assembly carries NWs beyond the target assembly region and often leads to undesirable spillover on adjacent dies. Vigorous NW motion was observed during such drop spreading, acting as a disruptor. A further disruptive role of capillary force was seen at drying fronts, that pull away NWs which are partially protruding from wells.

To reduce these disruptive effects, we introduced a cylindrical dam (Fig. 3.2) with

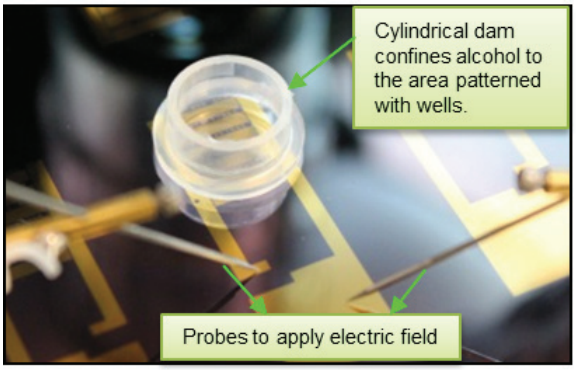

Figure 3.2: A cylindrical dam reduces the effects of drying-front capillary force as a disruptor and prevents NW spillover to adjacent dies.

1 cm diameter and 0.5 cm height, which confined NW suspension to the area of one die with 9500 wells. This eliminates the spreading and flow disruption and leaves a sufficient excess time for DEP to secure both NW ends within wells.

3.2.1.3 Inappropriate Nanowire Concentration

Having too low a concentration will lead to unfilled sites. For any selected suspension volume, a concentration allowing at least one NW for each well (equivalent to 9.5×10^5 NW/mL) is clearly needed to avoid empty sites. However, too high a NW concentration can lead to the formation of chains, bundles, or multiple NWs assembled between electrode pairs, disrupting single-NW assembly and reducing yield. Using the procedure in Methods Section 4, we determined by experiment that a concentration of 19×10^5 NW/mL (2 NWs for each well) was suitable, and repeatedly allowed us to avoid problems associated with too high a concentration of NWs. Images of NW assembly with different NW concentration are provided in Figure D.1 in Appendix D.

3.2.1.4 Brownian Motion

In our experiments, random displacement of NWs due to Brownian motion was observed when no electric field was applied. However, when the electric field was applied, we observed NW trapping within wells begin in about a second after the NW suspension was introduced.

Inspite of our observation for this assembly process, we ask how significant a disruptor Brownian motion could be, and in what circumstances. Cumulative Brownian displacement could be disruptive if it is comparable to, or greater than the displacement due to the DEP force. It is less likely to be disruptive very close to the electrode edges, where the field gradient and DEP force are strongest, but has scope to disrupt motion along the capture path at large distances from the electrode. The ratio of the root-mean-squared (rms) NW displacement induced by Brownian motion to DEP displacement has been estimated earlier [68, 80] for spherical particles. We obtain results for cylindrical NWs, moving perpendicular to the NW axis, in low Reynolds number flow. For this case, the drag coefficient is given by [81]

$$\gamma = F_d/u = 4\pi\eta L/[ln(2L/d) + 0.5] \tag{3.1}$$

Here L, d are the NW length and diameter respectively, the drag force is F_d, u is the velocity of the NW relative to the fluid and η is the dynamic viscosity of the fluid. With L=10μm, d=0.25μm and η=1.2×10^{-3} Pa.s for ethanol, the drag coefficent value is 3.09×10^{-8} kg/s. The reader is referred to the steps in the Appendix of this manuscript (D.1), for derivation of the ratio of Brownian to DEP displacement, in elapsed time t, which yields,

$$\Delta X_{Br}/\Delta X_{DEP} = \sqrt{(2k_BT)/(u^2\gamma t)} = \sqrt{(2k_BT\gamma)/(F^2t)} \tag{3.2}$$

Here F is the DEP force, k_B is Boltzmann's constant and absolute temperature T=293K. The ratio is inversely proportional to NW velocity, and decreases with elapsed time as $t^{-1/2}$. There is no known way of measuring forces, or velocities normal to the observation plane, for individual NWs during this assembly process, and we expect both will depend on NW height above electrodes. However, we may use Eq. (3.2) to examine the role of Brownian motion from an order of magnitude estimate. Fluid depth in the dam is ∼100 μm. An assembly time ∼1 s, for a distant NW in the vicinity of the fluid-air interface, yields an estimate for maximum NW velocity of ∼100 μm/s, for which the value of $\Delta X_{Br}/\Delta X_{DEP}$ is calculated to be 0.005. For a more reasonable starting NW distance of ∼10 μm, the velocity would be ∼10 μm/s, and this ratio would be 0.05. NWs at starting distances ∼1 μm or lower would be in the highest field gradient region and close to capture within the wells. In accord with our experimental observations, this rough estimation process confirms that Brownian motion is not a significant disruptor.

However, the value of this rough scaling analysis is that it shows Brownian motion could be a significant disruptor for slow-moving NWs, low DEP force and for liquids at low temperatures or with high viscosity.

3.2.1.5 Electrothermal Force

Electrothermal force is another disruptor for DEP-assisted positioning of NWs. The current due to applied electric field causes local heat generation in the solution. The resulting temperature variation, if significant, would lead to conductivity and permittivity gradients in the fluid. Therefore, the force imposed on the medium by electric field can vary in different parts of the fluid and induce fluid flow, named electrothermal flow, which interacts with NW positioning. The fluid temperature change is given by [68, 80]:

$$\Delta T \approx \frac{\sigma_m V_{rms}^2}{2K} \tag{3.3}$$

where K and σ_m are thermal and electrical conductivity of the fluid medium respectively (K =0.171 W.m^{-1}.K^{-1}and σ_m is 2.19×10^{-5} Sm^{-1} for ethanol [82]). The maximum applied voltage in this work, V_{rms} =7 V yields a temperature rise of about 10^{-3} °C. For this small temperature change, the effect on permittivity and conductivity is negligible and electrothermal fluid flow is not considered as a disruptor in this work.

In this section, we have used results of analysis and computation as a rough guide to (a) find which potential disruptors are negligible (here, Brownian motion and electrothermal force) and (b) impose constraints on physical parameters (such as ratio of electrode gap width to NW length) to make disruptors negligible. We also used experiments to eliminate some potential disruptors (capillary force and inappropriate NW concentration). Enforcing these constraints reduces the dimension of parameter space. If there is a resurgence of disruptors when modifications are made to established parameter values for a given protocol, these constraints provide a path for correction. This greatly reduces time spent compared to a trial-and-error approach with little intuition.

3.2.2 Strongly-Coupled Disruptors

3.2.2.1 Negative DEP

The time averaged DEP force is given by [36, 79]:

$$F_{DEP} = \frac{\pi r^2 l}{6} \epsilon_m Re[F_{CM}]. \bigtriangledown (E_l^2) \tag{3.4}$$

with

$$F_{CM} = \frac{\epsilon_p^* - \epsilon_m^*}{\epsilon_m^*} \tag{3.5}$$

where l and r are the length and radius of a NW, ϵ_m is permittivity of the medium and E_l is the electric field. Re$[F_{CM}]$, the real part of the Clausius-Mossotti factor, is positive over a range of frequencies for conductive NWs suspended in alcohol and becomes negative at sufficiently high frequencies [36, 42].

ϵ_p^* and ϵ_m^* are the complex permittivity of NWs and medium respectively, defined as $\epsilon^* = \epsilon - j(\frac{\sigma}{\omega})$ where ω is the angular frequency of the applied electric field. The sign of Re$[F_{CM}]$ dictates the sign of F_{DEP}. NWs can be attracted to or repelled from the wells when F_{DEP} is positive or negative, respectively. Here, we eliminate nDEP simply by choosing frequencies below 10^{10} Hz (Fig. 3.3(a)), ensuring DEP remains solely a director. Later in this paper, we will see that other constraints on frequency compel us to use frequencies well below 10^{10} Hz.

3.2.2.2 Electroosmotic Velocity

Among electrohydrodynamic (EHD) effects, a strong potential disruptor in this work is electroosmotic flow, which can interfere with NW positioning by creating a vortical flow, as shown in Fig. 3.3(b). This flow is driven by the electroosmotic force $F = qE_t$, where E_t is the tangential component of the electric field and q is the surface charge density of the electrical double layer. Green *et al.* [83] and Castellanos *et al.* [80] showed that electroosmotic fluid velocity strongly depends on the applied frequency. In addition, Eq. (3.5), plotted in Fig. 3.3(b), shows that Re $[F_{CM}]$ and as a result F_{DEP}, also depend on frequency. We show below, that a careful choice of frequency can be used to overcome the disruptive effect of electroosmotic flow.

The electroosmotic velocity, ν, can be calculated using [83]

$$\nu = \frac{\epsilon_m V_{rms}^2}{4x\eta} \times \frac{\Omega^2}{(1+\Omega^2)^2} = \frac{\epsilon_m V_{rms}^2}{4x\eta} f(\Omega) \tag{3.6}$$

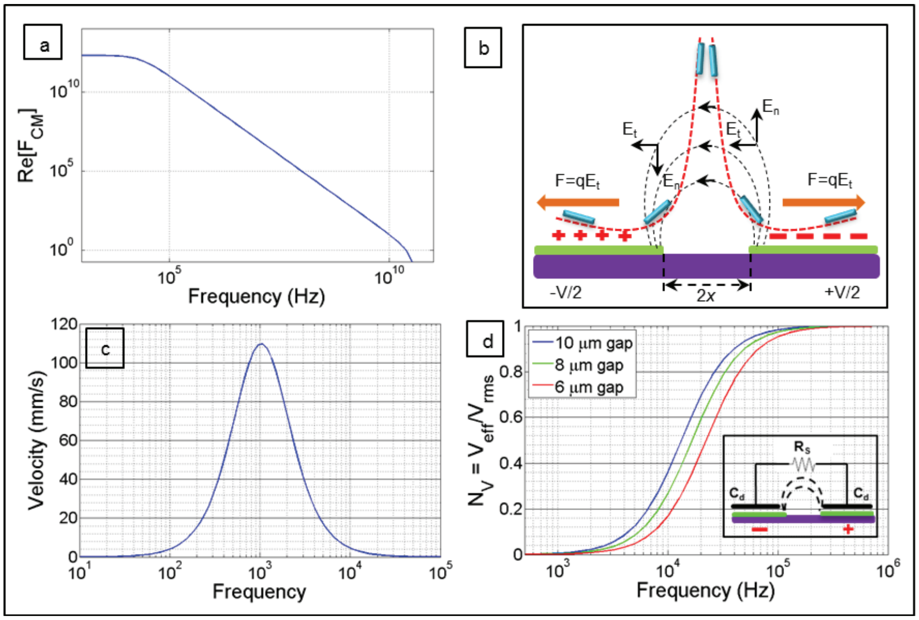

Figure 3.3: Frequency changes affect the competing director and disruptor forces by altering (a) the magnitude of the DEP director as a result of the change in the magnitude of $Re[F_{CM}]$; (b) the electroosmotic force (F), a disruptor that drags NWs away from the assembly-electrode gap and (c) the electroosmotic velocity of disruptor fluid vortices. (d) The ratio of the effective voltage to the applied voltage for different gap sizes changes with frequency due to electrode polarization (a disruptor), modeled as an RC circuit(inset).

knowing the rms-value of applied voltage (V_{rms}), dynamic viscosity of the electrolyte (η) and characteristic length x (half the gap width between electrodes), and with Ω, the dimensionless frequency, defined as:

$$\Omega = \frac{\pi}{2} x \kappa \omega (\frac{\epsilon_m}{\sigma_m}) \tag{3.7}$$

where κ is the reciprocal Debye length of the double layer. For liquids with a low dielectric constant, such as ethanol, κ^{-1} is $\sim$0.5 μm [84]. Electroosmotic velocity is plotted in Fig. 3.3(c) for ethanol with ε_m=2.3 $\times$ 10^{-10} F.m^{-1} and $\sigma_m = 2.19 \times 10^{-5}$ Sm^{-1}, at V_{rms}=7 V and characteristic length of x =5 μm. It shows a frequency peak at $\sim 10^3$ Hz, which is termed the EO-characteristic frequency. At low frequencies, here below $\sim 10^2$ Hz, the voltage drop across the double layer is high, making E_t small, with the resulting electroosmotic force $F = qE_t$ being too small to create electroosmotic flow. At high frequencies, here above $\sim 4 \times 10^4$ Hz, we do not see electroosmotic flow, but for a different reason. At this high frequency the double layer does not have sufficient time to form [80, 83], and the electroosmotic force is small because q is small. The calculation above provides guidance for selecting frequency to minimize electroosmotic flow. In addition, to enable use of a normalized electrosomotic velocity, (ν/ν_{max}), as a dimensionless measure of the strength of this disruptor, Eq. (3.7) shows that the maximum value of $f(\Omega)$ occurs at Ω=1, yielding $\nu_{max} = (\epsilon_m V_{rms}^2)/(16x\eta)$. This parameter, ν_{max}, will be used in Sec 3.2.4

3.2.2.3 Electrode Polarization

The presence of an electrical double layer gives rise to another disruptor, electrode polarization. Electrode polarization causes a voltage drop adjacent to the electrode, and as a result, the effective voltage (V_{eff}) that provides the field strength for NW positioning, becomes less than the applied voltage (V_{rms}). The electrical conduction path, shown in Figure 3.3(d) (inset) consists of electrolyte resistance R_s for conduction through the suspending medium with two capacitive impedances (C_{eq}) in series, associated with the electrical double layers and photoresist at each of the two electrodes. The total impedance Z_T is defined [85, 86] by:

$$Z_T = R_s[1 + \frac{2}{j\omega C_{eq} R_s}] \tag{3.8}$$

Here $C_{eq} = [C_d C_{PR}/(C_d + C_{PR})]$, where C_d and C_{PR} are the capacitance of the electrical double layer and photoresist layer over the electrode, respectively. For electrodes of surface area S, with photoresist thickness of t and κ^{-1} as a measure of double-layer thickness, $C_d = \varepsilon\kappa S$ and $C_{PR} = \varepsilon t^{-1} S$. R_s is calculated approximating the conduction path as having length equal to gap size ($2x$) and a cross-section defined by electrode width and a measure of the double-layer thickness, κ^{-1}.

The ratio (V_{eff}/V_{rms}), the normalized effective voltage for DEP, may be defined, as seen in the inset of Fig. 3.3(d), by:

$$N_V = \frac{V_{eff}}{V_{rms}} = \left| \frac{1}{1 + \frac{2}{j\omega R_s C_{eq}}} \right| = \frac{1}{\sqrt{1 + (\frac{2}{\omega R_s C_{eq}})^2}} \tag{3.9}$$

The minimum normalized effective voltage for DEP (N_V=0) occurs when the electrode polarization disruptor effect is maximum and vice versa. Therefore, normalized electrode polarization is defined as:

$$N_{EP} = 1 - N_V \tag{3.10}$$

Figure 3.3(d) shows that at frequencies less than 10^5 Hz only a fraction of applied voltage is available for NW positioning and below 10^3 Hz, N_V goes to zero as the value of N_{EP} approaches 1. As seen from a curve for any single value of gap size in Figure 3.3(d), we may maximize the fraction of applied voltage available for DEP to N_V=1 by increasing the frequency. Our choice of electrode gap size is determined by NW length and the constraint to avoid disruptive torque. How does this choice affect the strength of electrode polarization as a disruptor?

The effect of varying electrode gap size is seen in the curves in Figure 3.3(d), which shows that electrode polarization vanishes at higher frequencies for smaller electrode gap size ($2x$). This effect can be explained by the effect of relaxation times defined by Bazant *et al.* [87] as $\tau_c = 2x\kappa^{-1}/D$ where D is the ion diffusivity. Larger gap widths ($2x$) require longer charging time τ_c, and a lower frequency must be used to achieve the same double-layer thickness. As seen in Figure 3.3(d), if the same frequency is used for larger gaps, the effective voltage available for the DEP field is increased, reflecting the reduced double-layer thickness.

3.2.3 Experimental observation: effect of strongly-coupled disruptors on assembly yield

In the last section, we have shown that frequencies higher than 10^5 Hz would be required to eliminate both electroosmotic flow and electrode polarization disruptors. To experimentally see the effect of these disruptors on yield, pre-clamped yield was measured at two frequencies: {1} 10^4 Hz, at which theoretical results in Figure 3.3(d) show that only ~18, 24 and 38% of applied voltage is effective for NW assembly for gap sizes of 6, 8 and 10 μm respectively ,and {2} 10^5 Hz, where V_{eff} is almost equal to V_{rms}. If the theoretical results in Figure 3.3 (c) and (d) are accurate, pre-clamped assembly yield should show a significant increase at 10^5 Hz, compared to 10^4 Hz.

{1} After eliminating weakly-coupled disruptors by following the guidelines provided in Section 3.2.1, NW assembly between electrodes with gap sizes, $2x$, equal to 6, 8 and 10 μm, was observed at 10^4 Hz. Almost no assembly occurred at voltages less than 7 V (rms) at this frequency. Increasing applied voltage to the maximum value available to us, 7 V (rms), 15 to 20% of wells filled with NWs. For each gap size, V_{eff} /V_{rms} at 10^4 Hz (based on Figure 3(d)) and experimental yield of pre-clamped NWs are shown in Table 3.1.

{2} The yield was then studied for a range of voltages between 0.7 to 7 V (rms) at

Table 3.1: Pre-clamped experimental yield (Exp. yield) at 10^4 Hz and 7 V (rms). Theoretical V_{eff}/V_{rms} was calculated using Figure 3.3(d).

Gap size (μm)	V_{eff}/V_{rms}	Exp. yield (%)
10	0.38	20
8	0.24	18
6	0.18	15

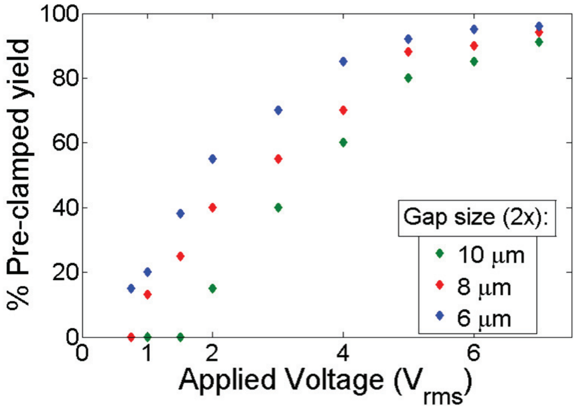

Figure 3.4: Experimental results showing the effect of applied voltage on pre-clamped yield at 10^5 Hz for three different gap sizes ($2x$). Larger gap sizes have higher threshold voltage (2, 1 and less than 0.7 V (rms) respectively for $2x$=10, 8 and 6 μm. Highest assembly yield occurs at 7 V (rms).

10^5 Hz as shown in Figure 3.4. For each gap size, there is a threshold voltage below which NW assembly does not occur due to the small value of F_{DEP}. As seen in Figure 3.4, NW assembly does not occur at voltages below 2, 1 and 0.7 V (rms) for 10, 8 and 6 μm gap sizes respectively. Increasing the applied voltage and resulting F_{DEP} increases the assembly yield. The maximum yield realizable, occurs at the highest available voltage of 7 V (rms) at 10^5 Hz. For this condition, we used two dies of 9500 sites, for each gap size. The measured pre-clamped yield varied with gap size. Several optical micrographs such as in Figure 3.5, were used to determine the yield. The yields were 91% and 93 % for 10 μm gap, 94% and 95 % for 8 μm and 94% and

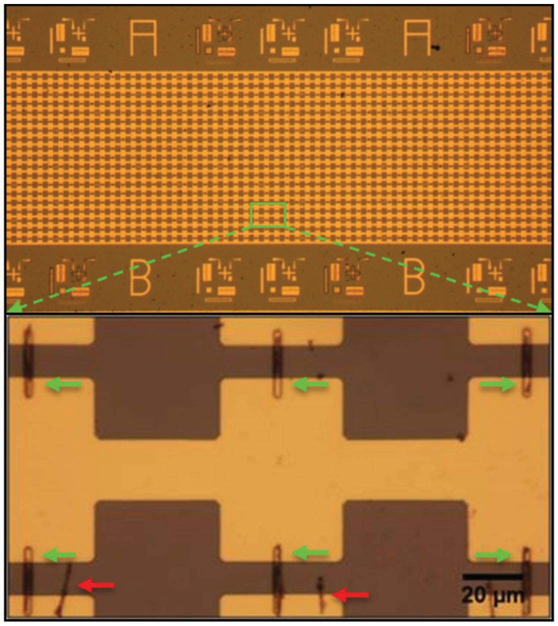

Figure 3.5: Single NWs aligned in almost every well (green arrows) at 10^5 Hz and 7 V (rms). Red arrows show misaligned NWs.

96 % for 6 μm gap size, resulting an averaged pre-clamped yield of 94%.

3.2.4 Director-Disruptor Competition

To separate the director-dominant region from the disruptor-dominant one, shown in Figure 3.6(a) and (b), we introduce a cut-off frequency, at which both the strong disruptors, normalized electroosmotic velocity (N_{EO}) and normalized electrode polarization ($N_{EP} = 1 - N_V$) are each less than 5%. Normalized electroosmotic velocity N_{EO} is defined as:

$$N_{EO} = \frac{\nu}{\nu_{max}} = \frac{4\Omega^2}{(1+\Omega^2)^2} \tag{3.11}$$

where ν_{max} defined earlier, is the maximum electroosmotic velocity at EO-characteristic frequency. N_{EO} provides a non-dimensional measure of the strength of the disruptor.

Regions with frequencies greater than cut-off frequency are director-dominant regions. If the DEP force alone has magnitude sufficient to direct NWs, it will face negligible competition from disruptors in this region. Figure 3.6(b) shows that when ethanol is used as the medium, a large disruptor-free frequency range is available, beginning at $\sim 10^5$ Hz and extending to $\sim 10^{10}$ Hz, the frequency for cross-over into the nDEP region.

The region with frequencies less than EO-characteristic frequency is disruptor-

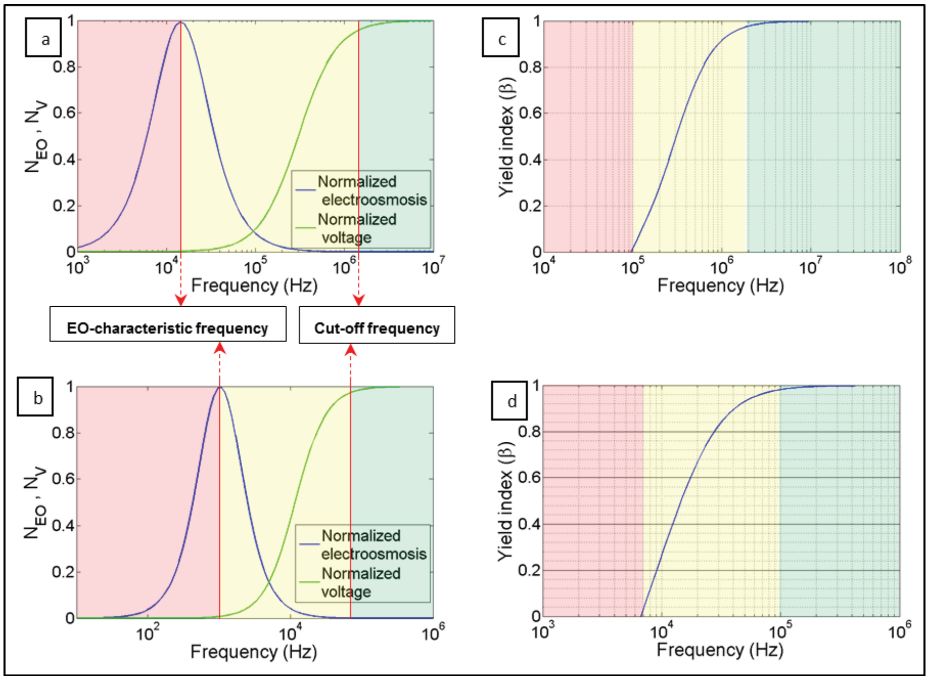

Figure 3.6: Director-dominant (green), disruptor-dominant (pink) and competing region (yellow) for water (a) and ethanol (b) with electrical conductivity of 5×10^{-3} and 2.19×10^{-5} Sm^{-1} respectively. The yield index for water (c) and ethanol (d) indicates the device yield as a result of competition between disruptors and directors in the competing region. For this comparison, electrode gap size was 10 μm and 1μm photoresist layer was considered on the electrodes.

dominant, in which high electrode polarization and electroosmotic fluid flow overcome the directive effect of DEP force and decrease the yield dramatically. At frequencies between cut-off and EO-characteristic frequencies, as seen in the central region of Figure 3.6(a) and (b), directors and disruptors are competing. The cut-off and EO-characteristic frequencies vary as the medium changes since both N_{EO} and N_V depend on the electrical properties of the medium. To investigate the effect of suspension medium property we chose water and ethanol and plotted N_{EO} and N_V vs frequency. Figure 3.6(a) and (b) shows the three regions for water and ethanol respectively. The higher cut-off and EO-characteristic frequency for water compared with ethanol is due to the higher conductivity of water.

The competing region is an important region to study as the competition between forces can decrease or increase the device yield. How can the effect of competition between the director and the dominant remaining disruptors on device yield be approached quantitatively? As we have earlier (in Section 3.2.1) removed weakly-coupled disruptors, we now define a parameter, the yield index β, such that β=1 if there is no reduction of DEP by disruptors and β=0, if the disruptors are at their maximum value. β is defined as:

$$\beta = 1 - N_{EP} - N_{EO} \tag{3.12}$$

Using Eq. (3.10), this can be rewritten as:

$$\beta = N_V - N_{EO} \tag{3.13}$$

Figure 3.6(c) and (d) shows how the region of competition and the resulting yield index change with respect to frequency in water and ethanol respectively. For our selected parameter values, it shows that the yield index is maximum at frequencies higher than 2×10^6 Hz for water and 10^5 Hz for ethanol.

Figure 3.6 enabled comparison of yield indices and operating parameters for suspension fluids -water and ethanol- with different properties. In this work, a layer of photoresist was coated on the electrodes (see Section 3.4.3). To calculate the yield index, the capacitance of the photoresist has to be included while calculating C_{eq} in Eq. (3.8). The resulting yield index, plotted in Figure 3.6(d), shows that the yield index increases slightly from 0.98 to 0.99, in moving from 10^5 to 2×10^5 Hz. However this change would cause the term $\mathrm{Re}[F_{CM}]$ in the DEP force to decrease in value by nearly an order of magnitude from 6×10^{11} to 9×10^{10} (from the data used to create Figure 3.3(b)). In this case, to prevent large DEP force reduction, we select 10^5 Hz and forgo the small increase in yield index available at 2×10^5 Hz.

3.2.5 Clamping

Field-directed assembly typically requires clamping of the NWs, to secure them in place for a circuit or network (integration), or to build individually addressable NW devices. These may require, at one or both ends of a NW, electrical contact or a firm pedestal for nanomechanical applications of NWs. Here we briefly discuss clamping and post-clamped device yield. Methods such as electron beam induced deposition (EBID) [78] incur a cost proportional to the number of clamped devices; their cost becomes prohibitive for large arrays. Simultaneous electrodeposition of all required clamps on a chip, using the metal electrodes designed for DEP, circumvents this cost penalty. Electrodeposition of gold from cyanide-based solutions has been

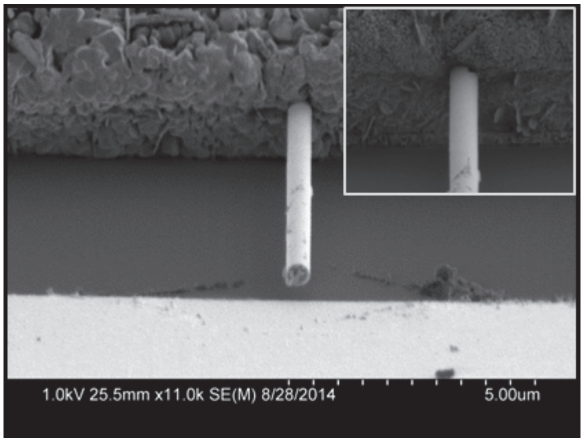

Figure 3.7: Single-end-clamped nanoresonator using electrodeposited silver as clamp material, with inset showing the uniformity of the silver clamp around the NW.

demonstrated in previous work with metal NWs [21] and with silicon NWs [14], to enable clamps of repeatable rigidity. Here, the use of silver (Ag) in place of gold enables a reduction in step cost (current cost ratio 1:65 for Ag:Au) and removes the dependence on toxic gold cyanide solutions. Figure 3.7 shows a clamp fabricated to create a cantilevered NW with (inset showing) uniform interfacial contact of Ag.

Figure 3.8 is selected to illustrate examples of defects -empty sites, NWs broken or misaligned during clamping in a high yield post-clamped array. More examples are provided in Figure D.4 and D.5. Other defects such as chained and multiple NWs are rarely seen, following our control of NW concentration. The inset shows a single clamped NW suspended about 500 nm above the electrode surface and free to serve as a mechanical resonator.

Since post-clamped yield can be lower than the yield from the assembly process alone, for a meaningful comparison of the results of different approaches, it is important to check which one is implied in published reports. For example, the 80% yield quoted in the work of Li *et al.* [14] refers to post-clamped yield and may be compared with the 88% yield in the current study. Freer *et al.* [39] and Collet *et al.* [40] each introduce innovations, with new directors for yield enhancement. Using microfluidic channel flow [39] and capillary force [40], yields of 98.5% and 81% respectively, are reported by these groups. These studies do not attempt clamping, hence, the numbers from these studies should be compared with the pre-clamped yield of 94% in this work.

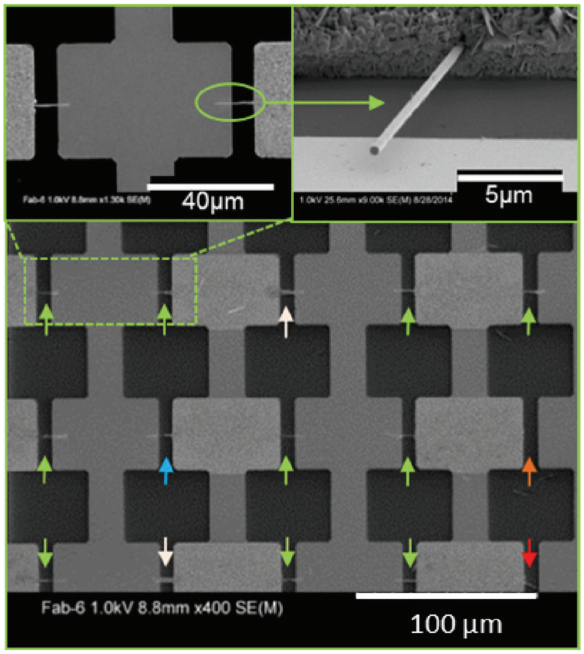

Figure 3.8: High yield clamped single NW and defects. Green arrows: perfectly positioned and clamped NWs; blue arrow: a broken NW after clamping and removing photoresist; white arrow: NW bundle instead of single NW; orange arrow: no NW; red arrow: misaligned NW.

3.2.6 Towards a Generalized Director-Disruptor Framework

The entry to the literature on electrohydrodynamic (EHD) field-directed assembly of NWs to date may seem daunting to a new user. This comes from the fact that a number of effects such as DEP, electroosmosis, electrode polarization and electrothermal are involved, with varying roles reported in different studies. A few examples listed in Table 3.2, show that the same effect can serve either as a director or disruptor. For example, capillary force at moving front is a disruptor in this work and a director in [40]; positive DEP (pDEP), the main director for all studies, can be a disruptor at high magnitudes [25, 39, 40] as it can cause NW to attach on the electrodes instead of in the gap between them [40] or lead to positioning more than one NW between electrodes [25, 39]; low pDEP is identified as a director in [78] and a disruptor in [41] and in our study. The intensity of each effect as well as its degree of coupling to others, varies in these studies. Further, each one of several physical parameters such as geometry, material properties and frequency and magnitude of applied voltage, can contribute to more than one effect.

The focus of this study is the introduction of a general framework for field-directed

NW assembly processes, not limited to DEP, which will help to choose parameter values to maximize device yield. For any field-directed assembly process we propose a systematic procedure with the steps listed below. Sections of this paper where the work done serves as an example for each step, are noted in parenthesis below:

1. List the relevant effects and identify the physical parameters involved for each one. See Sections {3.2.1 and 3.2.2}.

2. Identify each effect as a possible director or disruptor. Sections {3.2.1 and 3.2.2}.

3. Where possible, estimate which disruptors are too weak to be significant; discard them. Sections {3.2.1.4 and 3.2.1.5}.

4. Identify disruptors that are not strongly coupled to any director -remove them, wherever possible, by experimental modification. Sections {3.2.1.1, 3.2.1.2 and 3.2.1.3 }.

5. Examine remaining effects for which director-disruptor coupling could be strong -typically where both are either increased or decreased by the same change in any single physical parameter. Section {3.2.2}.

6. Use physical intuition, experiments, analysis or computation, to seek a minimal set of the simplest non-dimensional parameters that represent the competition between the remaining directors and disruptors well enough to be indicators of yield. Section {3.2.4}.

For the example protocol of DEP discussed in this work, using steps 1 to 6, we found that a single non-dimensional parameter, the yield index, can be used to represent the competition between the director (pDEP) and the strongly-coupled disruptors (electroosmosis and electrode polarization).

The number for the yield index should *not* be interpreted as the expected value of pre-clamped NW yield -*e.g.* a yield index of 0.94 is not the same as 94% pre-clamped yield. The yield index β we have defined has value 1 if the disruptors are negligible and value 0 if the disruptors dominate and prevent DEP from functioning. The value of β is a guide which tells us how to move in the direction of disruptor reduction. We first determined frequency (here, 10^5 Hz) to make β close to 1. Further increase in the frequency would yield small disruptor reduction, but it would significantly reduce the DEP force due to reduction of $Re[F_{CM}]$ as discussed in Section 3.2.4. Therefore,

Table 3.2: Table of comparison: identifying director and disruptor forces influencing the yield of single NW assembly in selected studies focused on increasing the yield of individually addressable single NWs. Effects marked by ‡ are classified as director or disruptor by us, based on qualitative information provided in the source. pDEP and nDEP refer to positive and negative dielectrophoresis.

Source	Director	Disruptor	Method
This work	• pDEP • Capillary inside wells	• nDEP • High NW concentration • Capillary at drying front • Electroosmosis • Electrode polarization • Low pDEP at very high frequency • Electrothermal fluid flow	Analytical & experimental
Collet *et al.* [40]	• pDEP • Capillary	• Very high pDEP • Electrode polarization ‡	Analytical & experimental
Palapati *et al.* [78]	• Low DEP force at pDEP to nDEP transition frequency	• Electrode polarization	Computational & experimental
Freer *et al.* [39]	• Hydrodynamic drag force in microfluidic channels • pDEP • Electrostatic repulsion between NW-NW and NW-electrode	• Very high pDEP • Hydrodynamic drag force in microfluidic channels	Analytical & experimental
Burg *et al.* [42]	• pDEP	• Electrothermal fluid flow • Electroosmosis	Computational & experimental
Raychaudhuri *et al.* [41]	• pDEP	• Electroosmosis • Electrode polarization • Low pDEP at very high frequency	Analytical & experimental
Li *et al.* [14] Smith *et al.* [75]	• pDEP • Capillary inside wells	•Electrode polarization‡ • Capillary in drying front‡	Analytical & experimental
Boote and Evans [25]	• pDEP	• Very high pDEP • Electrode polarization‡	Analytical & experimental

we fixed the frequency. In order to increase the DEP force to try and achieve the best yield possible, the applied voltage was increased, as shown in Figure 3.4.

The primary use of the yield index discussed here for this example use of DEP, is to determine the frequency that moves index β closer to the value 1, after first eliminating weakly-coupled disruptors. We note, however, that the framework with resulting equations, can be useful even after a good working set of parameters for high yield index is finalized, and a high yield experimentally confirmed. Experimental considerations other than those related to the DEP assembly, may impose a new constraint on one of the parameters such as electrode gap size, property of the medium, or the frequency of the field. Considerable effort would be required to arrive at a new set of parameter values by experimental trial-and-error alone. Following the steps of the framework and equations given in Sections 3.2.1, 3.2.2 and 3.2.4, one can quickly obtain working estimates for remaining parameters, and use them to guide experiments confirming the best values.

This approach enabled a selection of physical parameters to significantly improve the post-clamped yield with respect to the earlier study of Li *et al.* [14] and obtain pre-clamped yield value close to the maximum yield reported to date by Freer *et al.* [39], but without the additional experimental cost and complexity of implementing microfluidic channels.

3.3 Conclusions and Outlook

Field-directed assembly enables large-area coverage with individually addressable NW devices. The assembly cost is independent of area, with potential to aid nanoscale research and to open a path for nanomanufacturing. This study introduces a general director-disruptor framework of steps for any field-directed NW assembly process.

One of several directed assembly methods from the literature with positive dielectrophoresis as the main director was selected to serve as an example, to test the utility of the framework. We identified potential disruptors and estimated those that were weak, or weakly-coupled to the director. With guidance from analysis, computation, or experiment in this and earlier published work, we eliminated weak disruptors and defined constraints between variables for the weakly coupled disruptors. We then proposed a definition for a non-dimensional yield index, to capture the competition between the remaining disruptors and directors. The identification of constraints, as well as the definition of appropriate dimensionless parameters, improves intuition about the assembly process, reduces the dimension of parameter space and enables the determination of parameter values with far less trial-and-error. The values of several experimental parameters, such as electrode area and gap size, properties of the suspension medium and frequency of the applied field, were reflected in the yield index. Guided by the variation of the yield index, we obtained the maximum yield (88%) of functional (post-clamped) devices among published reports we have found in the literature to date.

The constraints and dimensionless parameters (such as the yield index here) should be determined afresh for any new field-directed assembly method. Once determined, they provide a rational path for selecting new parameter values, with greatly reduced trial-and-error, if any experimental parameter needs to be changed for reasons other than assembly process. In doing so, the director-disruptor framework has potential to serve as a vehicle for better understanding of the process, and for providing a rational, economical path towards design of a nanomanufacturing process for commercial and scientific use of large arrays of NW devices.

3.4 Experimental Methods

3.4.1 Nanowire Synthesis

We used rhodium (Rh) NWs that have desirable mechanical properties for resonant mass sensing as they retain high quality factor (Q-factor) from high vacuum to near atmospheric pressure [14]. Rh NWs were synthesized in porous membranes from an aqueous rhodium sulfate solution (RH221D from Technic). NWs with length up to 12 μm were synthesized by electrodeposition at -400 mV with respect to a Ag/AgCl reference electrode in 60 minutes [88]. Nanoporous AAO membranes with 200 nm nominal pore size and thickness of 60 μm (Whatman) and polycarbonate membranes with 400 nm nominal pore size and thickness of 20 μm (Sterlitech) were used for NW synthesis. NWs extracted from polycarbonate template have a better cylindricity compared with the NWs synthesized in AAO templates. If the functionality of the resulting device depends on cylindricity of the NWs, using polycarbonate templates is recommended. After dissolving the template (AAO by 3M NaOH and polycarbonate by dichloromethane), the NWs were suspended in ethanol. Electrodeposition experiments were controlled using a Princeton Applied Research VersaStat3 potentiostat/galvanostat. A detailed discussion of the NW synthesis is available in earlier work [88].

3.4.2 Nanowire Concentration Measurement

A known volume of NW suspension was dried on a silicon substrate. Fifty non-overlapping optical micrographs, including center and edge regions of the dried-out drop were analyzed using ImageJ software and the average was used to compute the total number of NWs in the sample. We found that concentrations above 3.3×10^8 NW/mL result in multiple layers or clumps of NWs on the substrate which does not allow for a credible count for NWs with this method. For assembly, we found that a concentration two orders of magnitude below this value was required to prevent chaining and multiple NWs per die. Hence, measurements of concentration made for the assembly are far below this limit.

3.4.3 Nanowire Assembly

Six separate dies, each with 9500 NW assembly sites defined by electrode pairs with different gap sizes, were patterned using photolithography and metal lift-off on a silicon substrate with 300 nm of wet thermal oxide. Figure 3.1 illustrates the following patterning steps: (a) patterning a $\sim$1 μm thick layer of deep ultraviolet (DUV) PMGI SF-11 photoresist (MicroChem) hard-baked (at 200°C for 5 min) to create wells for trapping NWs between each electrode pair. The wells are $\sim$500 nm deep with lengths of 12, 14 and 16 μm for electrode gap sizes of 6, 8 and 10 μm respectively. (b) micro-pipetting 10 μL of suspension over each die, with AC voltage (frequency and voltage value determination discussed later) applied across all chosen electrode pairs to trap NWs within wells. A layer of Shipley 1811 photoresist (MicroChem), $\sim$1 μm thick was then spun and patterned to create a photoresist mask for exposing the PMGI layer over one electrode of each pair, to enable clamping of the NW end. (c) electrodeposition of Ag, from Silver Cyless (succinimide) solution (Technic), to clamp one end of the NWs followed by removal of all photoresist and critical point drying.

PMGI photoresist was chosen in this process for several reasons. Ethanol dissolves Novolac-based photoresists such as Shipley 1811, but it does not dissolve the hard-baked PMGI photoresist. Therefore, the electric-field assisted NW assembly, using NW suspended in ethanol, was conducted on hard-baked PMGI as an insulating layer to prevent short circuit occurrence for the large-scale NW assembly. Finally, Shipley 1811 and hard-baked PMGI can be exposed at different wavelengths, enabling patterning of PMGI using DUV flood exposure through the Shipley mask.

The chief advantages of this fabrication sequence are: {a} capture of NWs at predetermined well locations {b} retention of NWs by capillary force at the surface of the evaporating medium inside the wells {c} removal of randomly scattered NWs with the photoresist in the last step. This fabrication method eliminates the disruptive effect of a high value of the dielectrophoretic (DEP) force, reported by Collet *et al.* [40], which causes undesirable NW attachment at several points on the electrodes.

The dielectrophoretic assembly process was performed using a Signatone 1160 probe station. A function generator (Tektronix CFG253) was used to apply frequencies up to 100 kHz and voltages up to 7 V (rms). A Canon 60D digital camera was used to observe the assembly of NWs. Post-clamped NWs were studied using Field Emission Scanning Electron Microscopy (FESEM, Hitachi S-4800).

3.4.4 Nanowire Yield Measurement

The percentage yield was computed from 500 out of 9500 randomly selected wells per die (3000 of 57000 wells per wafer). Optical micrographs provided in supplementary online documentation (Figure D.2 to D.5 in Appendix D) show blank sites and other defects observed in the counting process. For measuring pre- and post-clamped yield, if multiple NWs were positioned between electrodes, only one NW per electrode pair was counted. Also, if a positioned NW bridged less than half the gap-width as shown in Figure D.4 , it was not counted.

Chapter 4

Nanoresonator Measurement: Suitable Fabrication Design

Nesonators with the assembly method described in the previous two chapters, are suitable for sensing applications. In mass sensing, biomolecules attached to the nanoresonator surface, cause a shift in the resonance peak frequency as shown in Figure 4.1. The resonance frequency of an actuated nanoresonator is evaluated from the resonance spectrum by driving the resonator over a swept frequency range. Different techniques can be used for NW actuation.

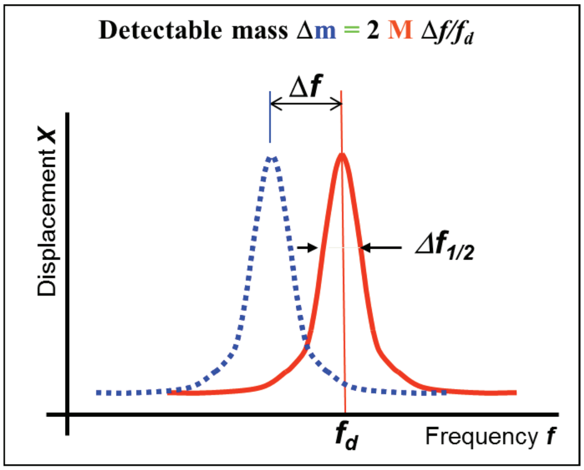

Figure 4.1: Schematic of mass detection. The shift in resonance frequency is caused by small mass attached to the nanoresonator.

This chapter briefly describes the measurement setup and two different actuating methods that can be used; piezo disk actuating and electrostatic actuating. In the former actuating method, a piezo disk is used to drive the entire chip, while, in the latter method, electrostatic actuation is used to drive one or a small number of NW resonators. To be able to use each of these methods, two different fabrication designs were used.

There are two main parts in this chapter; fabrication defects that can disrupt transduction of the nanoresonators (Section 4.2), and issues associated with geometric defects of the NWs that can affect the transduction (Section 4.3). The fabricated nanoresonators resulting from this Ph.D. work were used for NW resonant measurement by my colleague Nima Moghimian [63]. The measurement results are not included in this document.

4.1 Resonance Frequency Measurement Setup

Nanoresonators fabricated in this work were characterized with a non-intrusive optical technique [63]. The steps for resonance frequency measurement mainly include mounting the chip on a piezo disk, loading the piezo disk into the chamber, pumping the chamber to desired vacuum level, laser alignment to individual resonator, and resonance spectrum collection. The vacuum chamber was secured on an inverted optical microscope that was used to focus a laser onto the free end of the cantilevered NW resonator through a 40X objective. The resonance measurement setup is shown in Figure 4.2(a) and (b).

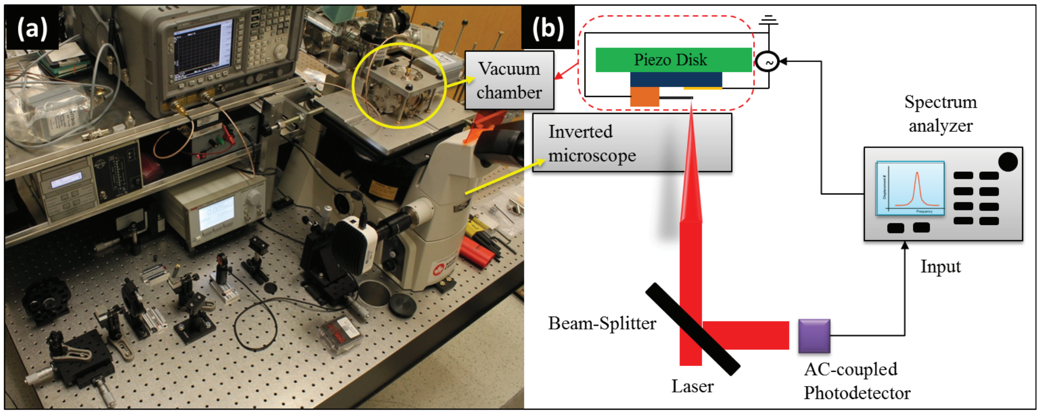

Figure 4.2: (a) Laser setup used for resonance frequency detection. (b) Schematic of the measurement setup to measure the resonance of NW resonators.

After integration of nanoresonators, one die was mounted on a piezo disk using indium metal soldering.The piezo disk and the die were then mounted on the Cu pillars as shown in Figure 4.3. Wires were bonded from the chip and connected to the feedthroughs on the flange for piezo disk and electrostatic actuating as will be explained in section 4.2.1 and 4.2.2. The flange and the piezo disk were loaded into the measurement vacuum chamber, with the chip facing down as shown in Figure 4.2(b).

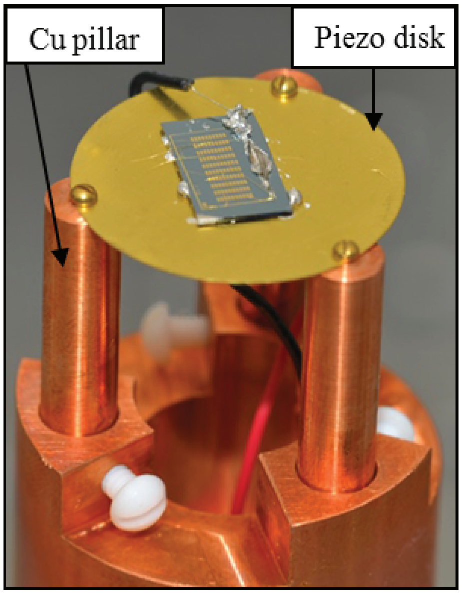

Figure 4.3: A chip mounted on a piezo disk. The electrical feedthrough on the flange can be used to apply AC voltage for both piezo disk and electrostatic actuation.

A 10 mW laser (wavelength=633 nm), providing approximately 3 mW input power for measurement, was focused on the free end of the NW resonator on the chip. The light reflected off the vibrating NW surface and chip substrate, generated the signal tracking the frequency and amplitude of the NW vibration. By using a beam splitter, as shown in Figure 4.2(b), the optical signal was guided to a photodetector where the signal was converted to an electrical signal. An RF spectrum analyzer (Agilent E4402B) displayed the resonance curve and allowed evaluation of the peak frequency. The frequency corresponding to the peak amplitude is the damped resonance frequency (f_d in figure 4.1). The pressure of the measurement chamber was controlled by a turbo-molecular pump placed in series with a dry backing pump, which allowed the chamber pressure to be controlled from 10^{-8} torr to 1 atmosphere by pumping out or feeding in pure (10 ppm impurities), dry nitrogen.

Knowing the measurement setup, different possible actuation methods, piezo disk and electrostatic, are explained in the following sections.

4.2 Different Actuation Methods and Related Fabrication Design

The fabrication design used for piezo disk actuation of nanoresonators is different from the one used for electrostatic actuation since each of these actuating methods have different design requirements. This section provides information about different fabrication designs used in this work. In addition, fabrication flaws that can cause difficulties in nanoresonator transduction, as well as guidelines to prevent these mistakes, are provided.

4.2.1 Piezo Disk Actuation

In this method, a piezo disk, driven by an AC voltage, was used to induce oscillations of the resonators. The piezo disks were extracted from commercial piezo buzzers (NEXXTECH) to drive NW resonators with resonance frequencies ranging from 1 MHz to 10 MHz. The piezo disk contained 3 layers: a brass substrate, a piezoelectric film, and an aluminum contact. This stack is shown in Figure 4.4.

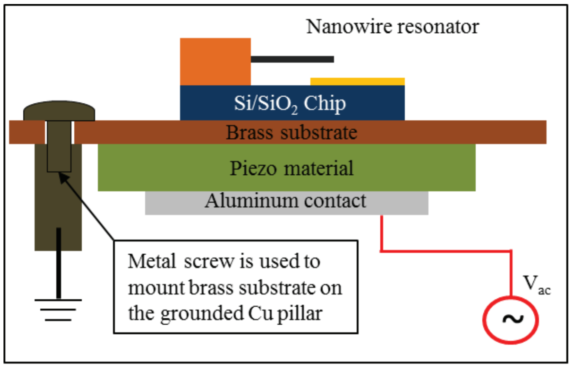

Figure 4.4: Schematic of piezo disk actuation.

The brass substrate of the piezo disk was grounded by mounting it on the flange through Cu pillars and a Cu block. The red wire, shown in Figure 4.3, connected one of the two electrical feedthroughs to the aluminum contact on the piezo disk and was used to deliver the AC signal to the piezo disk. During the measurement, the AC voltage induced the vibration of the piezo disk and drove all of the resonators on the chip. The AC voltage was swept over a range of frequencies that was centered around the resonance frequency of the NW resonator being measured.

In this method, all NWs resonate at the same time. However, resonance frequency of each NW is measured separately by focusing of the laser beam at the tip of each resonating NWs. When the length of the nanoresonators varies over the chip, to detect frequency peak from shorter NWs, a higher voltage needs to be applied, which increases the displacement of longer NWs. If the gap between the suspended end of the NW and the substrate is too small, long NWs may attach to the substrate by van der Waals force. This can decrease the number of functional nanoresonators on a substrate. The impedance of the piezo disk can vary significantly and this can generate a non-uniform driving force on the NW resonators during the measurement, particularly when large frequency spans are involved [35]. Under these circumstances, it is difficult to analyze the resonance performance. In such case, electrostatic actuation may be preferred.

4.2.2 Electrostatic Actuation

In electrostatic actuation, an AC voltage, V_{ac}, is applied between the clamp and driving electrode as shown in Figure 4.5. An electric field is produced between the resonator and the driving electrode and induces a charge on the resonator. The generated electrostatic force drives the nanoresonators. Using this actuation technique, we can selectively drive one or a few nanoresonators at a time.

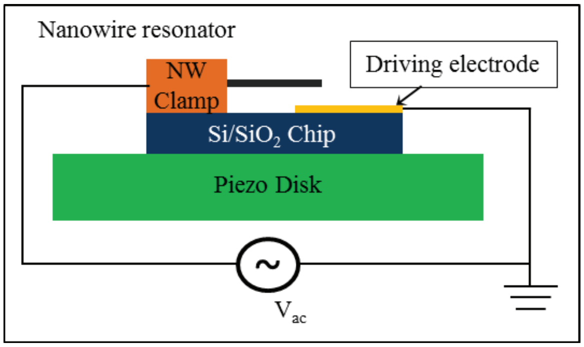

Figure 4.5: Schematic of electrostatic actuation. The AC voltage applied between the clamp and driving electrode is used to drive the NW.

4.2.3 Fabrication Design Used for Piezo Disk and Electrostatic Actuation

In design #1 (D1), shown in Figure 2.3, one electrode (marked with a white star) could be used to actuate all nanoresonators on a chip electrostatically. However, if the suspended end of a NW adheres to the driving electrode during assembly of the nanoresonators, an electrical short prevents electrostatic actuation of all nanoresonators on the substrate. An electrical short circuit is not a possibility in piezo disk actuation. This is one of the main advantages of piezo disk actuation over electrostatic method.

D1 is suitable for piezo disk actuation. To drive nanoresonators electrostatically, design #2 (D2) was used for nanoresonator assembly. The differences between D2 and D1 that make D2 a better fabrication design for electrostatic actuation are noted below:

1. One issue that was addressed by using D2 was the electrical short circuit. In D2, the distance between adjacent electrode pairs was chosen to be 200 μm instead of 60 μm in D1. In both designs, electrode pairs were connected through a gold bar. If an electrode pair is electrically shorted in D2, focused ion beam (FIB) or a sharp probe tip can be utilized to isolate the faulty nanoresonator by removing the gold bar. Whereas in D1, the small gaps between electrode pairs make it impossible to remove gold bars by using sharp probe tip without destroying the adjacent nanoresonators. FIB instead, could be applicable as it provides a precise cut. Figure 4.6 shows SEM image of a gold bar electrically disconnected by using FIB. However, for D1, this approach is time-consuming and may even cause the failure of the NW device when high doses (combination of high accelerating voltage, current, exposure time or number of passes) of ion beam are used. Therefore, larger gap size between adjacent electrode pairs in D2 made the isolation easier and enabled electrostatic actuation.

2. Another issue addressed in D2 was preventing actuation of all nanoresonators on a chip at the same time that could cause adhesion of longer NWs during peak frequency measurement of a short NW. In D2, each five electrode pairs have a separate driving electrode and therefore, nanoresonators can be selectively driven (Figure 2.3 inset).

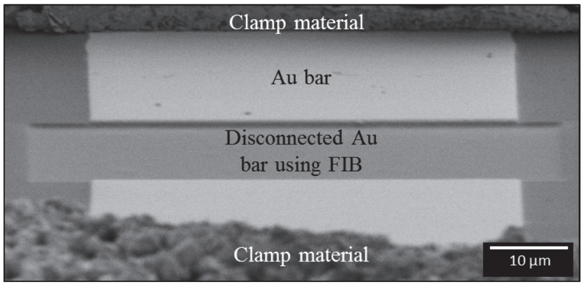

Figure 4.6: FIB-milled slot used for isolating two bridged pads by removing part of a gold connection bar.

4.3 Effect of NW Geometry on Performance of Nanoresonators

This section briefly explains the effect of length and diameter of nanoresonator in resonance frequency measurement. The suspended length of clamped NWs and uniformity in shape and diameter throughout the length directly affect the performance of the nanoresonators. This section focuses on several fabrication considerations in order to assemble a perfectly cylinder nanoresonator with measurable suspended length.

4.3.1 Nanowire Length

As mentioned in Section 2.3.2, in the absence of a sorting technique, short NWs can be clamped however, they may not produce a functional device. The proper suspended length for nanoresonators, enabling actuation and detection is shown in Figure 4.7. The free end of the NW resonator can be either suspended on top of (Figure 4.7(a)) or very close to (Figure 4.7(b)) the underlying driving electrode. The resonance frequency of NW resonators in both configurations can be measured using both piezo disk actuation and electrostatic actuation. However, when a NW does not have an overlap with underlying driving electrode (Figure 4.7(b)) less light reflects back to the detector which makes signal detection for resonance peak challenging compared with longer NWs.

The dependence of the resonance frequency of a cantilevered beam, on geometry, material properties and clamping when modeled as a harmonic oscillator in a low damping environment such as high vacuum, is shown in Eq. (4.1):

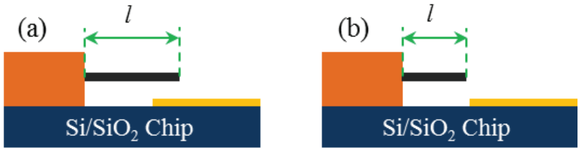

Figure 4.7: Two configurations of nanowire resonators with suspended length of l.

$$f = \frac{\beta_n^2}{8\pi}\sqrt{\frac{E}{\rho}}\frac{d}{l^2} \tag{4.1}$$

where E, ρ, d and l are the Young's modulus, density, diameter and suspension length respectively, n is the mode number and β_n is the associated eigenvalue. For example, the first three modes have eigenvalues of β_0=1.875, β_1=4.694 and β_2=7.855.

Eq. (4.1) enables calculation of NW properties such as Young's modulus [14, 63] if length and diameter of the NWs can be measured. Knowing f from Eq. (4.1), the quality factor (Q-factor) [14] can be also calculated. Q-factor expressed by:

$$Q = 2\pi\frac{mf}{C} \tag{4.2}$$

where C is the damping term, m is the mass and f is the resonance frequency. For Q$\gg$1, f reduces to f_0. Under this condition, Q can be rewritten as:

$$Q = \frac{f_0}{\triangle f_{1/2}} \tag{4.3}$$

where $\triangle f_{1/2}$ is the full width at half-power maximum of the resonance spectrum as shown in Figure 4.1.

Generally, suspended length l is measured from the edge of the clamp electrode to the tip of the NWs by using SEM images. However, some fabrication flaws can make this measurement challenging. An example of fabrication defect that can occur during the photolithography step for opening the clamp windows, when the clamp mask is misaligned with respect to the clamp electrodes, is shown in Figure 4.8. The clamp mask was shifted to the left (see Figure 4.8(a)). Therefore, the photoresist covering the NWs beyond the left-hand-side edges of the clamp electrodes was exposed. As well, on the right-hand-side edges, photoresist layer remained unexposed. Accordingly, after developing the photoresist and electrodeposition step, the clamp material was deposited on the exposed part of the NWs on the right-hand-side edges, as shown in Figure 4.8(b) and remaining photoresist on the opposite edges, prevented electrodeposition of the clamp material, shown in Figure 4.8(c). This defect can cause uncertainty in measuring the suspended length of the nanoresonators.

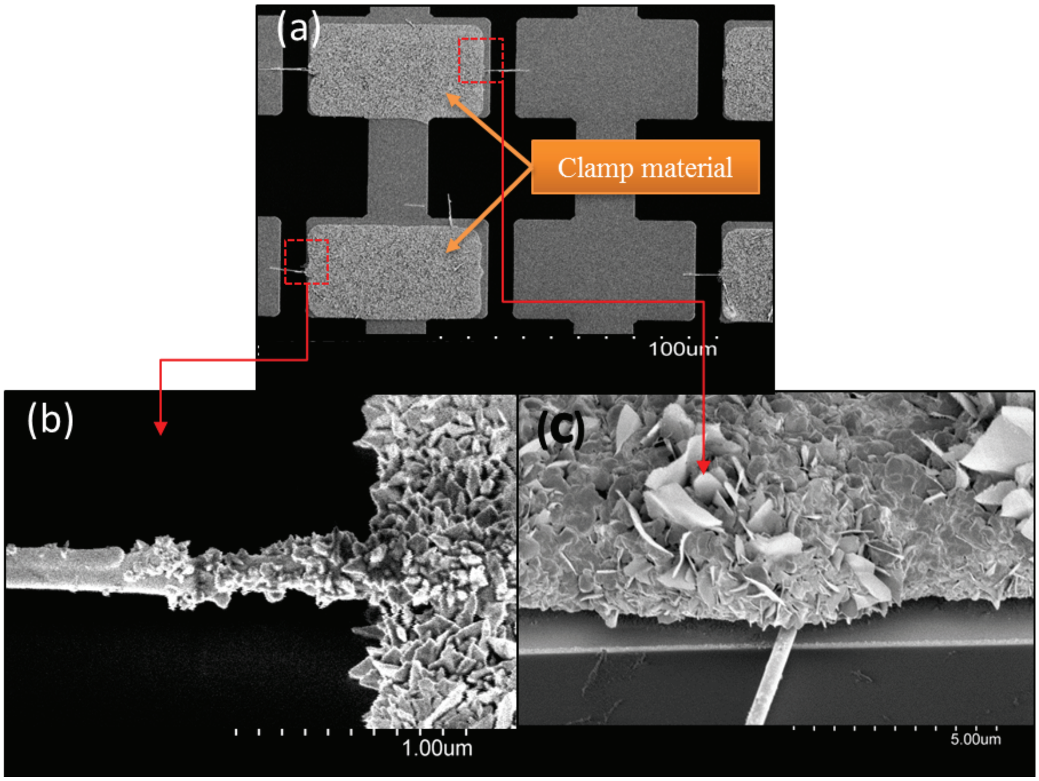

Figure 4.8: Effect of misaligned clamp mask. (a) Clamp mask was shifted to the left and caused (b) deposition of clamp material on the NW beyond the edge of the clamp electrodes while (c) remaining photoresist on the opposite edge, prevented deposition of the clamp material on the NW end placed over these edges.

4.3.2 Nanowire Diameter

As mentioned, besides length, the diameter of NWs also affect the values of Young's modulus and the damping coefficient, obtained through resonance measurements. The uniformity of diameter and surface quality of the NWs are dictated by the shape and quality of the pores in the porous membrane. In this work, NWs were synthesized from two different porous membranes, anodized aluminum oxide (AAO) and polycarbonate (PC).

Anodized aluminum oxide (AAO) template (Whatman) used in this research had 60 μm thickness and nominal pore diameter of 200 nm. One difficulty with NWs extracted from this template was the non-uniform geometry of synthesized NWs.

Although the nominal pore size of the template was 200 nm, the pore size varies throughout the pore and results in NWs that are not perfect cylinders. Figure 4.9 (a) clearly shows the existence of the branches in NWs synthesized inside the AAO membrane. Figure 4.9 (b) shows a nanoresonator integrated by using defective non-cylindrical NW.

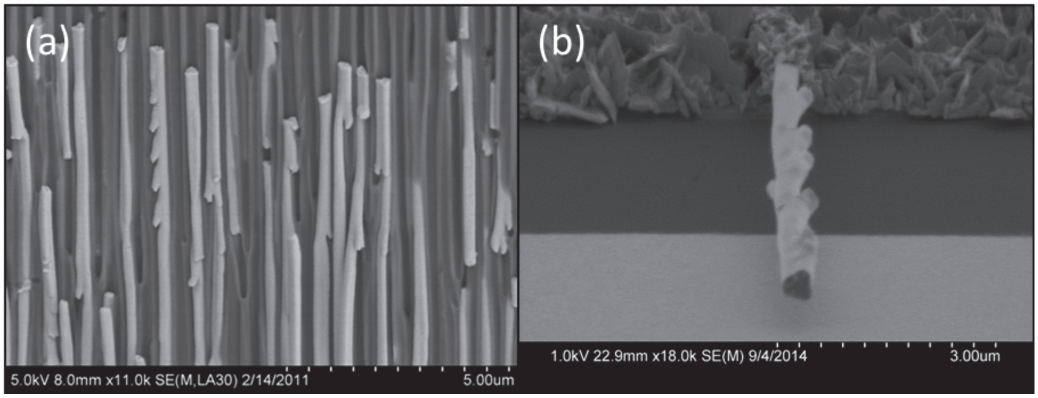

Figure 4.9: Defective NWs grown inside AAO porous template. (a) Cross section of NWs grown inside AAO pores [63]. (b) Integrated nanoresonator.

Operating mass detection experiments or other related measurements will be challenging using NWs synthesized from AAO membrane as the shape and diameter of the NW can vary throughout its length.

In order to solve this problem, polycarbonate (PC) membrane, with 25 μm thickness and nominal diameter of 400 nm, were used in this research. SEM image of Rh NWs extracted from PC membrane is shown in Figure 4.10(a). Figure 4.10(b) shows that NWs are perfectly cylindrical, have better surface quality and uniform diameter throughout the length. However, several issues were involved in NWs extracted from these membranes. PC templates are commercially made to serve as filters, therefore the pores are mainly criss-crossed through the thickness of the polymer [63]. The pore-connection degree is high and hundreds of NW clumps are created from each membrane (see Figure 4.10(c)). This structural defect is the most significant problem associated with PC membranes for fabrication of nanoresonators.

During nanoresonator assembly, these NW clumps can bridge clamp and driving electrodes and prevent electrostatic actuation as shown in Figure 4.11(a). Low concentration of single NWs, due to high pore-connection degree, and high diversity in NW length (2 to 8 μm) as a result of NW-clumps breakage, are other issues associated with NWs extracted from PC templates. The short length of these NWs can cause

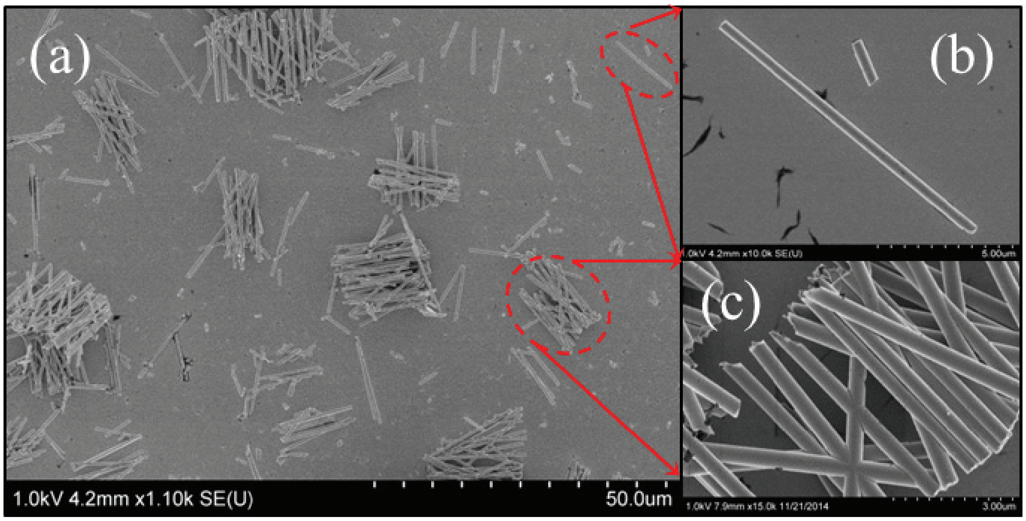

Figure 4.10: (a) Geometry of NWs extracted from polycarbonate porous membrane. (b) Resulting NWs show uniform geometry. (c) However, criss-crossed pore pattern causes NW clumps.

fabrication of many non-functional nanoresonators as seen in Figure 4.11(b)

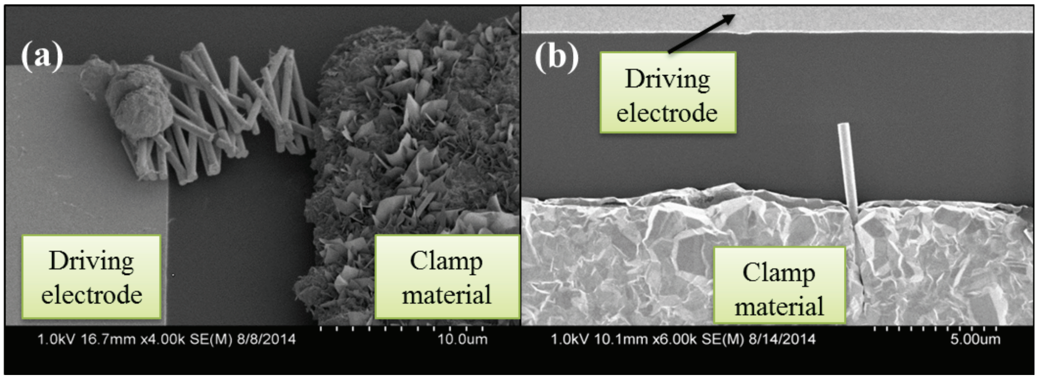

Figure 4.11: Defects caused by NWs synthesized from polycarbonate template. (a) Clumped NWs can connect clamp and driving electrodes which prevents NW actuation electrostatically. (b) Synthesized single NWs can be short.

In order to use the PC-extracted NWs for nanoresonator integration, a sedimentation technique was required to remove heavy clumps. Our observation showed that by leaving the NW suspension for 3 to 10 min, big NW clumps sediment at the bottom of the test tube. The NW suspension from top half of the test tube was transferred to a new test tube by using micropipettes. This NW suspension was then used for NW assembly. However, it was not possible to remove all clumps by using sedimentation method and remaining clumps could still cause electrical short during nanoresonator integration. Therefore, isolation of the electrically-shorted parts of the substrate was required for actuating the nanoresonators.

Design #2 was appropriate for assembly and integration of NWs from PC templates since it enables isolation of the electrically-shorted electrode pairs and actuating small number of nanoresonators separately from the rest of the nanoresonators on the substrate. To be able to capture and clamp these short NWs, the electrode gap size in D2 was chosen as 3, 4 and 5 μm. The resulting integrated nanoresonators are shown in Figure 4.12.

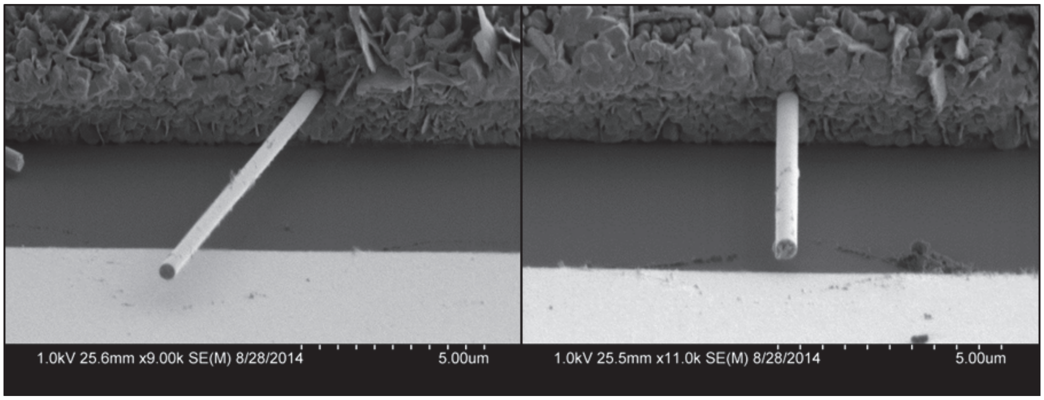

Figure 4.12: Nanoresonator integrated from polycarbonate-synthesized NWs, assembled and clamped using design #2.

4.4 Conclusions

This chapter presented the measurement setup and the two different actuation methods used to characterize NW resonators. In the first actuation method a piezo disk was used to drive entire nanoresonators on a chip. In the second method, one or a small number of NWs were driven electrostatically. Two different fabrication designs, suitable for each actuation technique, were introduced. The design D1 which was used for piezo disk actuation, had a high number of assembly electrode pairs with gap sizes of 4, 6, 8 and 10 μm. NW with lengths between 8 and 12 μm, synthesized in anodized aluminum oxide templates, were long enough to be integrated into these gaps.

If during nanoresonator assembly, the suspended end of nanoresonators adhere to driving electrodes, a short circuit prevents electrostatic actuation. Due to the small gap between adjacent nanoresonators in D1 it was impossible to isolate faulty nanoresonators without using focused ion beam. However, a high number of electrode pairs in this design increases the possible number of shorted electrode pairs and therefore, using focused ion beam will be time-consuming. In addition, the NWs with perfect cylindricity fabricated in polycarbonate templates were too short for gap sizes in D1. Therefore, design #2 (D2), with smaller electrode gap size (3, 4 and 5 μm), was used for nanoresonator integration. D2 provides smaller number of integrated nanoresonators on a chip but enables driving only one or a small number of nanoresonators at a time. In this design, a larger gap between adjacent electrode pairs enables isolation of electrically shorted electrode pairs by scratching through with a sharp probe tip instead of FIB, without destroying the nanoresonators.

4.5 Future Work

One major problem in nanoresonator transduction concerns the ability to isolate nanoresonators. In future work, new design having two different metal layers (e.g., use Au for the clamp and driving electrodes and use Ag metal lines to connect the Au electrodes) could be used to isolate pairs of electrodes by selective wet etching of the Ag after the device fabrication is completed.

Chapter 5

Field-Directed Chaining of Nanowires

This chapter presents an article published [60] under the title of *Field-Directed Chaining of NWs: Towards Transparent Electrodes*. The article (Materials Letters 163 (2016): 205-208) is reproduced with permission from Elsevier.

Abstract

Nanowire networks on rigid or flexible substrates can be used as low-cost transparent electrodes for displays, photovoltaics and as sensors. Generating an ordered configuration of connected nanowires from disordered suspension requires external forces. We demonstrate chaining of nanowires, using an AC electric field to generate dielectrophoretic force on nanowires adjacent to the electrodes and dipole-dipole interaction between nanowires far from the electrodes. Classifying and controlling forces and parameters that disrupt chaining, we provide guidelines to enable large-area coverage with multiple nanowire chains. Compared with other low-cost techniques such as spray or spin coating, AC electric field assembly provides control over density and connectivity of nanowire chains with potential for fabricating low-cost, high-performance devices.

5.1 Introduction

Covering large surface area with connected nanowires (NWs) is of interest for fabricating devices such as light-emitting diodes (LEDs), liquid crystal displays and solar cells [44, 48]. Several assembly process such as drop casting [16, 89] spray [90], electrospinning [57] and nanoimprinting [56] have been used for NW network fabrication but not all assembly processes offer the combination of speed, simplicity and low cost required for technologically feasible applications. Due to the low fabrication cost of drop casting [16,89] and NW spray [90], these methods are at the center of attention, however, it is difficult to achieve high coating reproducibility from these methods since there is no director force for connecting NWs. Furthermore, in solution-process techniques, annealing is required to remove the additives used for preventing agglomeration which is not required in field-directed chaining.

Dielectrophoresis [36] (DEP), a force exerted on a polarizable particle in a non-uniform electric field, has been introduced as a cost-effective technique that can direct single NWs [3, 14] to pre-determined places on a substrate. Moreover, it also enables NW and nanoparticle (NP) chaining between electrodes [91–95]. Simplicity, ability to direct nanostructures to desired places and high level of end-to-end registry of nanostructures facilitate fabrication of portable and accurate devices such as gas [11] and biomolecule [96] sensors by using DEP.

However, covering a large surface area with DEP-assisted multiple NW chains is challenging. Capillary force at the drying front of the suspension [91] or electrical short circuit after connection of the first chain with assembly electrodes can disrupt chain formation. In this letter, we demonstrate how to overcome disruptive effects to create a network of NWs over a large surface area. The choice of parameter values that enable growth of multiple long chains with reproducible configuration are described following a discussion of the differences between field-directed assembly of single and chained NWs.

5.2 Materials and Methods

In this work, rhodium (Rh) NWs were chained between interdigitated assembly-electrodes (see Figure E.1 in Appendix E) with different gap sizes of 180 and 240 μm. The electrodes were fabricated using 10 nm Cr/100 nm Au metal lift-off on a silicon substrate. Rh NWs were electrodeposited in porous aluminum oxide templates of 200 nm nominal pore size and 60 μm thickness (Whatman), at -400 mV with respect to a Ag/AgCl reference electrode from an aqueous rhodium sulfate solution (RH221D from Technic) with 60 mM concentration of elemental rhodium. To extract the NWs, sections of the template were placed within a test tube containing 3M NaOH. After 15 min sonication the aluminum oxide membrane was dissolved. Following this, the suspension was centrifuged and and supernatant NaOH solution discarded. NWs were then rinsed with DI water and ethanol and finally suspended in ethanol [88].

NW suspension with concentration of 3.3×10^8 NW/mL was introduced over the substrate while AC electric potential of 5 V (*rms*) and 10 kHz was applied. To create multiple NW chains bridging the electrodes, we increased the alcohol evaporation time by using a dam. Several parallel wells were machined within a 2-mm thick polycarbonate sheet to serve as the dam (pictured in Figure E.2 in Appendix E). Adding NW suspension (100 and 120 μL respectively over substrates with 180 and 240 μm electrode gap sizes) NW chains covered the entire substrate.

Resistance of the NWs was measured using a DC voltage applied across the NW chaining electrodes and an external resistance in series. The voltage drop across the external resistance was first used to determine the current (I) in the circuit. The voltage drop (V) across the electrodes with chained NWs was then measured using a probe station. These data were plotted as an I-V curve, found to be linear. The NW chains' resistance was obtained from the reciprocal of the slope of this line.

5.3 Results and Discussion

In single NW positioning [14], assembly-electrode gap size (L_{gap}) is comparable with NW length (L_{NW}) (Figure 5.1(a)), the gradient of electric field is high within the gap and DEP is the dominant force anywhere inside the gap. However, in NW chaining [93–95], when L_{gap} is much larger than L_{NW} (20 to 25 times in our work), we may anticipate two different regions as shown in Figure 5.1(b). (1) A region of high DEP force, adjacent to assembly electrodes, where DEP force directs NWs towards the edge of the electrodes. These edge-NWs become new electrodes with high electric field gradient at their end. (2) A region of low DEP force, in the inter-electrode space, in which polarized NWs may chain together via dipole-dipole interaction. We observed that these small chains move towards the electrodes, where they link to the edge-NWs and create a longer chain.

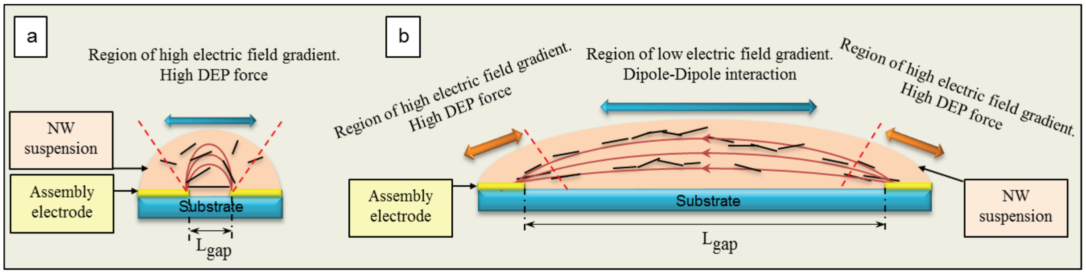

Figure 5.1: Sketch of (a) single NW positioning ($L_{gap}/L_{NW} < 2$) and (b) NW chaining ($L_{gap}\ /L_{NW} \geq 20$).

Based on observed phenomena, we classify chaining into three stages. (1) Initiation: NWs are propelled towards electrode edges, and simultaneously, small chains are generated parallel to the field between the electrodes. (2) Growth: when the linear density of edge-NWs has stabilized, these NWs serve as initiators, and growth of NW chains is observed. (3) Bridging: elongated chains grown from counter electrodes meet and connect.

From initiation to bridging, several factors and forces are involved that can disrupt formation of long chains. The disruptors and guidelines to control them, are discussed below.

5.3.1 Effect of Disruptors on Chain Formation

Disruptive effect of capillary force at the drying front can destroy NW chains when the generated electric field is small. At V_{rms}= 5 V, some of the chains for L_{gap}=240 μm were destroyed by capillary force at the drying front of NW suspension but no chain destruction was observed for L_{gap}=180 μm (Figure 5.2(a) and (b)). One approach to overcome the capillary disruptor is to increase the voltage, thus increasing the electric field. For NWs, $F_{DEP} \propto \varepsilon_m \mathrm{Re}[F_{CM}] \bigtriangledown (E^2)$ where F_{DEP} is the DEP force and E is the electric field. Re[F_{CM}], the real part of Clausius-Mossotti factor, is equal to $(\varepsilon_m^* - \varepsilon_p^*)/\varepsilon_m^*$ where ε^*=$\varepsilon - j(\sigma/\omega)$. Subscripts m and p refer to medium and particle. ε and σ are the permittivity and conductivity, respectively, and ω=$2\pi f$ is the frequency of applied voltage [36]. Although increasing voltage can increase the electric field, which results in stronger field-generated forces for NW chaining, high voltage can become a disruptor unless a sufficiently high number of NWs is provided, as explained below.

When the voltage is applied, edge-NWs, positioned along the assembly electrodes,

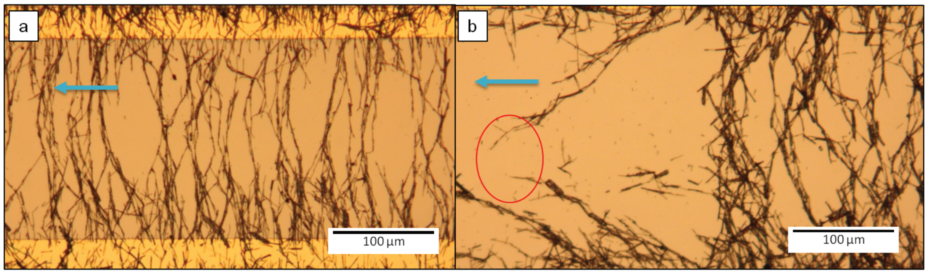

Figure 5.2: (a) L_{gap}=180 μm (b) L_{gap}=240 μm. In (b), capillary force disconnects the bridged chains (marked with red circle). The direction of the drying front of the medium is indicated with blue arrows

.

screen the electric field in their immediate neighborhood, reducing the field strength, which determines the lateral spacing between positioned NWs [97]. Higher applied voltage reduces the NW spacing, with more NWs used up in the initiation step. This results in fewer NWs being available for the growth and bridging steps, as seen in Figure 5.3(a) and (b). Increasing the volume of NW suspension over the substrate prevents this disruption, creating more NW chains bridging the electrodes.

In addition to the magnitude of the applied voltage, its frequency also affects NW chaining. Two disruptors could result from inappropriate choice of applied frequency, electroosmotic force and electrode polarization [83, 85]. These effects result from the presence of an electrical double layer on the surface of assembly electrodes, at frequencies lower than the relaxation frequency of the ions and the polar molecules in suspension. Frequencies higher than relaxation frequency are required to prevent double layer formation and halt the disruptive effect of electroosmosis and electrode polarization. For the assembly-electrode gap sizes and the NW medium used in this work, the ratio between the effective voltage available in the bulk of the medium and applied voltage (V_{eff}/V_{rms}) goes to unity at frequencies higher than 10 kHz. This suggests a negligible thickness of the double layer at these frequencies. Increasing the frequency above 10 kHz is not favorable for NW chaining since F_{DEP} decreases.

Chain growth and bridging can be arrested by another disruptor, a short circuit, which occurs when the first chain ends make contact with both assembly electrodes. A thin layer of dielectric deposited over the electrodes would prevent short circuits, but also isolate NW chains from the electrodes, which is undesirable. Another approach would be to coat NWs with a thin layer of dielectric material [98]. However, this would lead to an undesirable and large increase in the NW-NW contact resistance and hence chain resistance. How could we assemble NW chains and bridge assembly electrodes without an electrical short circuit?

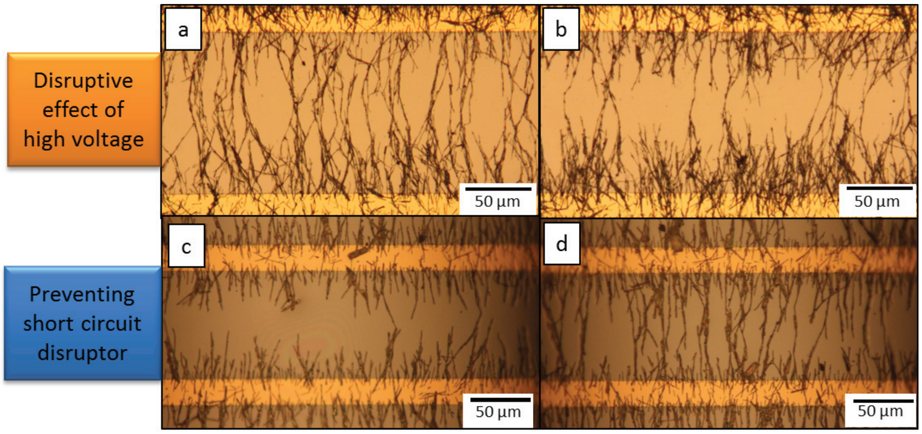

Figure 5.3: Disruptor results: effect of increasing voltage from (a) V_{rms}= 5 V to (b) 7 V. (c) and (d) hovering NWs prevent a short circuit.

In the suspension, a cloud of counter ions adjacent to the substrate and around each pole of the NWs, creates a repulsive electrostatic force, which repels NWs away from the electrodes. A balance between electrostatic repulsion force and DEP attraction force would make NW chains hover above electrodes [97] (gauged by the absence of short circuit). With the large gap sizes chosen to make long chains, we observed that NW chains hovered over electrodes even at 7 V rms, the maximum voltage available to us. Using a dam, NW suspension was replenished in the wells before alcohol dried out completely. Figure 5.3(c) shows that although some chains bridged the electrodes, more bridging occurred by adding NW suspension before alcohol dried out (Figure 5.3(d)). Upon drying, DEP and van der Waals forces pin the NWs to the substrate.

After assembly, we examined electrical characteristics of NW chains generated for gap sizes between L_{gap}=180 and 240 μm at 5 V (rms) and 10 kHz. The resistance measured from current-voltage (I-V) characteristics (Figure 5.4) was 16 and 42 Ω for chains with gap lengths L_{gap}=180 and 240 μm respectively. Further investigation can be done to improve the electrical conductance by sintering the NWs [99, 100].

The aim of this study is to generate multiple chains of NWs covering large surface area. Longer chains or large values of L_{gap} are desirable as they reduce the fraction of area covered by assembly electrodes. This can help increase the transparency of the substrate, as needed for electrode applications. To the best of our knowledge, the longest field-assisted chain was a 3 mm *single* chain of gold NPs [101]. The method demonstrated here enables coverage of large surface area with *multiple* long chains,

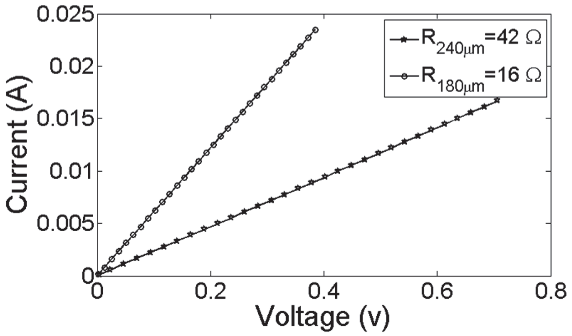

Figure 5.4: Resistance measurement for chains of L_{gap}=180 and 240 μm.

without the disruptive effect of a short circuit. By choosing parameter values that provide large enough director force and prevent disruptors, field-directed chaining of NWs provides a path to create reproducible properties (such as electrical conductivity and light transmissivity) over large surface area and with low fabrication cost.

5.4 Conclusions

We showed that field-directed NW chaining between gaps much larger than NW-length, differs from that for single NW assembly between gaps comparable to nanowire length. While dielectrophoresis is the predominant force for single NW positioning, for nanowire chaining its influence dominates for only a small fraction of the gap region, close to the electrodes. In the region far from the electrodes, dipole-dipole interaction is dominant. Lower electric-field strength in nanowire chaining can make nanowire chains hover above assembly electrodes and prevent electrical short circuits, which enables the covering of large surface area with multiple chains. Forces and parameters that can disrupt NW chaining were noted as capillary force, high voltage with insufficient number of nanowires, electroosmotic velocity, electrode polarization and a short circuit. Guidelines to control them were presented.

This method is not limited by the dimension of the substrate or size and type of polarizable NWs and should help in the development of scalable and cost effective techniques for making sensors and optoelectronic devices.

5.5 Acknowledgments

This work was supported by Canadian agencies NSERC, CFI and BCKDF and made use of the 4D LABS facilities at Simon Fraser University.

Chapter 6

Fabrication of Transparent Electrodes on Rigid Substrates Using Field-Generated Forces

This chapter provides introductory background and experimental results on fabrication of transparent electrodes (TEs) by using field-generated forces. This technique has been used for the first time in this Ph.D. dissertation as a method applicable to TE fabrication. The information provided in this chapter can serve as a guideline to expand this technique in order to improve the performance of the resulting TEs.

6.1 Transparent Electrodes

Transparent electrodes (TEs) combine high optical transparency and electrical conductivity, useful in different areas such as light-emitting diodes (LEDs), liquid crystal displays and in energy conversion devices (*e.g.* solar cells) [45, 46]. A highly competitive market of electronic devices, such as phones and flexible touch screens as well as a worldwide increasing demand for energy, drives research to improve the performance of TEs on rigid and flexible substrates. The earliest group of TEs, transparent conductive oxides (TCO), were thin film of oxides such as CdO, Cu_2O, PbO, ZnO, SnO_2 and In_2O_3 [48]. Among all TCOs, Indium tin oxide (ITO) films show the best performance. However, ITO is expensive and in case of flexible substrates, such as flexible displays and organic solar cells, its elevated fabrication temperature and brittle behavior lead to the formation of cracks, which causes high sheet resistance. These economic and material limitations of ITO have spurred research for alternatives.

Recently, different materials and geometries have been investigated [47] including graphene flakes [102], ultra thin metal films (UTMFs) (<10 nm) [103], patterned thin metal films (TMFs) [104, 105] and nanostructured grids or networks [16, 56, 57, 59]. TEs fabricated by these materials and geometries have shown promising results as their ratio of light transmittance to sheet resistance, ranging from 0.06 to 0.45 Ω^{-1}, is comparable or much higher to that for ITO (0.08 to 0.085 Ω^{-1}). However, work still needs to be done in order to achieve high performance TEs with low fabrication cost.

Commercially available ITO has sheet resistance as low as ∼10 Ω/sq for a transmittance of ∼80% [48]. Among new materials, graphene offers several potential advantages including flexibility, chemical stability and cost. 90% light transmission was demonstrated from solution processed graphene (sonicating bulk graphite in dimethylformamide (DMF)) on a glass substrate [102]. However, the sheet resistance was high, up to 5000 Ω/sq. An approach to increase the light transmission as well as conductivity is to incorporate a conductive material with graphene. Copper NWs coated with graphene [106] demonstrated light transmission of 95% with sheet resistance of 41 Ω/sq. Even though the ratio of light transmittance to sheet resistance of the demonstrated TE is smaller than the one for ITO, progress in TE performance makes research on graphene encouraging. UTMFs, as another alternative for ITO, create even topography, suitable for preventing electrical shunting with overlying layer in devices such as solar cells, but their sheet resistance is high. Thicker layer of films provide better electrical conductivity but reduce the optical transmittance and vice versa. Patterning TMFs can resolve the issue by depositing and patterning a thicker layer of metal (up to 100 nm) to achieve high light transmittance and film conductivity. This can be done in different ways such as patterning a metal film on a UTMF layer [105] or partially removing the deposited metal film [104]. However, in this technique, more than 70% of the deposited material needs to be removed, which is wasteful. While nanostructured grids and networks, made by electron beam lithography (EBL) [59], nanoimprinting [56] or electrospining [57], show performance comparable to or better than ITO, the cost or complexity of these techniques has motivated research on simpler and less expensive fabrication methods such as drop casting [16, 89] (dropping nanostructure suspension on the substrate) or spraying [90] of NWs. However, in these techniques, there is no control on connectivity of the nanostructurs and the only way to increase conductivity is by increasing the concentration of the NWs on the substrate. Therefore, light transmittance is very low for substrates with high conductivity and vice versa. A technique in which a controllable external force directs the connection of nanostructures could help solve this issue.

Dielectrophoretic force (DEP) accompanied by coulomb force, facilitates connectivity of NWs or nanoparticles (NPs) suspended in an electrolyte. Nanoparticle chains have been explored [85, 91–94, 101, 107, 108] and used in highly sensitive and portable devices for gas [11, 12] and biomolecule [96] sensing. However, DEP appears not to have been pursued as a technique for fabricating TEs.

Similar to drop casting and spray, multiple and complicated fabrication steps or expensive equipment are not needed in DEP-assisted NW chaining. In spite of its simplicity, DEP force along with dipole-dipole interaction, controls the connectivity of NWs which is missing in spin coating and spray techniques. In drop casting, since a high concentration of NWs is needed to fabricate a substrate with high conductivity, dispersion of the NWs in the suspension is very important to prevent NW agglomeration. Additives such as polyvinylpyrrolidone (PVP) need to be added to the suspension to achieve this. However, the PVP residue decreases the electrical contact between NWs [89]. A heat treatment step is required in order to remove the additive from the surface of the NWs to enhance the NW-NW connection and maintain low sheet resistance. In DEP-assisted chaining, the repulsive force between similar poles results from polarization of the NWs, preventing NW agglomeration without additives. Accordingly, no additional step, such as heat treatment, is required to remove the additives from NWs.

Figure 6.1 shows NW arrangement in two cases- self assembly of NWs by drop casting and field-generated NW chains. NWs after drop casting are disordered and disconnected (Figure 6.1(a)) while DEP force and dipole-dipole interaction between NWs create an ordered pattern of connected NWs, shown in Figure 6.1(b). Although the same amount of NW suspension was introduced over both substrates, since no director force was involved in Figure 6.1(a) to connect NWs, the degree of connectivity of NWs was very low and NWs were dispersed everywhere on the substrate. However, field-generated forces in Figure 6.1(b) retained NWs between electrodes and controlled NW-NW connectivity. To improve the connectivity of a self-assembled NW network, a higher concentration of NWs is required in drop casting. It implies that where NW connection is directed by an applied electric field instead of a NW concentration, electrical conductivity over the substrate can be achieved using lower concentration of NWs which can result in a higher light transmittance.

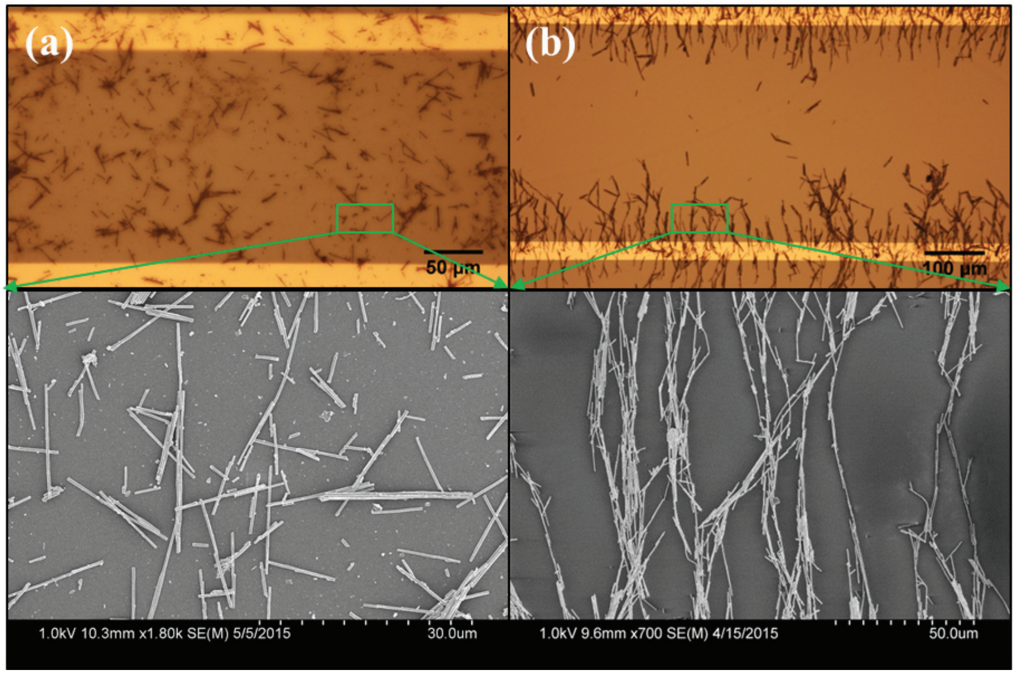

Figure 6.1: Effect of applied electric field on NW connectivity. 10 μl of NW suspension was introduced over both substrates (a) no electric field was applied, (b) an AC field with 5 V (rms) at 10 kHz was applied to the electrodes.

Creating a NW network and patterned thin metal films were discussed as two separate methods for fabrication of TEs. In this chapter, we introduce a hybrid fabrication method, incorporating elements from both techniques. In this method, metal-film assembly electrodes are patterned on a transparent substrate (glass) by using photolithography. The NW network is then created between assembly electrodes by using forces generated by electric field. This method shows many advantages as discussed through this chapter. For example, it is a less expensive method of creating patterned NW network compared with EBL or nanoimprinting. Since the patterned metal films in this case are restricted to a smaller fraction of area compared with patterned thin metal film (TMFs), the transmission loss is less sensitive to film thickness. After noting experimental details, the effect of configuration of the resulting NW network on light transmissivity of the TE is discussed.

6.2 Experiments

Here, formation of NW chains is studied on glass substrates. Interdigitated electrodes with different assembly-electrode spacings (120, 180, 240 μm) were fabricated, using

10 nm Cr/100 nm Au, with a metal lift-off process. Field-generated forces and the resulting chain configuration can vary with electrode spacing and alter the performance of resulting TEs.

To determine NW concentration, several optical images of NWs, dried out from a known volume of suspension, were processed by image process software (ImageJ) to count the number of NWs. The concentration of NW suspension was measured $\sim 3.3 \times 10^8$ NW/mL. NW suspension was introduced over the substrate while AC electric field potential of 5 V (rms) and 10 kHz was applied by using Tektronix CFG253 function generator.

As shown in Chapter 5, a dam was used to prevent electrical short circuit enabling NW chains to cover the substrate entirely. 80, 100 and 120 μL of NW suspension was added, respectively, to substrates with 120, 180 and 240 μm assembly-electrode gap in order to cover the entire substrate with multiple chains. After alcohol completely dried out, substrates were studied under optical microscope as well as SEM (Hitachi S-4800 FESEM). Different chain configurations, as a result of changing the assembly-electrode gap size for the same applied voltage are illustrated in this chapter. Light transmittance of the substrates was measured by using a Varian Cary 50 UV-Vis Spectrophotometer.

6.3 Effect of Chain Configuration and Electrode Geometry on Light Transmittance

This section provides information about the effect of the size of the gap between thin-film assembly electrodes, on configuration of the NW network. Also, the effect of the geometry of assembly electrodes on light transmittance of the resulting TE is discussed here. These parameters affect the performance of the resulting TE and this study provides guidance towards finding suitable physical parameter values for fabrication of high performance TEs. Since a four-point probe measurement tool was not available during this study, it was not possible to measure the sheet resistance of the resulting TEs.

6.3.1 NW Chaining at 5 V (rms)

Chains of NWs between electrodes with 120, 180 and 240 μm electrode gaps created at 5 V (rms) and 10 kHz by adding 80, 100 and 120 μL, respectively, of NW suspension to the substrates. Optical micrographs in Figure 6.2 shown that the linear density of chained NWs (number of NW chains bridging the electrodes per unit length of assembly electrodes) decreased by increasing the gap size. The disruptive effect of capillary force can be clearly seen in Figure 6.2(c) where assembly-electrode gap size is larger than those seen in Figure 6.2(a) and (b). Electric field and magnitude of the field-generated forces were smaller for the substrate with 240 μm electrode gap and in this case, capillary force could overcome field-generated forces and break bridged NW chains. Detached chain segments were agglomerated on the substrate after the NW suspension dried out completely. More images of NW chains with assembly-electrode gap size of 240 μm are provided in Appendix F. Does a smaller linear density of bridged chains cause higher light transmittance?

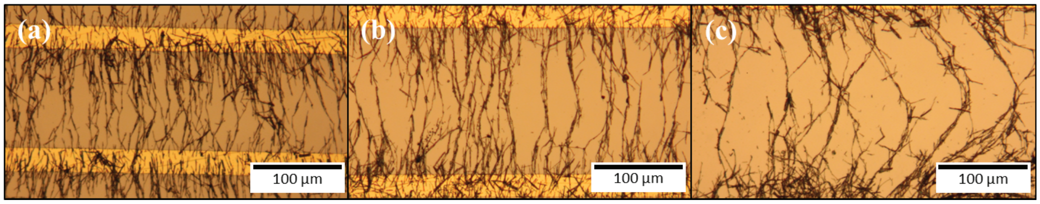

Figure 6.2: Chain configuration alters as assembly-electrode gap size changes from (a) 120 μm to (b) 180 μm and (c) 240 μm. The frequency and magnitude of applied voltage for all three experiments were 10 kHz and 5 V (rms) respectively.

Optical transmission was measured for the three substrates with different assembly-electrode spacing, before NW chaining (blank assembly electrodes). As expected, the results shown in Figure 6.3(a) reveal that the substrate with 240 μm assembly-electrode gap has the highest light transmittance (90%) and the one with 120 μm assembly-electrode gap size has the lowest light transmittance (81%). Figure 6.3(b) is the result of light transmission of the same substrates after NW chaining. The substrate with 120 μm electrode gap size still shows the least light transmittance (65%). However, after NW chaining, the substrate with 240 μm gap size shows less light transmittance (69%) compared with the one with 180 μm (72%). This appears to be contradictory, since the substrate with 240 μm electrode-assembly gap size, had smaller linear density of bridged chains (optical micrograph in Figure 6.2(c)) as well as less surface area covered with assembly electrodes. The contradiction can be explained by the effect of capillary force during alcohol evaporation. NW chains which detached and agglomerated during alcohol evaporation decrease the light transmittance. Increasing the electric field by increasing the applied voltage could likely offset the disruptive effect of capillary force and prevents the formation of the NW clumps.

By increasing the applied voltage, as explained in the previous chapter, more NWs need to be provided to create sufficient amount of chains bridging the electrodes. This can also decrease the light transmittance but this time because of an increase in linear density of bridged NWs.

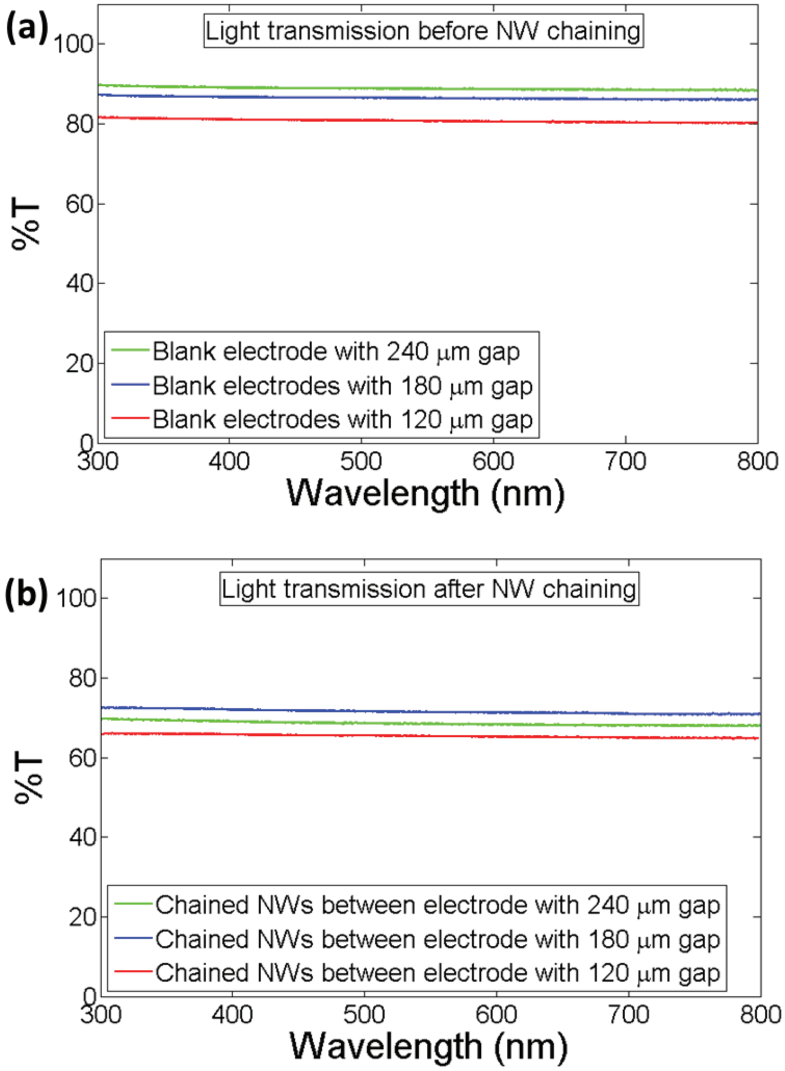

Figure 6.3: Light transmission results from substrate patterned (a) with blank electrodes with gap sizes of 240 μm, 180 and 120 μm and (b) with NW chains between different electrode gap sizes. NW chain assembly occurred at 10 kHz and 5 V (rms).

Figures 6.2 and 6.3 showed that a chaining configuration without NW-clumping can provide better light transmittance. However, although NW clumps do not appear on the substrate with 120 μm assembly-electrode gap size, high surface area covered with assembly electrodes decreases the light transmittance of this substrate. As mentioned, Au electrodes used in this experiment have 100 nm thickness and therefore, zero light transmittance. How much will the light transmittance improve by using a thinner layer of assembly electrodes?

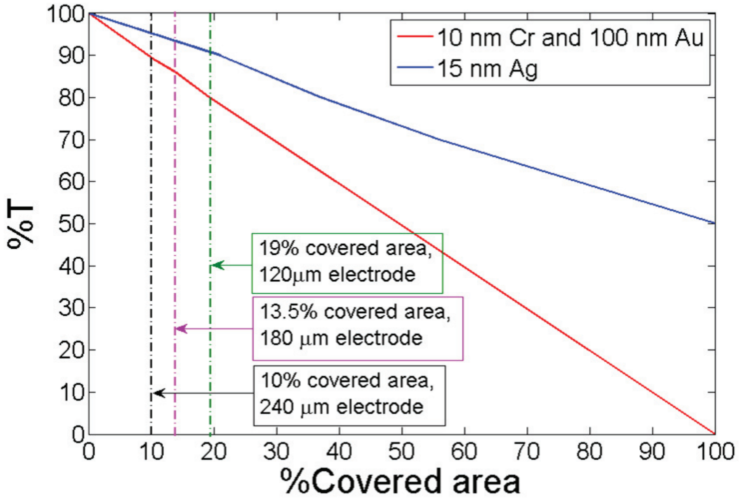

Figure 6.4: The effect of assembly-electrode thickness on light transmittance of the substrate. Transmittance measurement for glass substrate coated with 15 nm Ag layer (blue line), is taken from Ref. [104]. Electrodes with 10 nm Cr/100 nm Au layer (red line) were used in this work. Vertical dashed lines represent the percent of covered area for assembly electrodes with 120, 180 and 240 μm gap size.

A recently published paper by Theuring *et al.* [104], used a 15 nm-thick Ag layer patterned with circular shapes in different sizes. They measured the change in light transmittance of the substrate with different surface coverage. To quantify the effect of using thinner electrodes, the plot shown in Figure 6.4 can be used to compare the change in the light transmittance with covered area for electrodes fabricated from 10 nm Cr/100 nm Au (used in this research work) and electrodes with 15 nm thick Ag (from Theuring's work [104]).

Figure 6.4 shows that by using 15 nm Ag instead of 100 nm Au, light transmittance of blank electrodes with 240, 180 and 120 μm gap size increases by 7, 10 and 12% respectively. Accordingly, if 15 nm Ag was used to fabricate interdigitated electrodes, the light transmittance of resulting TE (after NW chaining) could increase as shown in Table 6.1.

Although thinner assembly electrodes have higher light transmittance, they have lower sheet resistance. A uniform metallic film of thickness t and metal resistivity ρ has a sheet resistance $R_s = \rho/t$ expressed in units of Ω/sq. A nanostructured

Table 6.1: Effect of assembly-electrode thickness, for geometry used in our experiments, on light transmission (%T) of the resulting transparent electrode (TE).

Gap size (μm)	%T of TE, 100 nm Au	%T of TE, 15 nm Ag	% increase in T
120	65	77	15.6
180	72	82	12.2
240	69	76	9.2

metallic film with a 1D spacing x, width w, and thickness t has a sheet resistance of $R_s = (\rho/t)(x/w)$ [59,109].

Considering two grid substrates as shown in Figure 6.5 one patterned with 100 nm-thick Au and the other one with 15 nm-thick Ag. Electrical resistivity of Au and Ag at 20°C are 2.4×10^{-8} and 1.6×10^{-8} Ωm respectively [110]. If in both cases, w=30 μm and x=180 μm, the resulting sheet resistance would be 1.4 and 6.4 Ω/sq for 100 nm Au and 15 nm Ag respectively. It shows that as a result of using 15 nm Ag electrodes instead of 100 nm Au electrodes, the increase in light transmittance (shown in Table 6.1) is smaller than the increase in sheet resistance (78.1%) of the substrate.

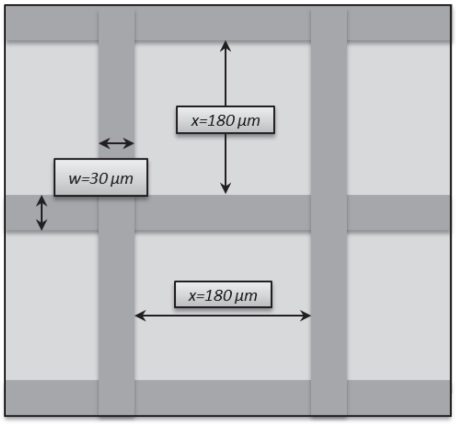

Figure 6.5: Schematics of thin film grid pattern.

Chains of 250 nm diameter Rh NWs between assembly electrodes of 100 nm thick Au showed the highest light transmittance (72%) when assembly-electrode gap size was 180 μm. No study was found on using electric field assisted chaining of NWs for fabrication of TEs due to difficulties in generating multiple long chains to cover large surface area. However, controlling the forces and parameters that are involved in NW chaining by using field-generated forces enables fabrication of TEs from any metallic or semiconductor materials on a large surface area with low cost. In this work, Rh NWs were used to demonstrate the capability of this method, however, less expensive materials such as copper can be used for further studies.

6.4 Conclusions

Low cost attributed to the material and fabrication process is an essential requirement for device manufacturing. One approach to meet this requirement is demonstrated in this work. NW chains between patterned thin-film assembly electrodes were utilized to demonstrate a technique for transparent electrode fabrication. The main benefit of this method compared with other low cost methods such as NW spray or drop casting is that NW connectivity and chain configuration can be controlled by field-generated forces. Compared with TEs fabricated by using patterned thin metal film, here a small fraction of surface area is covered with thin film assembly-electrodes and therefore, the light transmittance of the resulting TE is less sensitive to the thickness of metallic electrodes. The method introduced here is applicable for both organic and inorganic substrates as no high temperature or corrosive environment were involved during the fabrication. In general, simplicity and a wide range of applicable materials, make this technique favorable for versatile low cost fabrication of large-area TEs.

6.5 Future Work

A four-point probe sheet resistance device was required for measuring the sheet resistance of the different substrates with different chain configuration. However, at this phase of the study, this device was not available to us. The results of this study can be used for further investigation on finding best parameter values for high performance TE.

Chapter 7

NW Chaining on Flexible Substrate

This chapter describes NW chaining on flexible substrates using electric field-generated forces. In this method, after patterning assembly electrodes on a rigid substrate using photolithography, a polymer is spun and baked on the substrate. AC electric field is applied to the electrodes patterned on the substrate and simultaneously off-chip synthesized NWs are introduced over the baked polymer. Field-generated forces (DEP and Coulomb forces) enable NW chaining on the entire surface of the polymer. Other layers can be deposited on the NW-patterned polymer to generate a functional device such as organic solar cells. Finally, the polymer can be peeled from the rigid substrate without destroying NW chain connectivity and configuration. To the best of author's knowledge, using electric field-generated forces to create NW chains on a flexible substrate has been developed for the first time in this research work .

7.1 Two Protocols

As shown in chapters 5 and 6, field-generated forces enable the creation of NW networks on a rigid substrate that can be used for fabrication of transparent electrodes. Due to increasing demands on electronic devices that are flexible, foldable or even wearable, combining flexibility, light weight, high electrical conductivity and optical transparency is essential for the development of many devices. Examples of the devices are flexible displays, electronic textile, sensory skins and organic solar cells [111–114]. Reliable, simple and cost-effective assembly techniques that provide large area coverage on flexible substrates have received increasing attention in last couple of decades. Knowing that field-generated forces are capable of providing uniform coverage of NWs over a large area at low cost, made it worth investigating the capability of field-generated forces for positioning NWs on flexible substrates. To achieve this, two primary protocols were considered. Each protocol and its preliminary considerations are explained below:

1. Thin film electrodes patterned on top of a flexible substrate:

In this approach, thin-film assembly electrodes are patterned on a polymer substrate. Having an organic substrate, it is necessary to avoid patterning techniques that require corrosive environments. Shadow masks (metal masks with micron-size patterns) enable transfer of the patterns to the polymer substrate by using physical vapor deposition (PVD) or sputtering tools. In this method, the stability of the polymer substrate at the deposition temperature needs to be taken into account. Also, the deposited metal film needs to be thin to withstand a high level of bending without being cracked. Crack formation due to bending strain can degrade properties such as electrical conductivity. Followed by patterning the assembly electrodes, electric field can be applied on the substrate by using the probe tips, as shown in Figure 7.1(a). NW assembly will then occur in between electrodes when NW suspension is introduced on the substrate.

2. Baked-polymer layer over electrodes patterned on a rigid substrate:

A rigid substrate is patterned with the desired electrode geometry using conventional fabrication techniques such as photolithography and lift-off. A layer of polymer is spun and baked on the substrate. The polymer is partially removed from electrodes on which probe tips make contact to apply electric field (see Figure 7.1(b)). Following this, NW suspension is introduced on to baked polymer. The applied electric field polarizes NWs in the suspension enabling NW assembly on the polymer surface. After NW assembly, the polymer, including positioned NWs, can be peeled and attached to a desired surface. The polymer should be thick enough for it to be peeled without rupture and deformation during peeling should be elastic, to maintain dimensional stability within desired tolerance. In this approach, the patterned rigid substrate is reusable for unlimited NW assembly experiments.

In both protocols introduced above, the flexible substrate should not be chemically reactive with the medium of NW suspension (*e.g.* ethanol in this work). Having

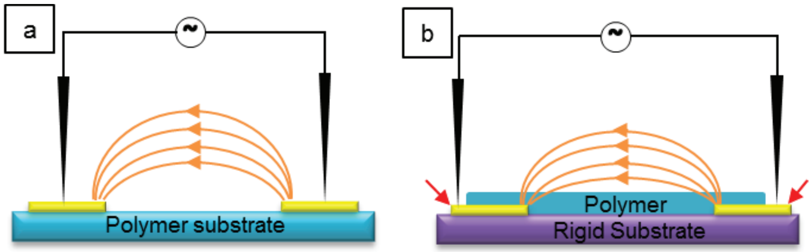

Figure 7.1: Two different protocols for NW assembly on a flexible substrate using field-generated forces. (a) NW assembly on a patterned plastic substrate (b) NW assembly on a polymer layer coated on a patterned rigid substrate. Polymer is partially removed from the electrodes (see red arrows) enabling electrical contact.

a reusable patterned wafer that enables NW positioning on a polymeric substrate without the requirement of depositing metal film directly on the flexible substrate make the second approach more reliable. Therefore, in this work, NW chain assembly by field-generated forces on flexible substrates is investigated using a baked polymer on a patterned rigid substrate.

7.2 Experiments

Polyimide (VTEC 1388) was used as a flexible substrate in this research work. Polyimide represents an important class of high temperature and solvent resist polymers. Stability under mechanical stress and wide temperature range make polyimide a good candidate for several devices such as solar cells [115] and humidity sensors [116].

Creating of a NW chain network on the polymer substrate consists of three steps: Spin coating the polymer on a patterned substrate, assembly of NW chains on the polymer layer, and peeling off the NW-patterned polymer. Each step requires several considerations as noted below.

7.2.1 Spin Coating

A 4-inch silicon wafer with 300 nm thermally-grown silicon oxide was used. 100 nm-thick interdigitated electrodes were patterned by using a lift-off process (Appendix A). Polyimide was spin-coated on the patterned silicon wafer. Spin speed and spin time were 3500 RPM and 70 seconds respectively. Polyimide was then baked at 90°C for 90 seconds followed by 150°C for another 90 seconds. The thickness of the baked polymer was measured as 8 μm by using a Bruker profilometer model DekTak XT.

The thickness can be altered by tuning the spin speed. In order to achieve a uniform thickness, spin time needs to be increased for lower spin speeds. Before spin coating step, careful cleaning of the substrate with acetone and isopropanol was required for removing the contamination from substrates followed by nitrogen-gas drying. The substrates were then dehydrated on a hotplate at 110°C for 1 minute and cooled down in air before spin coating the polymer.

In the presence of surface contamination, thickness of the polymer becomes nonuniform. Light fringes, shown in Figure 7.2 (a), are the evidence of nonuniform thickness which results in nonuniform NW assembly (see Figure 7.2 (b) and (c)).

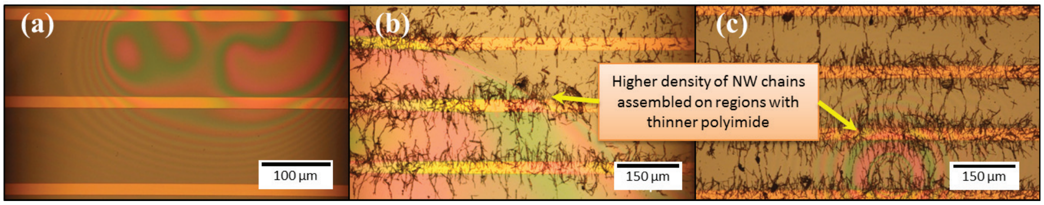

Figure 7.2: (a) Nonuniform thickness of polymer. (b) and (c) show that more NW chains are generated over thinner parts of polyimide layer.

7.2.2 NW Assembly

NW chaining facilities used were the same as used for rigid substrates in Chapter 5 and 6. An AC voltage was applied across the interdigitated electrodes and NW suspension was introduced on to the baked polymer layer. Determination of the frequency and voltage value is discussed later. After micro-pipetting enough volume of the NW suspension over the surface of the baked polyimide, NW chaining occurred throughout the substrate. The dam with parallel wells, that was used for NW chaining on rigid substrates, was also used here but for a different reason. In this case, due to the presence of polyimide layer, the electrical short circuit cannot happen after NW chains bridge the electrodes. However, since the polyimide layer can behave as a capacitor, the electric field will be small inside the NW suspension which results in small values for field-generated forces. As explained in Chapter 5, the capillary force could be more disruptive in the absence of a strong electric field. The dam, in this case, moderates the motion of the alcohol drying front and prevents chain destruction due to drag force at the drying front. After alcohol dried out completely, the dam was carefully removed from the substrate by using a tweezer and the chain configuration was recorded using an optical microscope and digital camera. The AC voltage was left on during the entire NW assembly process.

7.2.3 Peeling

After NW assembly, NW-patterned polyimide was peeled from the substrate. To do so, one edge of the baked polyimide was gently detached from the substrate. The peeled edge of the polymer was then grasped by a tweezer and the rest of the polymer was mechanically peeled from the substrate as shown in Figure 7.3(a).

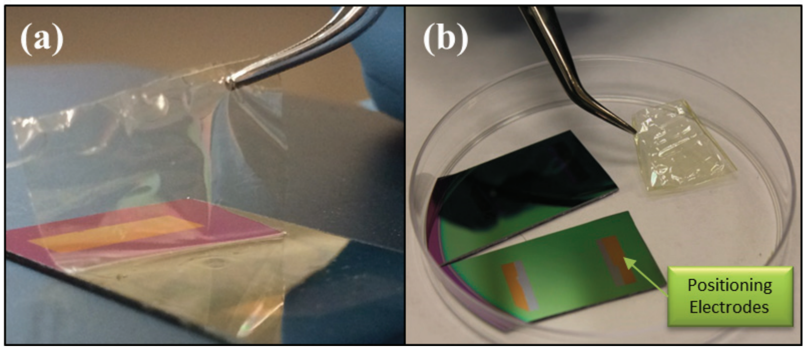

Figure 7.3: (a) Peeling NW-patterned polymer from a rigid substrate. (b) SiO_2 layer was deposited on the substrate to assist peeling the NW-patterned polymer. Oxide layer was partially etched from positioning electrodes to enable electrical connection between probe tips and electrodes.

It was observed that polyimide adheres strongly to the surface of Au electrodes but it peels easily from non-patterned region of the substrate. This behavior could cause polymer rupture during the peeling step. To prevent this, after patterning interdigitated electrodes and before spin coating the polymer, 100 nm of SiO_2 was deposited on the substrate using plasma-enhanced chemical vapor deposition (PECVD) using a NEXX Systems model Cirrus 150 ECR PECVD. To remove oxide layer from the positioning electrodes, substrate was covered with AZ703 photoresist and positioning electrodes were then exposed using photolithography as explained in Appendix G. Following that, reactive ion etch (RIE) (Sentech model Etchlab 200) was used to remove the oxide layer from positioning electrode as shown in Figure 7.3(b). To Peel the NW-patterned polymide, two cuts were made through the polyimide, by using a surgical blade, to isolate polymer from two assembly electrodes. This prevents polyimide rupture due to adhesion of polymer to the Au assembly electrodes.

7.3 Assembly Parameters

We have examined several experimental conditions for chaining NWs on the polyimide layer. NW concentration was kept the same as that used for NW chaining on rigid substrates (3.3× 10^8 NW/mL). The maximum voltage available with the function generator (V_{rms}=7 V) was applied to the substrate. In addition to the magnitude of the applied voltage, its frequency also affects chain formation. Figure 7.4 shows that for similar applied voltage, chains start to grow from the assembly electrodes at 100 kHz (Figure 7.4(a)) but no evidence of NW chaining was observe at 10 kHz (Figure 7.4(b)). What prevents NW chaining at 10 kHz?

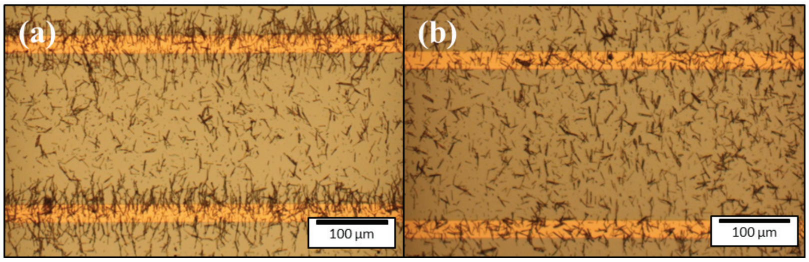

Figure 7.4: Effect of frequency on chain formation: (a) 100 kHz, (b) 10 kHz. In both cases, electrode-assembly gap size is 240 μm.

The variation in NW-chain formation with applied frequency can be related to the capacitive behavior of polyimide. A published review paper [117] about different polymers coated on conductive films showed that polymers can behave as a capacitor. Accordingly, at low frequencies, polyimide layer has the ability to store charges or act as a capacitance. Further details about the behavior of the polymer layer in the presence of electric field will be taken up in detail, in future work.

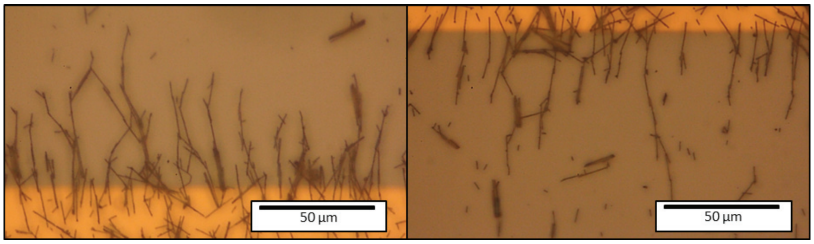

Figure 7.5: Chain growth at 7 V (rms) and 100 kHz between electrodes with 240 μm spacing. NW chains remain short due to small field-generated forces.

Although chain growth was observed at 100 kHz, shown in Figure 7.5, bridging did not occur for 240 μm assembly-electrode gap size due to the weak field-generated

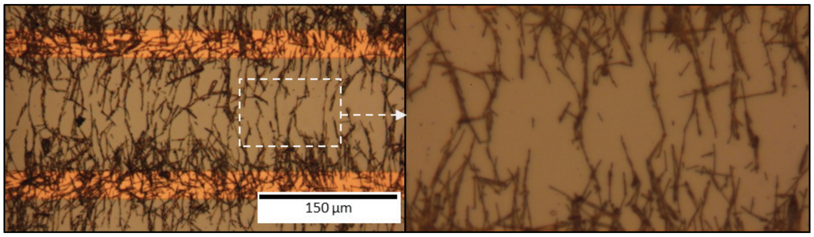

Figure 7.6: NW chain bridging electrodes with 120 μm gap size. Assembly voltage and frequency used were 7 V (rms) and 100 kHz respectively.

forces. Therefore, smaller electrode gap size (120 μm) was used to enhance the magnitude of electric field. The result of NW chaining is illustrated in Figure 7.6.

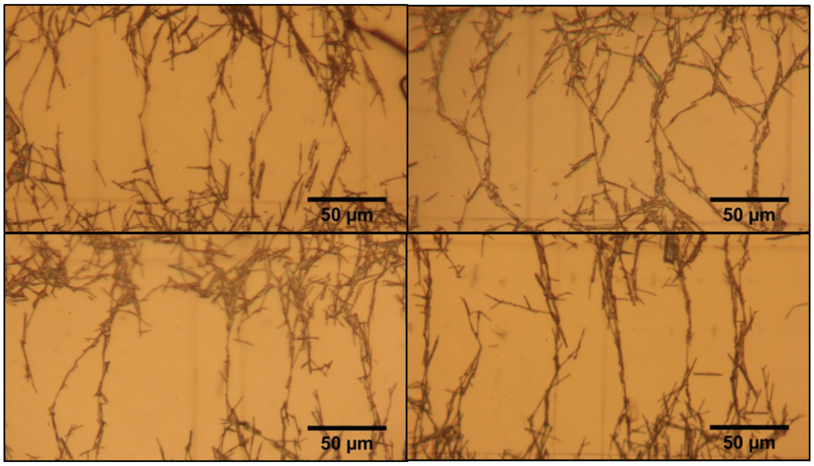

Figure 7.7: Peeled NW-patterned polyimide. High van der Waals force between NWs and polymer prevents chain destruction during peeling of the polymer.

The NW-patterned polyimide was then peeled and NW chain structure was observed using an optical microscope. Optical micrographs such as in Figure 7.7 demonstrate that peeling the polyimide, does not affect the NW chain configuration.

The NW-patterned polyimide can serve as a charge collector with high conductance in the direction of NW chains. To provide a better performance as a charge collecting layer, a polymer layer with multi-directional (isotropic in-plane) conductivity is required.

7.4 Fabrication of NW Grid

The field direction dictates the orientation of NW chains. Accordingly, it is possible to modify the pattern of NW chain by fabricating assembly electrodes in different shapes. In this section, a grid-shaped NW chain is demonstrated. To achieve this, a rectangular-shaped assembly electrode was fabricated from two layers of interdigitated electrodes that are perpendicular with respect to each other but electrically isolated by an intermediate layer of dielectric (see Figure 7.8). A detailed sequence of fabrication steps is provided in Appendix G. Briefly, horizontal assembly electrodes that are connected to vertical positioning electrodes were first patterned on a Si/SiO_2 substrate by photolithography and lift-off process. Following this, 300 nm of SiO_2 was deposited on the first patterned layer by using PECVD. To increase the adhesion of oxide layer to Au-electrodes, 10 nm Ti was deposited on Au electrode during lift-off process. A second layer of assembly electrodes (vertical assembly electrodes connected to horizontal positioning electrodes) was metallized on the oxide layer using the same photolithography and lift-off process followed by deposition of a 100 nm oxide layer to prevent adhesion of polyimide to Au electrodes as described in Section 7.2.3. Finally, the oxide layer was removed from the positioning electrode by using RIE. The PECVD oxide layer between horizontal and vertical interdigitated electrodes prevents electrical short circuit between two layers of assembly electrodes during NW chaining.

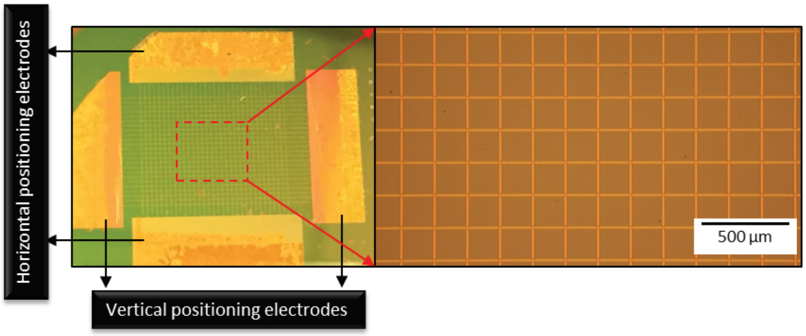

Figure 7.8: Grid-shaped assembly electrode detailed at right of figure.

To create NW grids, chain formation at each electrode layer was conducted separately as shown in Figure 7.9. In Figure 7.9(a) 80 μL of NW suspension was introduced to the dam when AC voltage was applied only to vertical positioning electrodes. After alcohol dried out, probe tips were connected to horizontal positioning electrodes to apply AC electric field between vertical assembly electrodes, the dam was rotated 90 degrees and another 80 μL of NW suspension was added (Figure 7.9(b)). These steps can be repeated as many times as needed to create high enough density of NW grids on the polymer.

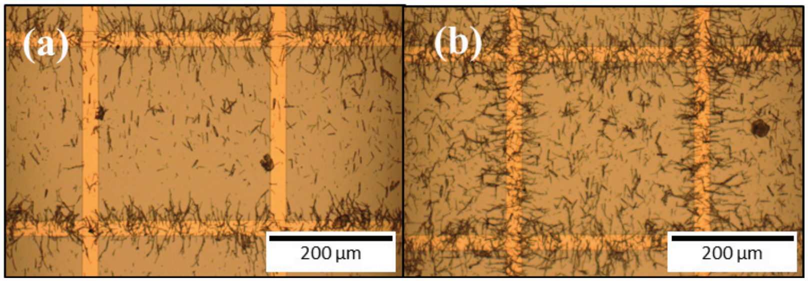

Figure 7.9: Alternating applied voltage to (a) horizontal, (b) vertical assembly electrodes.

A different amount of NW suspension is required for different assembly-electrode spacing. While 80 μL of NW suspension was sufficient to create NW grids by using 120 μm electrode spacing (Figure 7.10(a)), 180 μL of NW suspension was used in the case of 300 μm electrode spacing (Figure 7.10(b)). Figure 7.10 also shows that smaller assembly-electrode gap size provides more ordered NW-grid pattern while in higher gap size, the pattern is less ordered as it shown in Figure 7.10(c). This is due to smaller field-generated forces between assembly electrodes with larger gap size.

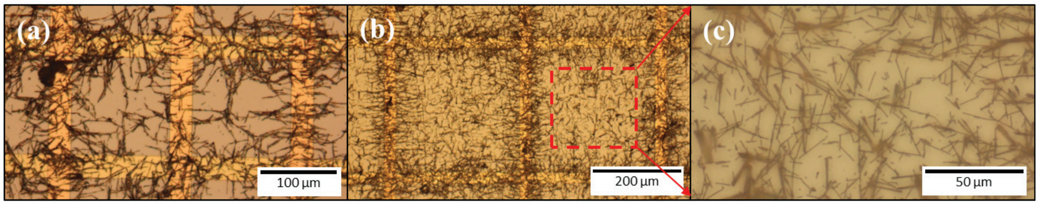

Figure 7.10: NW grid formation. (a) 120 μm and (b) 300 μm electrode spacing. Smaller field-generated forces in (b) caused less ordered patterns of connected NWs showed in (c).

In this chapter, a new protocol for positioning NWs on a flexible substrate was demonstrated. Applying electric field on a patterned rigid substrate causes NW chaining on a spun and baked polymer on the substrate. Compared with the case of creating NW chains directly on a rigid substrate, electric field and resulting field-generated forces are smaller here due to the presence of the polymer layer. To increase the electric field where choosing higher voltage is not possible, decreasing the assembly-electrode gap size is recommended. The frequency needs to be high enough to overcome the capacitive resistance of the polymer layer.

7.5 Conclusions

In this chapter, we introduced a new technique for NW assembly on a flexible substrate by using field-generated forces. Two different approaches were noted: (1) depositing assembly electrode on a plastic substrate and chaining NWs between assembly electrodes, (2) NW chaining on a spun polymer on a patterned-rigid substrate. In (1), patterning of the assembly electrode and NW positioning both occur on the polymer substrate whereas in (2), electrodes are patterned on the rigid substrate while NW assembly occurs over the baked polymer. The second approach was pursued in this chapter due to several reasons. In the first protocol, cracks may initiate in the thin film electrodes deposited on flexible substrates and degrade the property of the resulting device. Also the patterning technique may limit the choice of the substrate material if a high temperature or corrosive environment is required for patterning the assembly electrodes. In contrast, in the second approach, assembly electrodes are not patterned on the flexible substrate, accordingly, neither property degradation due to crack propagation in assembly electrodes, nor high temperature or corrosive environment involved in the assembly-electrodes patterning, cause any limitation. In addition, having assembly electrodes patterned on a rigid substrate allow the substrate to be used repeatedly. In the first protocol, in which patterning step on the polymer substrate needs to be repeated for every experiment.

However, the main difficulty of patterning NWs on a spun polymer is the low electric field strength due to the presence of a thick polymer layer. To overcome this difficulty, one approach is to design assembly electrodes with small gap sizes that can generate a higher electric field strength.

In this work, 120 μm assembly-electrode spacing was the smallest gap size that could be used for NW chaining on an 8 μm-thick at 7 V (rms) and 100 kHz. Maximum available voltage was used to increase field-generated forces while 100 kHz was found to be a suitable frequency for NW chaining. Peeling the NW-patterned polyimide after the chaining process did not destroy the chain configuration since NWs are strongly adhered to the polymer surface.

The utility of different assembly electrode patterns was introduced to create multi-directional chain configuration with the idea of enabling more uniform electrical conductivity throughout the resulting flexible substrate. Grid-shaped electrodes were used to create a NW grid on an 8 μm-thick polyimide substrate. This NW chain configuration creates electrical conductivity in both horizontal and vertical direction which is important for flexible electrodes in applications such as solar cells. Because of the simplicity and low cost of fabrication, the proposed technique will have an impact in a wide range of applications including photovoltaic cells and displays.

7.6 Future Work

The photolithography patterning was carried out at Simon Fraser University, as the required tools and clean room facility were not available at UVic. Restrictions in the availability of equipment, costly trips and user charges, and many other practical limitations slowed down the development and production of substrates which needed a range of electrode spacing. Moreover, equipment to measure the electrical property (sheet resistance) of the chained NWs on the flexible substrate was not available either at UVic or at Simon Fraser University.

However, this study was a proof-of-concept for positioning NWs on a flexible substrate by using electric field-generated forces. The systematic study of NW chaining conditions (mainly: applied frequency, voltage, assembly-electrode gap, as well as utilizing a dam to reduce disruptive effect of capillary force at the NW suspension drying front) pave the way for future further development in this area. An equipped microfabrication facility is expected to become available at UVic in a time scale of one year. This will significantly boost the production rate of the substrate with different assembly-electrode geometry.

Additionally, one interesting question to explore is the effect of polymer conductivity on NW chain configuration. The electric field inside the NW suspension will be stronger when the resistivity of the polymeric substrate is low. Besides more control over NW-chain configuration, using a polymer with low electrical resistance may allow using a thicker layer of a polymer as the flexible substrate which should allow easier peeling and handling of the resulting device.

Chapter 8

Conclusions

This dissertation presents experimental research supported by analysis, to create a systematic framework applicable to any field-directed assembly method for positioning NWs at predetermined locations on a substrate. The technique enabled positioning and clamping of single NWs to create nanoresonator arrays, combining AC electric-field assisted assembly of NWs, photolithographic patterning and electrodeposition. This assembly method is general and can be extended to many other types of off-chip synthesized materials, polarizable in a medium. This is a cost-effective method, in that fabrication cost does not scale with the size of the substrate or the number of devices on the substrate. However, achieving high device yield is challenging due to the presence of disruptive forces and physical parameters, which have until now been resolved chiefly by time-consuming trial-and-error, with little guidance from analysis and computation.

In creating a process to achieve a high yield of single-NW resonators, chaining of NWs was a disruptor. However, chaining is an inherent phenomenon in electric field-directed NW positioning and can be utilized where NW connectivity is needed, as in charge collector layers or transparent electrodes. Although different fabrication methods have been studied to generate networks of NWs, an easy, cost-effective technique that controls configuration of NW networks over large surface area still needed to be discovered. Field-generated forces were demonstrated here, for the first time, as a technique to produce transparent conductive surfaces.

The main contributions of this dissertation, with consideration of their applications, are listed below.

1. Introduction of a director-disruptor framework for experiments in field-directed

assembly, with the following steps: identification of forces serving as assembly directors and disruptors; analysis to separate disruptors weakly-coupled and strongly-coupled to the director; experimental reduction or elimination of weakly-coupled disruptors; and analysis for defining dimensionless parameters that more compactly describe the parameter space. This rational alternative to costly trial-and-error in the search for parameter values opens a path to nanomanufacturing, with strong potential to enable widespread commercial and scientific use of nanodevices. Our published demonstration of the highest field-directed assembly yield achieved with a single director to date, also provides some validation of the utility of this framework.

2. Customizing fabrication for the creation of nanomechanical resonator platforms, towards biosensors for multiplexed, cost-effective molecular diagnosis.

3. Publication of a method to achieve the first experimental realization of multiple long chains of NWs, without shorting the electrodes. Achieving a balance between dielectrophoretic force and dipole-dipole interaction forces was realized experimentally, allowing multiple suspended chains above the electrodes, to be trapped by the drying suspension medium. The result is a significant step towards the production of reduced-cost transparent electrodes (TEs) for photovoltaics and displays. Using this protocol, fabrication of transparent electrodes was demonstrated on glass substrates. Optical transmissivity of the resulting electrodes was characterized by experiments.

4. Experimental studies for fabrication of transparent conductive electrodes on rigid and flexible substrates, tuned for particular applications of TEs. Due to high demand for comfortable, foldable and light-weight devices, a new generation of electronics, displays, biological sensors and photovoltaics need to be made on flexible substrates. Incompatibility of plastic substrates with corrosive or high temperature environments imposes challenges in fabricating these devices. In Chapter 7, two protocols were introduced which enable chain formation by using field-generated forces, on flexible substrate. Choosing one of the protocols, NW chains on polymeric substrate were demonstrated as a proof-of-principle.

This research work has introduced a new approach in using field directed assembly of NWs by first, providing a framework that helps increase the device yield in shorter time and with lower cost compared to a trial-and-error approach, and second, by introducing a cost-effective technique that enables fabrication of NW networks on both rigid and flexible substrates. The forces and parameters that influence both single and chained NW assembly were discussed. This work can pave the way for fabrication of nanodevices and move towards nanomanufacturing and commercialization of the devices. Opportunities for future work have been included at the end of each thesis chapter.

Appendix A

Lift-Off Process

Pick 4” Si wafer with 300nm SiO_2
Clean sample with acetone and IPA
Dehydrate sample 1 min at 110°C followed by 2 min cool down in atmosphere temperature
Spin LOR-A at 4000 RPM for 40 sec
Prebake wafer with LOR-A for 2 min at 180°C
Spin coat 1 μm AZ703 photoresist at 4500 RPM for 40 sec
Prebake sample for 1 min at 90°C followed by 1 min cool down in atmosphere temperature
Second stage of prebake 1 min at 110°C followed by 2 min cool down in atmosphere temperature
Expose AZ703 with Mask 1 (”electrode”) for 4 sec
Develop AZ703 in developer MIF 300 for 55 sec
Oxygen descum
Load sample into evaporator
Evaporate desire metal
Soak sample in Microposit remover 1165 for 24 hours at room temperature
Sonicate Micro 1165 remover if necessary
Rinse in DI water
Rinse in IPA
Dry sample with Nitrogen

Appendix B

Nanoresonator Integration Process

Pick 4” Si wafer with patterned electrodes prepared by metal lift-off procedure in appendix A
Clean sample with acetone and IPA
Dehydrate sample 1 min at 110°C followed by 2 min cool down in atmosphere temperature
Spin PMGI SF-11 at 4000 RPM for 40 sec
Bake PMGI SF-11 on hotplate at 200°C for 5 min followed by 5 min cool down at room temperature
Spin Shipley 1811 at 4000 RPM for 40 sec
Bake on hotplate at 100°C for 1 min
Align Mask 2 (”wells”) and expose Shipley 1811 for 4 Sec with power of 19.4 mW/cm^2
Develop Shipley 1811 in developer MF 26-A for 45 sec
Oxygen descum at 25 W for 30 sec
Check exposed feature with optical microscope
Expose PMGI SF-11 in the Hitachi zoon SEM for 90 sec
Develop PMGI SF-11 in 101A developer for 40 sec
Soak sample in acetone for 2 min and rinse sample in acetone and IPA
Assemble nanowires from ethanol suspension using AC bias with 100 KHz and 7 V$_{rms}$
Check nanowire alignment result with optical microscope
Rinse sample in IPA
Dehydrate sample 1 min at 110°C

Spin Shipley 1811 at 4000 RPM for 40 sec
Bake on hotplate at 100°C for 1 min
Align Mask 3 (”clamp”) and expose Shipley 1811 for 4 sec with power of 19.4 mw/cm^2
Develop Shipley 1811 in developer MF 26-A for 40 seconds
Oxygen descum at 25 W for 30 sec
Check exposed feature with optical microscope
Expose PMGI SF-11 in Hitachi zone cleaner for 240 sec
Develop PMGI SF-11 in 101A developer for 45 sec
Check exposed feature with optical microscope
Pre-heat Ag electrolyte (commercially available succinimide $Ag(C_4H_5NO_2)_2$ silver solution) to 55° with water bath followed by magnetic stirring Ag electrolyte
Plate Ag using galvanostatic deposition at current densities ranging 0.3×10^{-2} to 3.3×10^{-2} mA/cm^2 for 4 hours
Soak sample in Micro 1165 remover at 55°C for 8 hours
Soak sample in DI water and gently stir for 30 sec
Remove sample and soak in fresh DI water and gently stir for 30 sec, repeat this step for 4 times
Soak sample in ethanol and gently stir for 30 sec
Remove sample and soak in fresh ethanol and gently stir for 30 sec, repeat this step for 4 times
Transfer sample to a 100 ml reservoir filled with ethanol
Use critical point drier to dry sample out of ethanol

Appendix C

Rhodium Nanowire Length

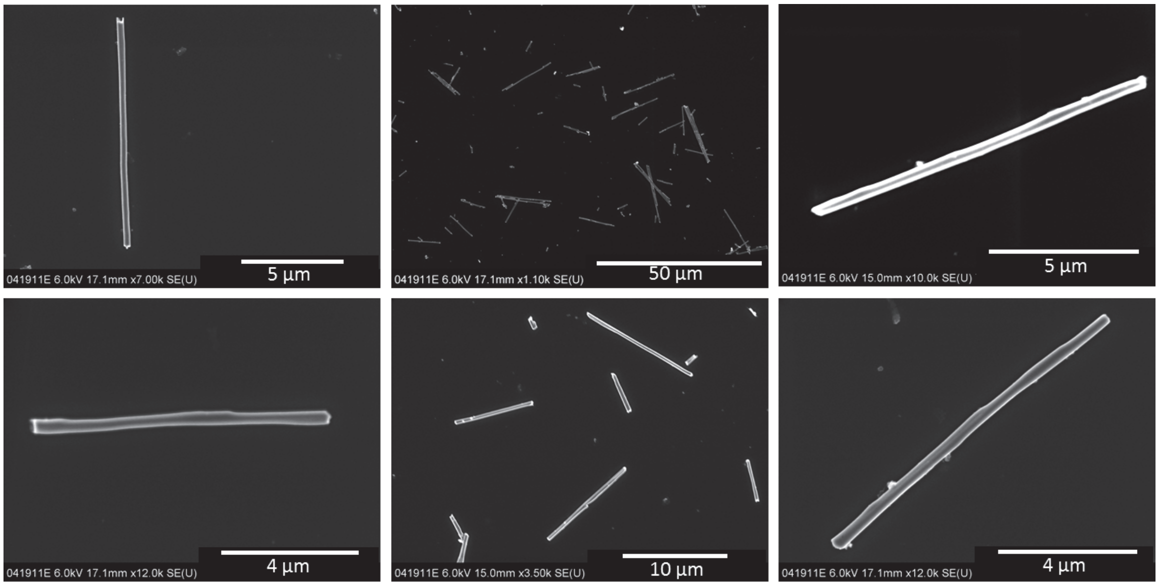

Figure C.1: SEM images of the rhodium nanowires extracted from anodized alumina membranes (AAO from Whatman). Dominant length ranged between 8 to 12 μm.

Appendix D

Single Nanowire Positioning

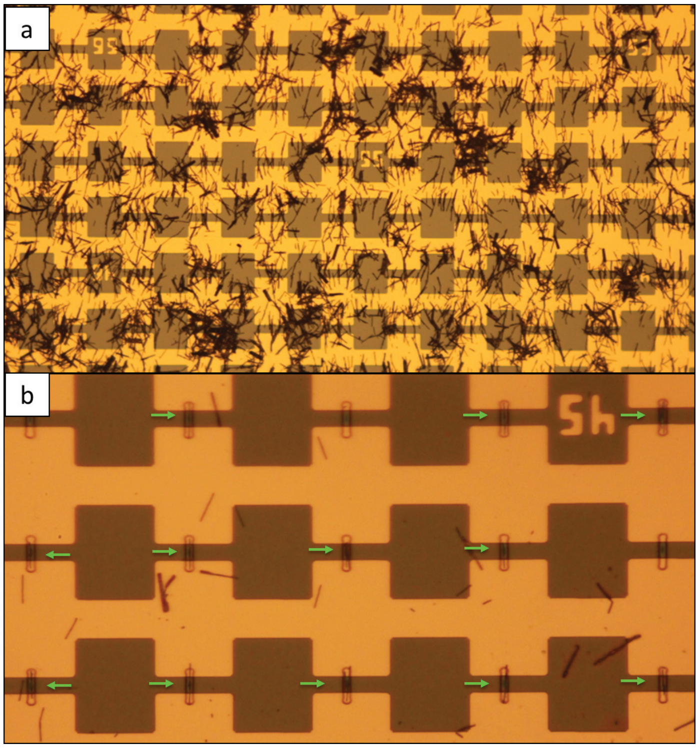

Figure D.1: Effect of NW concentration on NW assembly yield: (a) high concentration of NWs reduces the device yield due to presence of so many NW clumps on the substrate. (b) decreasing the concentration to $19{\times}10^5$ NW/mL increases the number of wells filled with single NWs (green arrows).

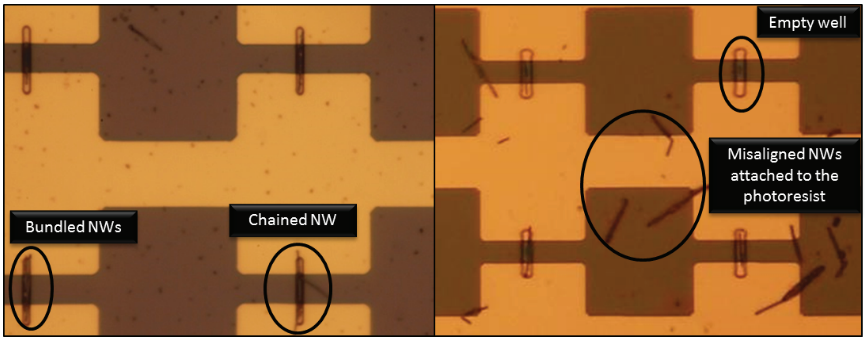

Figure D.2: Optical micrograph of nanowire assembly defects. Nanowires are preferentially positioned inside wells. Defects such as bundled, chained and empty sites are considerably reduced by appropriate choice of nanowire concentration range. Misaligned nanowires, shown attached to the photoresist surface, are removed with the photoresist.

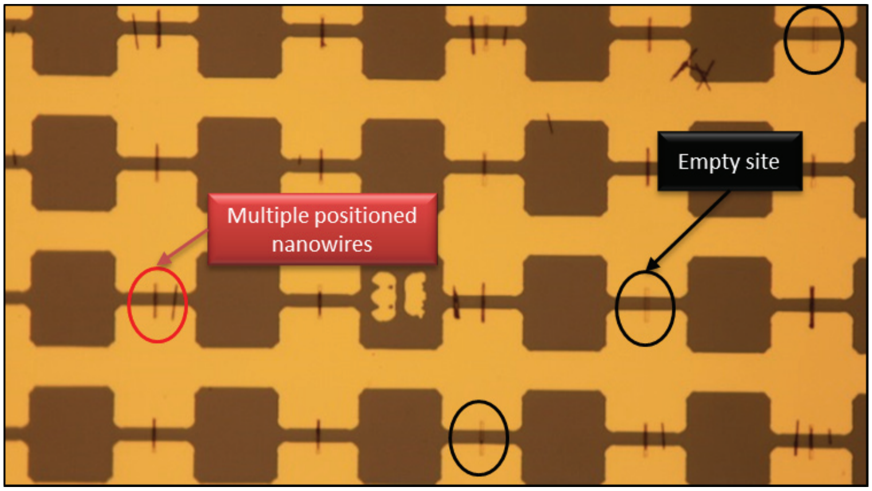

Figure D.3: High pre-clamped yield of nanowires. Where multiple nanowires are positioned in between some electrode pairs, only one nanowire per electrode pair is counted, to determine the assembly (pre-clamped) yield.

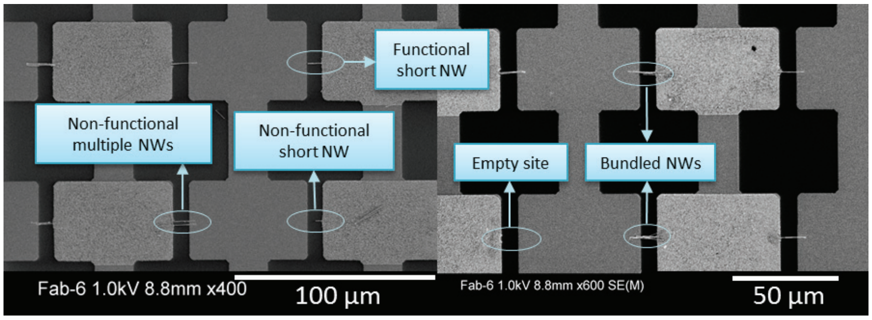

Figure D.4: SEM image of post-clamped defects. Empty sites, bundled or multiple nanowires less than 10 μm apart and short nanowires were not counted as functional nanoresonators. If the free end of a clamped nanowire reaches the edge of the counter electrode below, it is counted as functional device.

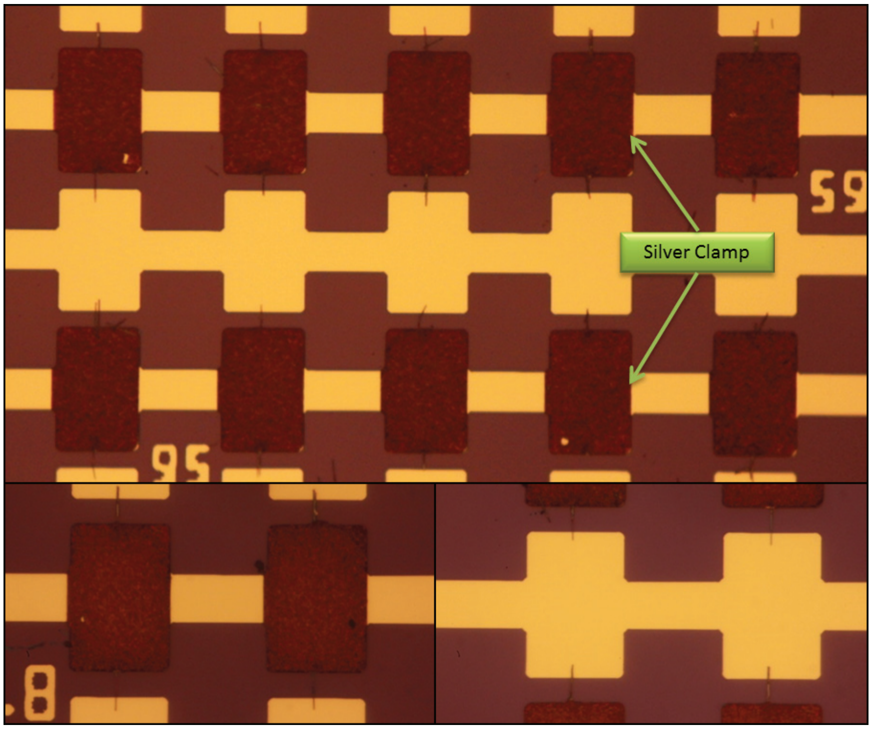

Figure D.5: Optical image of clamped nanowires showing high yield after photoresist removal. Dark rectangles are the silver clamps.

D.1 Order of magnitude analysis of Brownian and dielectrophoretic displacement

Scaling analysis -Brownian and dielectrophoretic displacement: Under the action of viscous drag force (F_d), given in Eq. (D.1), terminal velocity u is achieved when viscous drag force F_d opposing the motion becomes equal to applied DEP force F_{DEP}.

$$F_d = 4u\pi\eta L/[ln(2L/d) + 0.5] \tag{D.1}$$

For a NW of mass m, the acceleration changes from $a = F_{DEP}/m = F_d/m$ to zero, as the velocity increases from zero to u. For a rough estimate of time scale,

$$\tau \cong \frac{u}{a} = \frac{\rho_p d^2}{16\eta}[ln(2L/d) + 0.5] \tag{D.2}$$

For a rhodium NW with density ρ_p=12,410 Kg/m^3, L=10 μm, d=0.25 μm and ethanol dynamic viscosity η=1.2×10^{-3} kg/m.s, we calculate τ to be 1.2×10^{-7} s. Comparing this time to observation time t ∼1 s, the moving NW is almost always at terminal velocity. Using the relation for Brownian displacement with the Stokes-Einstein relation for particle diffusivity yields [68] $\Delta X_{Br} = (2k_BTt/\gamma)^{1/2}$. The displacement due to DEP force is $\Delta X_{DEP} = ut = (F/\gamma)t$. The ratio of displacements, used in the order of magnitude analysis in Section 2.1.4, is then given by:

$$\Delta X_{Br}/\Delta X_{DEP} = \sqrt{(2k_BT)/(u^2\gamma t)} = \sqrt{(2k_BT\gamma)/(F^2t)} \tag{D.3}$$

Appendix E

Chaining NWs

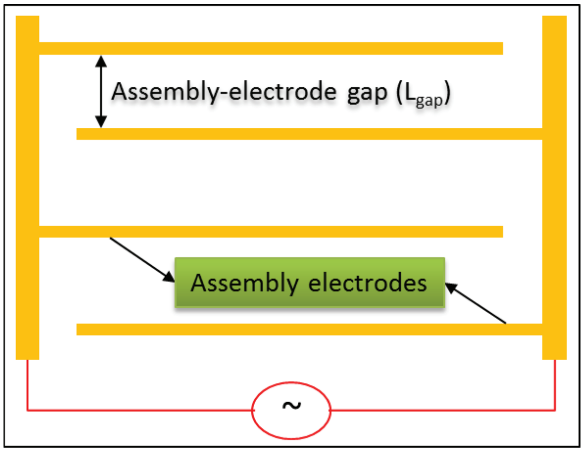

Figure E.1: Schematic of interdigitated electrodes.

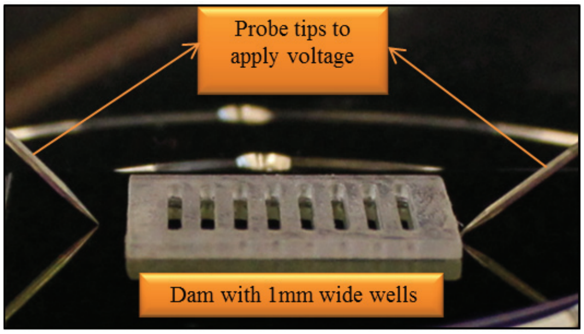

Figure E.2: Using a dam to increase available time (before alcohol evaporates), for creating multiple chains bridging the electrodes.

Appendix F

Effect of Capillary on NW-Chains Configuration

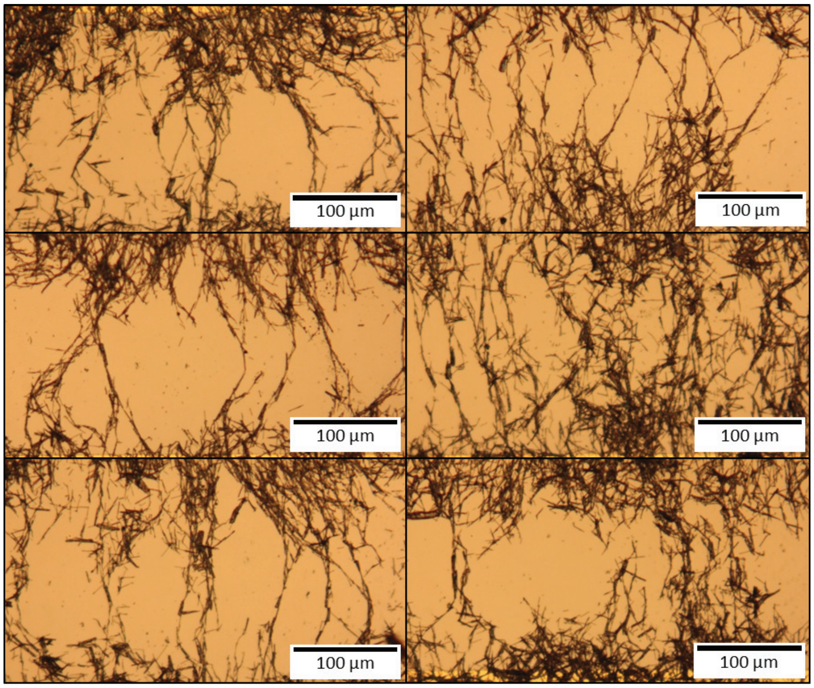

Figure F.1: Effect of capillary force at the NW suspension drying front on configuration of NW chains. Assembly-electrode gap size is 240μm. Capillary force can break the bridged chains. Small chain segments agglomerate on the substrate.

Appendix G

Grid-Shaped Assembly Electrode

This Appendix provides information on fabrication steps for grid-shaped assembly electrodes. Three different masks were used. A sketch of each mask is in the last page of this Appendix:

1- Pick 4” Si wafer with with 300 nm SiO_2

2- Clean sample with acetone and IPA

3-Dehydrate sample 1 min at 110°C followed by 2 min cool down in atmosphere temperature

4-Spin LOR A at 4000 RPM for 40 sec

5-Prebake wafer with LOR A for 2 min at 180°C

6-Spin coat 1 μm AZ703 photoresist at 4500 RPM for 40 s

7-Prebake sample for 1 min at 90°C followed by 1 min cool down in atmosphere temperature

8-Second stage of prebake 1 min at 110°C followed by 2 min cool down in atmosphere temperature

9-Expose AZ703 with mask1 for 4 sec

10-Develop AZ703 in developer MIF 300 for 55 sec

11-Oxygen descum

12-Load sample into evaporator

13-Evaporate desire metal (10 nm Ti/ 100 nm Au/ 10 nm Ti)

14-Soak sample in Microposit remover 1165 for 24 hours at room temperature

15-Sonicate Micro 1165 remover if necessary

16-Rinse in DI water and IPA
17-Load sample into PE-CVD to deposit 300 nm of SiO_2. Deposition rate and time was chosen 22 nm/min and 818 sec respectively
18-Repeat steps 2 to 8
19-Expose AZ703 with mask3-a for 4 sec
20-Develop AZ703 in developer MIF 300 for 55 sec
21-Oxygen descum
22-Load sample into RIE to etch SiO_2 with CHF_3. Rate and time for etching process was 26 nm/min and 12 min respectively.
23-Check the conductivity of the exposed electrode to make sure that SiO_2 layer is entirely etched.
24-Soak sample in acetone for 2 min to remove remaining AZ703
25-Repeat steps 2 to 8
26-Expose AZ703 with mask2 for 4 sec
27-Repeat steps 10 to 18
28-Expose AZ703 with mask3b for 4 sec
29-Repeat steps 20 to 23

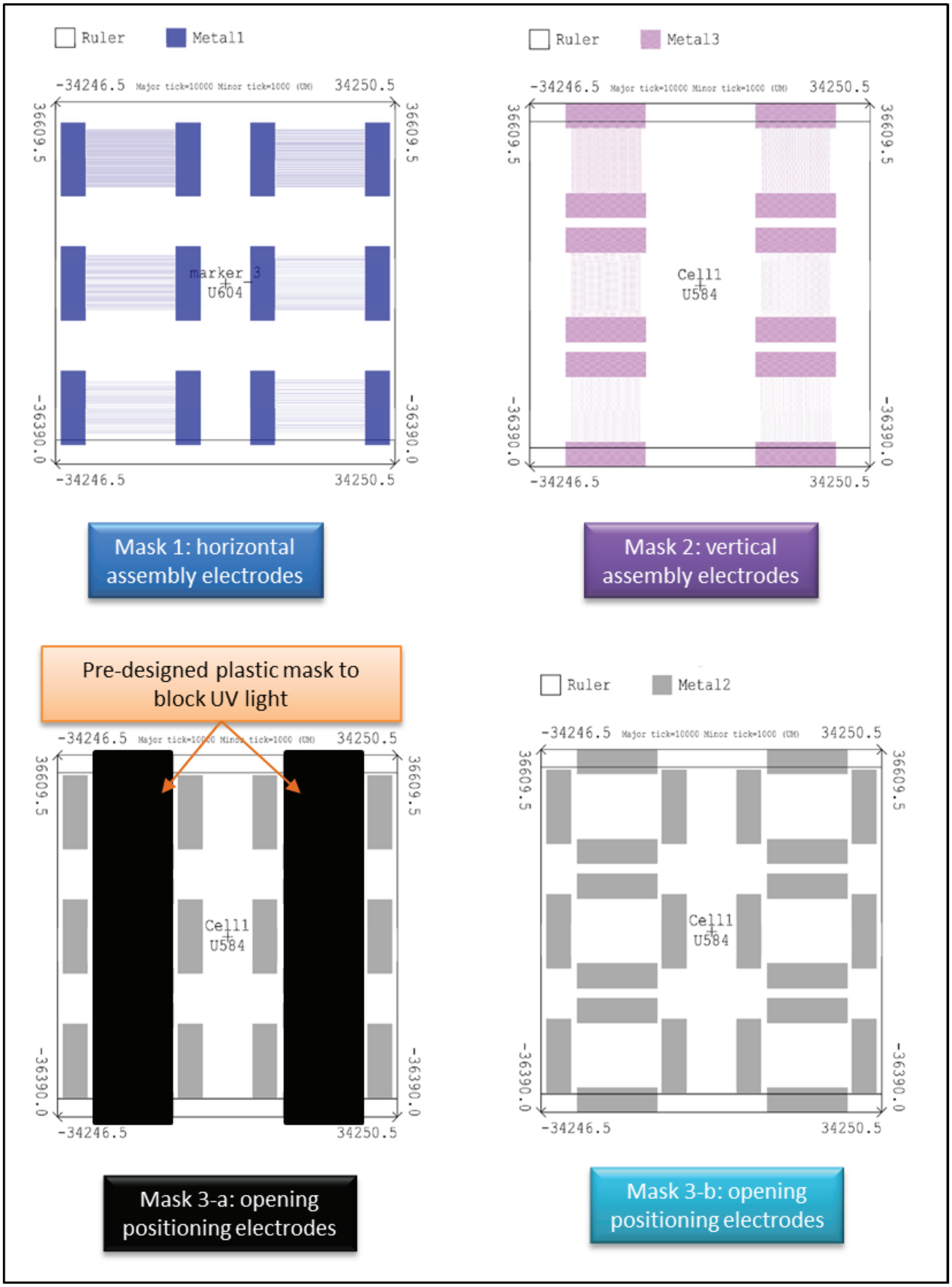

Figure G.1: Three different photolithography masks designed by using L-Edit software.

Bibliography

[1] H. Kawaguchi, T. Someya, T. Sekitani, and T. Sakurai, "Cut-and-paste customization of organic FET integrated circuit and its application to electronic artificial skin," *IEEE Journal of Solid-State Circuits*, vol. 40, no. 1, pp. 177–185, 2005.

[2] J. Viventi, D.-H. Kim, L. Vigeland, E. S. Frechette, J. A. Blanco, Y.-S. Kim, A. E. Avrin, V. R. Tiruvadi, S.-W. Hwang, A. C. Vanleer *et al.*, "Flexible, foldable, actively multiplexed, high-density electrode array for mapping brain activity in vivo," *Nature Neuroscience*, vol. 14, no. 12, pp. 1599–1605, 2011.

[3] J. A. Sioss, R. B. Bhiladvala, W. Pan, M. Li, S. Patrick, P. Xin, S. L. Dean, C. D. Keating, T. S. Mayer, and G. A. Clawson, "Nanoresonator chip-based RNA sensor strategy for detection of circulating tumor cells: response using PCA3 as a prostate cancer marker," *Nanomedicine: Nanotechnology, Biology and Medicine*, vol. 8, no. 6, pp. 1017–1025, 2012.

[4] Z. Fan, J. C. Ho, Z. A. Jacobson, R. Yerushalmi, R. L. Alley, H. Razavi, and A. Javey, "Wafer-scale assembly of highly ordered semiconductor nanowire arrays by contact printing," *Nano Letters*, vol. 8, no. 1, pp. 20–25, 2008.

[5] J. Goldberger, A. I. Hochbaum, R. Fan, and P. Yang, "Silicon vertically integrated nanowire field effect transistors," *Nano Letters*, vol. 6, no. 5, pp. 973–977, 2006.

[6] S. Nam, M. Song, D.-H. Kim, B. Cho, H. M. Lee, J.-D. Kwon, S.-G. Park, K.-S. Nam, Y. Jeong, S.-H. Kwon, J.-W. Kang, S. Jo, and C. Su Kim, "Ultrasmooth, extremely deformable and shape recoverable Ag nanowire embedded transparent electrode," *Scientific Reports*, vol. 4, 2014.

[7] S. Bae, H. Kim, Y. Lee, X. Xu, J.-S. Park, Y. Zheng, J. Balakrishnan, T. Lei, H. R. Kim, Y. I. Song *et al.*, "Roll-to-roll production of 30-inch graphene films for transparent electrodes," *Nature nanotechnology*, vol. 5, no. 8, pp. 574–578, 2010.

[8] E. C. Garnett, M. L. Brongersma, Y. Cui, and M. D. McGehee, "Nanowire solar cells," *Annual Review of Materials Research*, vol. 41, pp. 269–295, 2011.

[9] M. Yu, Y.-Z. Long, B. Sun, and Z. Fan, "Recent advances in solar cells based on one-dimensional nanostructure arrays," *Nanoscale*, vol. 4, no. 9, pp. 2783–2796, 2012.

[10] M.-W. Ahn, K.-S. Park, J.-H. Heo, D.-W. Kim, K. J. Choi, and J.-G. Park, "On-chip fabrication of ZnO-nanowire gas sensor with high gas sensitivity," *Sensors and Actuators B: Chemical*, vol. 138, no. 1, pp. 168–173, 2009.

[11] S. Ghashghaie, E. Marzbanrad, B. Raissi, C. Zamani, and R. Riahifar, "Effect of low frequency electric field parameters on chain formation of ZnO nanoparticles for gas sensing applications," *Journal of the American Ceramic Society*, vol. 95, no. 6, pp. 1843–1850, 2012.

[12] J. Lee, S. Mubeen, C. M. Hangarter, A. Mulchandani, W. Chen, and N. V. Myung, "Selective and rapid room temperature detection of H2S using gold nanoparticle chain arrays," *Electroanalysis*, vol. 23, no. 11, pp. 2623–2628, 2011.

[13] J. Suehiro, "Fabrication and characterization of nanomaterial-based sensors using dielectrophoresis," *Biomicrofluidics*, vol. 4, no. 2, pp. 022 804–022 814, 2010.

[14] M. Li, R. B. Bhiladvala, T. J. Morrow, J. A. Sioss, K.-K. Lew, J. M. Redwing, C. D. Keating, and T. S. Mayer, "Bottom-up assembly of large-area nanowire resonator arrays," *Nature Nanotechnology*, vol. 3, no. 2, pp. 88–92, 2008.

[15] W. Kang, C. Yan, C. Y. Foo, and P. S. Lee, "Foldable electronics: Foldable electrochromics enabled by nanopaper transfer method," *Advanced Functional Materials*, vol. 25, no. 27, pp. 4202–4202, 2015.

[16] J.-Y. Lee, S. T. Connor, Y. Cui, and P. Peumans, "Solution-processed metal nanowire mesh transparent electrodes," *Nano Letters*, vol. 8, no. 2, pp. 689–692, 2008.

[17] J. Suehiro, G. Zhou, and M. Hara, "Fabrication of a carbon nanotube-based gas sensor using dielectrophoresis and its application for ammonia detection by impedance spectroscopy," *Journal of Physics D: Applied Physics*, vol. 36, no. 21, pp. L109–L114, 2003.

[18] R. B. Bhiladvala, "Nanomechanical resonant sensors and fluid interactions," in *Encyclopedia of Nanotechnology.* Springer, 2012, pp. 1630–1643.

[19] J. Chaste, A. Eichler, J. Moser, G. Ceballos, R. Rurali, and A. Bachtold, "A nanomechanical mass sensor with yoctogram resolution," *Nature Nanotechnology*, vol. 7, no. 5, pp. 301–304, 2012.

[20] A. Heidelberg, L. T. Ngo, B. Wu, M. A. Phillips, S. Sharma, T. I. Kamins, J. E. Sader, and J. J. Boland, "A generalized description of the elastic properties of nanowires," *Nano Letters*, vol. 6, no. 6, pp. 1101–1106, 2006.

[21] M. Li, T. S. Mayer, J. A. Sioss, C. D. Keating, and R. B. Bhiladvala, "Template-grown metal nanowires as resonators: performance and characterization of dissipative and elastic properties," *Nano Letters*, vol. 7, no. 11, pp. 3281–3284, 2007.

[22] X. Wu, J. S. Kulkarni, G. Collins, N. Petkov, D. Almécija, J. J. Boland, D. Erts, and J. D. Holmes, "Synthesis and electrical and mechanical properties of silicon and germanium nanowires," *Chemistry of Materials*, vol. 20, no. 19, pp. 5954–5967, 2008.

[23] R. B. Bhiladvala and Z. J. Wang, "Effect of fluids on the Q factor and resonance frequency of oscillating micrometer and nanometer scale beams," *Physical Review E*, vol. 69, no. 3, pp. 036 307–5, 2004.

[24] W. Lu and C. M. Lieber, "Semiconductor nanowires," *Journal of Physics D: Applied Physics*, vol. 39, no. 21, pp. R387–R406, 2006.

[25] J. Boote and S. Evans, "Dielectrophoretic manipulation and electrical characterization of gold nanowires," *Nanotechnology*, vol. 16, no. 9, pp. 1500–1505, 2005.

[26] T. Sahai, R. B. Bhiladvala, and A. T. Zehnder, "Thermomechanical transitions in doubly-clamped micro-oscillators," *International Journal of Non-Linear Mechanics*, vol. 42, no. 4, pp. 596–607, 2007.

[27] D. Mijatovic, J. Eijkel, and A. Van Den Berg, "Technologies for nanofluidic systems: top-down vs. bottom-up a review," *Lab on a Chip*, vol. 5, no. 5, pp. 492–500, 2005.

[28] M. J. Madou, *Fundamentals of microfabrication: the science of miniaturization.* CRC press, 2002.

[29] M. Kwiat, S. Cohen, A. Pevzner, and F. Patolsky, "Large-scale ordered 1d-nanomaterials arrays: Assembly or not?" *Nano Today*, vol. 8, no. 6, pp. 677–694, 2013.

[30] R. G. Hobbs, N. Petkov, and J. D. Holmes, "Semiconductor nanowire fabrication by bottom-up and top-down paradigms," *Chemistry of Materials*, vol. 24, no. 11, pp. 1975–1991, 2012.

[31] J. C. Love, K. E. Paul, and G. M. Whitesides, "Fabrication of nanometer-scale features by controlled isotropic wet chemical etching," *Advanced Materials*, vol. 13, no. 8, pp. 604–607, 2001.

[32] M. Kumar and Y. Ando, "Chemical vapor deposition of carbon nanotubes: a review on growth mechanism and mass production," *Journal of Nanoscience and Nanotechnology*, vol. 10, no. 6, pp. 3739–3758, 2010.

[33] Y. Huang, X. Duan, and C. M. Lieber, "Nanowires for integrated multicolor nanophotonics," *Small*, vol. 1, no. 1, pp. 142–147, 2005.

[34] Y. Huang, X. Duan, Q. Wei, and C. M. Lieber, "Directed assembly of one-dimensional nanostructures into functional networks," *Science*, vol. 291, no. 5504, pp. 630–633, 2001.

[35] M. Li, "Hybrid integration of nanowire resonator arrays," *PhD thesis*, 2008.

[36] T. B. Jones, *Electromechanics of particles.* Cambridge University Press, New York, 1995.

[37] T. B. Jones, "Basic theory of dielectrophoresis and electrorotation," *Engineering in Medicine and Biology Magazine, IEEE*, vol. 22, no. 6, pp. 33–42, 2003.

[38] R. Pethig, "Review articledielectrophoresis: status of the theory, technology, and applications," *Biomicrofluidics*, vol. 4, no. 2, pp. 022811-022835, 2010.

[39] E. M. Freer, O. Grachev, X. Duan, S. Martin, and D. P. Stumbo, “High-yield self-limiting single-nanowire assembly with dielectrophoresis,” *Nature Nanotechnology*, vol. 5, no. 7, pp. 525–530, 2010.

[40] M. Collet, S. Salomon, N. Y. Klein, F. Seichepine, C. Vieu, L. Nicu, and G. Larrieu, “Large-scale assembly of single nanowires through capillary-assisted dielectrophoresis,” *Advanced Materials*, vol. 27, pp. 1268–1273, 2014.

[41] S. Raychaudhuri, S. A. Dayeh, D. Wang, and E. T. Yu, “Precise semiconductor nanowire placement through dielectrophoresis,” *Nano Letters*, vol. 9, no. 6, pp. 2260–2266, 2009.

[42] B. R. Burg, V. Bianco, J. Schneider, and D. Poulikakos, “Electrokinetic framework of dielectrophoretic deposition devices,” *Journal of Applied Physics*, vol. 107, no. 12, pp. 124 308–11, 2010.

[43] H.-S. Kim, E. Brueckner, J. Song, Y. Li, S. Kim, C. Lu, J. Sulkin, K. Choquette, Y. Huang, R. G. Nuzzo *et al.*, “Unusual strategies for using indium gallium nitride grown on silicon (111) for solid-state lighting,” *Proceedings of the National Academy of Sciences*, vol. 108, no. 25, pp. 10 072–10 077, 2011.

[44] D.-H. Kim, N. Lu, R. Ghaffari, and J. A. Rogers, “Inorganic semiconductor nanomaterials for flexible and stretchable bio-integrated electronics,” *NPG Asia Materials*, vol. 4, no. 4, pp. 1–9, 2012.

[45] A. Carlson, A. M. Bowen, Y. Huang, R. G. Nuzzo, and J. A. Rogers, “Transfer printing techniques for materials assembly and micro/nanodevice fabrication,” *Advanced Materials*, vol. 24, no. 39, pp. 5284–5318, 2012.

[46] Z. Liu, J. Xu, D. Chen, and G. Shen, “Flexible electronics based on inorganic nanowires,” *Chemical Society Reviews*, vol. 44, no. 1, pp. 161–192, 2015.

[47] L. Hu, H. Wu, and Y. Cui, “Metal nanogrids, nanowires, and nanofibers for transparent electrodes,” *MRS Bulletin*, vol. 36, no. 10, pp. 760–765, 2011.

[48] K. Ellmer, “Past achievements and future challenges in the development of optically transparent electrodes,” *Nature Photonics*, vol. 6, no. 12, pp. 809–817, 2012.

[49] A. R. Madaria, A. Kumar, F. N. Ishikawa, and C. Zhou, “Uniform, highly conductive, and patterned transparent films of a percolating silver nanowire network on rigid and flexible substrates using a dry transfer technique,” *Nano Research*, vol. 3, no. 8, pp. 564–573, 2010.

[50] A. R. Madaria, A. Kumar, and C. Zhou, “Large scale, highly conductive and patterned transparent films of silver nanowires on arbitrary substrates and their application in touch screens,” *Nanotechnology*, vol. 22, no. 24, pp. 245201–8, 2011.

[51] J.-Y. Lee, S. T. Connor, Y. Cui, and P. Peumans, “Semitransparent organic photovoltaic cells with laminated top electrode,” *Nano Letters*, vol. 10, no. 4, pp. 1276–1279, 2010.

[52] C.-H. Chung, T.-B. Song, B. Bob, R. Zhu, and Y. Yang, “Solution-processed flexible transparent conductors composed of silver nanowire networks embedded in indium tin oxide nanoparticle matrices,” *Nano Research*, vol. 5, no. 11, pp. 805–814, 2012.

[53] D.-S. Leem, A. Edwards, M. Faist, J. Nelson, D. D. Bradley, and J. C. de Mello, “Efficient organic solar cells with solution-processed silver nanowire electrodes,” *Advanced Materials*, vol. 23, no. 38, pp. 4371–4375, 2011.

[54] R. C. Tenent, T. M. Barnes, J. D. Bergeson, A. J. Ferguson, B. To, L. M. Gedvilas, M. J. Heben, and J. L. Blackburn, “Ultrasmooth, large-area, high-uniformity, conductive transparent single-walled-carbon-nanotube films for photovoltaics produced by ultrasonic spraying,” *Advanced Materials*, vol. 21, no. 31, pp. 3210–3216, 2009.

[55] V. Scardaci, R. Coull, P. E. Lyons, D. Rickard, and J. N. Coleman, “Spray deposition of highly transparent, low-resistance networks of silver nanowires over large areas,” *Small*, vol. 7, no. 18, pp. 2621–2628, 2011.

[56] M.-G. Kang, M.-S. Kim, J. Kim, and L. J. Guo, “Organic solar cells using nanoimprinted transparent metal electrodes,” *Advanced Materials*, vol. 20, no. 23, pp. 4408–4413, 2008.

[57] H. Wu, D. Kong, Z. Ruan, P.-C. Hsu, S. Wang, Z. Yu, T. J. Carney, L. Hu, S. Fan, and Y. Cui, “A transparent electrode based on a metal nanotrough network,” *Nature Nanotechnology*, vol. 8, no. 6, pp. 421–425, 2013.

[58] H. Wu, L. Hu, M. W. Rowell, D. Kong, J. J. Cha, J. R. McDonough, J. Zhu, Y. Yang, M. D. McGehee, and Y. Cui, “Electrospun metal nanofiber webs as high-performance transparent electrode,” *Nano Letters*, vol. 10, no. 10, pp. 4242–4248, 2010.

[59] J. van de Groep, P. Spinelli, and A. Polman, “Transparent conducting silver nanowire networks,” *Nano Letters*, vol. 12, no. 6, pp. 3138–3144, 2012.

[60] M. Sam, N. Moghimian, and R. B. Bhiladvala, “Field-directed chaining of nanowires: Towards transparent electrodes,” *Materials Letters*, vol. 163, pp. 205–208, 2016.

[61] W. Fang and J. Wickert, “Determining mean and gradient residual stresses in thin films using micromachined cantilevers,” *Journal of Micromechanics and Microengineering*, vol. 6, no. 3, pp. 301–309, 1996.

[62] Y. Zhang, “Deflections and curvatures of a film–substrate structure with the presence of gradient stress in mems applications,” *Journal of Micromechanics and Microengineering*, vol. 17, no. 4, pp. 753–762, 2007.

[63] N. Moghimian, “Electrochemical control for nanoelectromechanical device production,” *PhD thesis*, 2015.

[64] Y. Calahorra, O. Shtempluck, V. Kotchetkov, and Y. E. Yaish, “Youngs modulus, residual stress, and crystal orientation of doubly clamped silicon nanowire beams,” *Nano Letters*, vol. 15, no. 5, pp. 2945–2950, 2015.

[65] Y. Yang, C. Callegari, X. Feng, K. Ekinci, and M. Roukes, “Zeptogram-scale nanomechanical mass sensing,” *Nano Letters*, vol. 6, no. 4, pp. 583–586, 2006.

[66] Y. Dan, Y. Cao, T. E. Mallouk, A. T. Johnson, and S. Evoy, “Dielectrophoretically assembled polymer nanowires for gas sensing,” *Sensors and Actuators B: Chemical*, vol. 125, no. 1, pp. 55–59, 2007.

[67] J. Suehiro, N. Nakagawa, S.-i. Hidaka, M. Ueda, K. Imasaka, M. Higashihata, T. Okada, and M. Hara, “Dielectrophoretic fabrication and characterization of

a ZnO nanowire-based UV photosensor," *Nanotechnology*, vol. 17, no. 10, pp. 2567–2573, 2006.

[68] Y. Liu, J.-H. Chung, W. K. Liu, and R. S. Ruoff, "Dielectrophoretic assembly of nanowires," *The Journal of Physical Chemistry B*, vol. 110, no. 29, pp. 14 098–14 106, 2006.

[69] A. San Paulo, J. Bokor, R. Howe, R. He, P. Yang, D. Gao, C. Carraro, and R. Maboudian, "Mechanical elasticity of single and double clamped silicon nanobeams fabricated by the vapor-liquid-solid method," *Applied Physics Letters*, vol. 87, no. 5, pp. 053111–13, 2005.

[70] S. Lee and R. Bashir, "Dielectrophoresis and electrohydrodynamics-mediated fluidic assembly of silicon resistors," *Applied Physics Letters*, vol. 83, no. 18, pp. 3833–3835, 2003.

[71] M. Sam, N. Moghimian, and R. B. Bhiladvala, "Field-directed assembly of nanowires: identifying directors, disruptors and indices to maximize device yield," *Nanoscale*, vol. 8, no. 2, pp. 889–900, 2016.

[72] E. Sage, A. Brenac, T. Alava, R. Morel, C. Dupré, M. S. Hanay, M. L. Roukes, L. Duraffourg, C. Masselon, and S. Hentz, "Neutral particle mass spectrometry with nanomechanical systems," *Nature Communications*, vol. 6, pp. 6482–6487, 2015.

[73] B. Ilic, Y. Yang, K. Aubin, R. Reichenbach, S. Krylov, and H. Craighead, "Enumeration of DNA molecules bound to a nanomechanical oscillator," *Nano Letters*, vol. 5, no. 5, pp. 925–929, 2005.

[74] N. P. Dasgupta, J. Sun, C. Liu, S. Brittman, S. C. Andrews, J. Lim, H. Gao, R. Yan, and P. Yang, "25th anniversary article: semiconductor nanowires–synthesis, characterization, and applications," *Advanced Materials*, vol. 26, no. 14, pp. 2137–2184, 2014.

[75] B. D. Smith, T. S. Mayer, and C. D. Keating, "Deterministic assembly of functional nanostructures using nonuniform electric fields," *Annual Review of Physical Chemistry*, vol. 63, pp. 241–263, 2012.

[76] M. C. Wang and B. D. Gates, "Directed assembly of nanowires," *Materials Today*, vol. 12, no. 5, pp. 34–43, 2009.

[77] D. Whang, S. Jin, Y. Wu, and C. M. Lieber, "Large-scale hierarchical organization of nanowire arrays for integrated nanosystems," *Nano Letters*, vol. 3, no. 9, pp. 1255–1259, 2003.

[78] N. K. Palapati, E. Pomerantseva, and A. Subramanian, "Single nanowire manipulation within dielectrophoretic force fields in the sub-crossover frequency regime," *Nanoscale*, vol. 7, pp. 3109–3116, 2015.

[79] A. Maijenburg, M. Maas, E. Rodijk, W. Ahmed, E. Kooij, E. Carlen, D. Blank, and J. Ten Elshof, "Dielectrophoretic alignment of metal and metal oxide nanowires and nanotubes: A universal set of parameters for bridging prepatterned microelectrodes," *Journal of Colloid and Interface Science*, vol. 355, no. 2, pp. 486–493, 2011.

[80] A. Castellanos, A. Ramos, A. Gonzalez, N. G. Green, and H. Morgan, "Electrohydrodynamics and dielectrophoresis in microsystems: scaling laws," *Journal of Physics D: Applied Physics*, vol. 36, no. 20, pp. 2584–2597, 2003.

[81] J. Happel and H. Brenner, *Low Reynolds number hydrodynamics: with special applications to particulate media.* Noordhoff International, 1973, vol. 1.

[82] J. Luecke and R. L. McCormick, "Electrical conductivity and phe response of fuel ethanol contaminants," *Energy & Fuels*, vol. 28, no. 8, pp. 5222–5228, 2014.

[83] N. G. Green, A. Ramos, A. Gonzalez, H. Morgan, and A. Castellanos, "Fluid flow induced by nonuniform ac electric fields in electrolytes on microelectrodes. i. experimental measurements," *Physical Review E*, vol. 61, no. 4, pp. 4011–4018, 2000.

[84] M. Z. Bazant, *Electrokinetics and electrohydrodynamics in microsystems.* Springer Science, 2011, vol. 530.

[85] B. C. Gierhart, D. G. Howitt, S. J. Chen, R. L. Smith, and S. D. Collins, "Frequency dependence of gold nanoparticle superassembly by dielectrophoresis," *Langmuir*, vol. 23, no. 24, pp. 12 450–12 456, 2007.

[86] P. Mirtaheri, S. Grimnes, and O. G. Martinsen, "Electrode polarization impedance in weak NaCl aqueous solutions," *IEEE Transactions on Biomedical Engineering*, vol. 52, no. 12, pp. 2093–2099, 2005.

[87] M. Z. Bazant, K. Thornton, and A. Ajdari, “Diffuse-charge dynamics in electrochemical systems,” *Physical Review E*, vol. 70, no. 2, pp. 021 506–24, 2004.

[88] N. Moghimian, M. Sam, and R. B. Bhiladvala, “Rhodium nanowires: Synthesis and nanostructure tailoring by controlling hydrogen evolution,” *Materials Letters*, vol. 113, pp. 152–155, 2013.

[89] L. Hu, H. S. Kim, J.-Y. Lee, P. Peumans, and Y. Cui, “Scalable coating and properties of transparent, flexible, silver nanowire electrodes,” *ACS Nano*, vol. 4, no. 5, pp. 2955–2963, 2010.

[90] P. N. Nirmalraj, A. T. Bellew, A. P. Bell, J. A. Fairfield, E. K. McCarthy, C. OKelly, L. F. Pereira, S. Sorel, D. Morosan, and J. N. Coleman, “Manipulating connectivity and electrical conductivity in metallic nanowire networks,” *Nano Letters*, vol. 12, no. 11, pp. 5966–5971, 2012.

[91] K. H. Bhatt and O. D. Velev, “Control and modeling of the dielectrophoretic assembly of on-chip nanoparticle wires,” *Langmuir*, vol. 20, no. 2, pp. 467–476, 2004.

[92] R. Kretschmer and W. Fritzsche, “Pearl chain formation of nanoparticles in microelectrode gaps by dielectrophoresis,” *Langmuir*, vol. 20, no. 26, pp. 11 797–11 801, 2004.

[93] D. L. House, H. Luo, and S. Chang, “Numerical study on dielectrophoretic chaining of two ellipsoidal particles,” *Journal of Colloid and Interface Science*, vol. 374, no. 1, pp. 141–149, 2012.

[94] A. Oliva-Avilés, F. Avilés, V. Sosa, and G. Seidel, “Dielectrophoretic modeling of the dynamic carbon nanotube network formation in viscous media under alternating current electric fields,” *Carbon*, vol. 69, pp. 342–354, 2014.

[95] W. Ahmed, E. S. Kooij, A. Van Silfhout, and B. Poelsema, “Quantitative analysis of gold nanorod alignment after electric field-assisted deposition,” *Nano Letters*, vol. 9, no. 11, pp. 3786–3794, 2009.

[96] S. Cherukulappurath, S. H. Lee, A. Campos, C. L. Haynes, and S.-H. Oh, “Rapid and sensitive in situ sers detection using dielectrophoresis,” *Chemistry of Materials*, vol. 26, no. 7, pp. 2445–2452, 2014.

[97] S. J. Papadakis, J. A. Hoffmann, D. Deglau, A. Chen, P. Tyagi, and D. H. Gracias, "Quantitative analysis of parallel nanowire array assembly by dielectrophoresis," *Nanoscale*, vol. 3, no. 3, pp. 1059–1065, 2011.

[98] S. Boehm, L. Lin, K. Guzman Betancourt, R. Emery, J. Mayer, T. Mayer, and C. D. Keating, "Formation and frequency response of two-dimensional nanowire lattices in an applied electric field," *Langmuir*, vol. 31, pp. 5779–5786, 2015.

[99] E. C. Garnett, W. Cai, J. J. Cha, F. Mahmood, S. T. Connor, M. G. Christoforo, Y. Cui, M. D. McGehee, and M. L. Brongersma, "Self-limited plasmonic welding of silver nanowire junctions," *Nature Materials*, vol. 11, no. 3, pp. 241–249, 2012.

[100] J. A. Spechler, K. A. Nagamatsu, J. C. Sturm, and C. B. Arnold, "Improved efficiency of hybrid organic photovoltaics by pulsed laser sintering of silver nanowire network transparent electrode," *ACS Applied Materials and Interfaces*, vol. 7, pp. 10 556–10 562, 2015.

[101] S. O. Lumsdon and D. M. Scott, "Assembly of colloidal particles into microwires using an alternating electric field," *Langmuir*, vol. 21, no. 11, pp. 4874–4880, 2005.

[102] P. Blake, P. D. Brimicombe, R. R. Nair, T. J. Booth, D. Jiang, F. Schedin, L. A. Ponomarenko, S. V. Morozov, H. F. Gleeson, and E. W. Hill, "Graphene-based liquid crystal device," *Nano Letters*, vol. 8, no. 6, pp. 1704–1708, 2008.

[103] J. Zou, C.-Z. Li, C.-Y. Chang, H.-L. Yip, and A. K.-Y. Jen, "Interfacial engineering of ultrathin metal film transparent electrode for flexible organic photovoltaic cells," *Advanced Materials*, vol. 26, no. 22, pp. 3618–3623, 2014.

[104] M. Theuring, V. Steenhoff, S. Geißendörfer, M. Vehse, K. von Maydell, and C. Agert, "Laser perforated ultrathin metal films for transparent electrode applications," *Optics Express*, vol. 23, no. 7, pp. A254–A262, 2015.

[105] D. Ghosh, T. Chen, and V. Pruneri, "High figure-of-merit ultrathin metal transparent electrodes incorporating a conductive grid," *Applied Physics Letters*, vol. 96, no. 4, pp. 041109–3, 2010.

[106] H. Xu, H. Wang, C. Wu, N. Lin, A. M. Soomro, H. Guo, C. Liu, X. Yang, Y. Wu, D. Cai, and J. Kang, "Direct synthesis of graphene 3d-coated cu nanosilks

network for antioxidant transparent conducting electrode," *Nanoscale*, vol. 7, pp. 10 613–10 621, 2015.

[107] Y. Ai, Z. Zeng, and S. Qian, "Direct numerical simulation of ac dielectrophoretic particle–particle interactive motions," *Journal of Colloid and Interface Science*, vol. 417, pp. 72–79, 2014.

[108] J. P. Singh, P. P. Lele, F. Nettesheim, N. J. Wagner, and E. M. Furst, "One-and two-dimensional assembly of colloidal ellipsoids in ac electric fields," *Physical Review E*, vol. 79, no. 5, pp. 050401–4, 2009.

[109] P. B. Catrysse and S. Fan, "Nanopatterned metallic films for use as transparent conductive electrodes in optoelectronic devices," *Nano Letters*, vol. 10, no. 8, pp. 2944–2949, 2010.

[110] R. A. Serway and J. W. Jewett, *Principles of Physics*. Saunders College Pub. Fort Worth, TX, 1998, vol. 1.

[111] Y. Sun and J. A. Rogers, "Inorganic semiconductors for flexible electronics," *Advanced Materials*, vol. 19, no. 15, pp. 1897–1916, 2007.

[112] Z. Fan, J. C. Ho, T. Takahashi, R. Yerushalmi, K. Takei, A. C. Ford, Y.-L. Chueh, and A. Javey, "Toward the development of printable nanowire electronics and sensors," *Advanced Materials*, vol. 21, no. 37, pp. 3730–3743, 2009.

[113] X. Liu, Y.-Z. Long, L. Liao, X. Duan, and Z. Fan, "Large-scale integration of semiconductor nanowires for high-performance flexible electronics," *ACS Nano*, vol. 6, no. 3, pp. 1888–1900, 2012.

[114] S. R. Forrest, "The path to ubiquitous and low-cost organic electronic appliances on plastic," *Nature*, vol. 428, no. 6986, pp. 911–918, 2004.

[115] A. Chirilă, S. Buecheler, F. Pianezzi, P. Bloesch, C. Gretener, A. R. Uhl, C. Fella, L. Kranz, J. Perrenoud, S. Seyrling *et al.*, "Highly efficient Cu (In, Ga) Se2 solar cells grown on flexible polymer films," *Nature materials*, vol. 10, no. 11, pp. 857–861, 2011.

[116] U. Kang and K. D. Wise, "A high-speed capacitive humidity sensor with on-chip thermal reset," *IEEE Transactions on Electron Devices*, vol. 47, no. 4, pp. 702–710, 2000.

[117] R. Ramya, R. Sivasubramanian, and M. Sangaranarayanan, “Conducting polymers-based electrochemical supercapacitorsprogress and prospects,” *Electrochimica Acta*, vol. 101, pp. 109–129, 2013.